공학박사 학위논문

Study on Intrinsic Rotation in KSTAR Ohmic Plasmas

KSTAR 오믹 플라즈마의 고유 유동에 대한 연구

2017년 8월

서울대학교 대학원

에너지시스템공학부

나 동 현

Study on Intrinsic Rotation in KSTAR Ohmic Plasmas

지도 교수 나 용 수

이 논문을 공학박사 학위논문으로 제출함
2017년 7월

서울대학교 대학원
에너지시스템공학부
나 동 현

나동현의 공학박사 학위논문을 인준함
2017년 6월

위 원 장 함 택 수 (인)

부위원장 나 용 수 (인)

위 원 황 용 석 (인)

위 원 장 호 건 (인)

위 원 고 원 하 (인)

Abstract

Study on Intrinsic Rotation in KSTAR Ohmic Plasmas

Na, Donghyeon

Department of Energy System Engineering

(Fusion & Plasma Engineering)

The Graduate School

Seoul National University

Plasma rotation is known to affect tokamak plasma performance and stability. The intrinsic rotation study is one of the important issues of tokamak plasma because it is expected that the plasma rotation by external torque sources is small in large devices such as ITER unlike the present tokamaks. Ohmic plasma could be the most suitable plasma for studying the physical mechanism of the intrinsic rotation generation and the experiments for the intrinsic rotation in Ohmic plasma has been conducted in various tokamaks. KSTAR, a domestic tokamak, had also been conducting experimental studies on

the intrinsic rotation in Ohmic plasmas, but previous studies only focused on the core intrinsic rotation using XICS measurement ($V_\phi(0)$ based analysis on the intrinsic rotation).

In this research, the experiment was designed to measure the profiles of the intrinsic rotation, and the profile-based analysis was performed to investigate the experimental characteristics of the intrinsic rotation in KSTAR Ohmic plasmas. Based on this database and experimental characteristics, a comparative analysis with various theoretical models for the intrinsic rotation generation was carried out. Then, the integrated modelling was conducted to predict the intrinsic rotation profiles using the selected model in KSTAR Ohmic plasmas and compare the intrinsic rotation profiles in experiments.

In order to measure the intrinsic rotation profiles in KSTAR, neutral beam injection is inevitably required. At this time, neutral beam injection not only disturb the plasma properties but also cause deformation of the plasma rotation due to external torques, so it is of the highest priority to minimize the external perturbation and to measure the intrinsic rotation in pure Ohmic plasma as much as possible. For this purpose, the optimal operating conditions of the neutral beam injection for measuring the intrinsic rotation profiles in KSTAR Ohmic plasma were experimentally derived. The optimal operating conditions depend on the plasma condition and purpose; in

KSTAR Ohmic plasma with a plasma current of 400−600 kA, it is confirmed that 20 ms * 2 Hz or less of beam injection duration and frequency should be at least satisfied.

As a result of the investigation of the intrinsic rotation profiles measured under various operating and plasma conditions, it is confirmed that $V_\phi(0)$ based analysis could be limited to capture the intrinsic rotation characteristics. To sufficiently cover the intrinsic rotation characteristics using $V_\phi(0)$ based analysis, two conditions are required. One is that the intrinsic rotation near the plasma boundary must be negligible, and the other is that the intrinsic rotation profile must be a simple curve. It has been confirmed that the intrinsic rotation near the plasma boundary depends on various operating and plasma conditions in KSTAR Ohmic plasma, and that even under the same operating conditions, it depends on when the experiment is performed. This means that the intrinsic rotation near the plasma boundary is sensitive to not only the operating conditions but also wall conditions. Furthermore, the change of the intrinsic rotation near the plasma boundary in KSTAR Ohmic plasma is up to 20 km/s. This is a level that cannot be ignored when compared with the typical variation of $V_\phi(0)$ in KSTAR Ohmic plasma. The other thing is that the intrinsic rotation profile does not have a simple curved shape and the toroidal rotation gradient could be varied

significantly depending on the radial location. It means that the intrinsic rotation profile must be considered in order to understand the actual intrinsic rotation characteristics. In consideration of these characteristics, we adopted the profile-based analysis and investigated the intrinsic rotation characteristics in KSTAR Ohmic plasma based on about 300 databases accumulated until 2016 KSTAR campaign.

First, we have examined the typical feature of the intrinsic rotation profiles. It is observed that the intrinsic rotation profiles in KSTAR Ohmic plasma could have a feature divided into four regions. The innermost region near the center of the plasma has a somewhat flat or slightly bulging shape, which is consistent with the inversion radius of sawtooth activity. Next, the region with a steep slope, called gradient region, is observed, and it usually has a positive gradient in KSTAR Ohmic plasmas. This region is strongly associated with the change in $V_{\phi}(0)$ as a result of the large change in slope with the increase of plasma density. The next is the anchor point region. Here, the profile seems again flattened and appears to act as the boundary region of the gradient region. This region is far from the actual plasma boundary, and is distinct from the actual plasma boundary region. The last part is the area between the anchor point region and the actual plasma boundary, and there are various shapes and values

of the intrinsic rotation according to the plasma operating conditions.

By analyzing the intrinsic rotation profiles for various operating conditions, it can be confirmed that the intrinsic rotation evolves from nearly flat to hollow shapes with the increase of the plasma density in KSTAR Ohmic plasmas and the feature of the intrinsic rotation is closely related to q_{95}. Here, the evolution of the intrinsic rotation mainly results from the change of the normalized rotation gradient (u') and its variation is only observed in the gradient region with the increase of plasma density while no significant change is observed in the anchor point region. Note that, the gradient region corresponds to the region with a low q value and a weak magnetic shear, and an anchor point region with a high q value and a strong magnetic shear.

The change of u' in the gradient region could be approximated by the ratio of the residual stress (the intrinsic rotation generation mechanism) and the momentum diffusivity. Here, it is expected that both are related to the turbulence characteristics such as ITG / TEM, so that the correlation of u' with the plasma properties such as $R/L_{T_i}, R/L_{T_e}, T_e/T_i, \nu_{eff}$ which effect on the turbulence characteristics was investigated. The analysis represents that the most important correlative properties are ν_{eff} and T_e/T_i. Interestingly, it was derived from the time-varying transport simulation that the change of u' in the gradient region would be closely related to the significant

change of the momentum diffusivity rather than the change of the residual stress. This is in agreement with experimental observations that u' always have a negative value even with a much lower collisionality with the ECH injection and the linear/nonlinear gyrokinetic simulations.

Using the KSTAR Ohmic plasma database, we have evaluated which theoretical model can well predict the intrinsic rotation characteristics. As a result of comparing and analyzing the neoclassical transport model and various turbulent transport models, it was found that the "finite ballooning tilting" model could well capture the intrinsic rotation characteristics observed in experiments. Although an arbitrary (but within a range of possible levels) tilting angle was used, the similar magnitude of u' in experiments could be represented, and even under fixed tilting angles, the model seems to predict similar ν_{eff} dependence in both gradient region and anchor point region. The difference between the gradient region and the anchor point region was found to be related to the magnetic shear and the q value. The predicted u' represents the similar ν_{eff} dependence of u' observed in the gradient region for the weak magnetic shear and the low q value case while it becomes smaller and the tendency is changed for the strong magnetic shear and the high q value case. This is consistent with experimental observations

where the gradient region and the anchor point region are related to the q value and the magnetic shear value.

Finally, in order to calculate the intrinsic rotation profiles in KSTAR Ohmic plasma by applying the "finite ballooning tilting" model, an integrated modelling was performed by combining the GKW code and the transport code ASTRA. Although the level of the intrinsic rotation from the modelling was predicted to be smaller than the intrinsic rotation in experiments, the change of u' with the increase of the collisionality and the profile feature which consists of the gradient region and the anchor point region seem to be well predicted.

This shows that the "finite ballooning tilting" model has a high potential as the intrinsic rotation generation mechanism in KSTAR Ohmic plasmas and the integrated modelling for the intrinsic rotation prediction would be utilized for various applications.

Keyword: Intrinsic Rotation, Profile-based analysis, KSTAR, Ohmic plasma, Gradient region, Anchor point region, Finite ballooning tilting

Student Number: 2011-21093

Table of Contents

List of Figures

Chapter 1. Introduction

1.1. Nuclear fusion and tokamak

1.1.1. Fusion reaction

Nuclear fusion is the process that more than one nuclei combines to form a single nucleus. In this process, the energy may release when the mass outcome is smaller than the income, following the mass – energy conservation law. The goal of present studies on the controlled nuclear fusion is to produce energy from the fusion reaction between two hydrogen isotopes; Deuterium (D) and Tritium (T). This reaction can be expressed as

$$ {}_1^2D + {}_1^3T = {}_1^4D(3.5\text{MeV}) + {}_0^1n(14.1\text{MeV}) \qquad (1.1) $$

D−T reaction is one of fusion process which requires smallest income energy. Therefore, it is most easily accessible and this is why present research is focused on this. Since kinetic energy outcome of this reaction (17.6 MeV) is much higher than income energy to overcome the coulomb barrier (~0.01 MeV), D−T reaction may be used to generate energy and electricity in future fusion power plant. To initiate the fusion reaction without heavy gravitation like sun,

temperature over 100 million kelvin is needed. At such temperature, most of matter is fully ionized and becomes plasma; the fourth state of matter. However, it is not a trivial to sustain a high energy particle and confinement of hot plasma for nuclear fusion is very challenging issues.

1.1.2. Plasma confinement

To initiate the fusion reaction, it is essential to sustain the hot and dense plasma in the limited space. Furthermore, high energy confinement is required to increase the plasma temperature with limited heating source and maintain the long time operation. Specifically, we can define the confinement time, τ_{E}, in stationary conditions as

$$\tau_E = \frac{W}{P_{inj}} \qquad (1.2)$$

where P_{inj} is injected power into plasma and W is total stored energy of plasma. τ_{E} presents the performance of energy confinement and it has to be big enough to make high energy plasma. In Lawson Criterion [1], it is found that the product of the plasma density n and τ_{E} requires $n\tau_{\mathrm{E}} > 1.5 \times 10^{20}\mathrm{m}^{-3}\mathrm{s}$ to ignite the fusion reactions to provide enough energy to maintain the plasma against

energy loss. Also, this condition has to be closely achieved to generate power from nuclear fusion under economic feasibility.

1.1.3. Tokamak

Tokamak is one of promising thermonuclear fusion device in present days. Its structure is shown in Figure 1.1. Toroidal field is generated by the currents in the toroidal field coil and poloidal field is formed by the toroidal currents inside the plasma current. There is also central solenoid coils to inductively drive the plasma current and several poloidal field coils to adjust the plasma position and shape. As a result, tokamak has a helical magnetic field configuration. It was firstly invented by Andrei Sakharov in 1950s. Through decades, concept of tokamak was significantly developed and physics of tokamak plasma were discovered within multiple devices, such as TFTR (USA), DIII-D (USA), JET (Europe), JT-60U (Japan) and KSTAR (Korea). With these development, the plasma performance has been greatly improved.

However, despite being the most effective device, the tokamak still faces some problems such as MHD instabilities and micro instabilities. These instabilities induce the energy flux to the outside of plasma and degrade the performance. Therefore, they have to be

controlled and suppressed to achieve the high plasma performance.

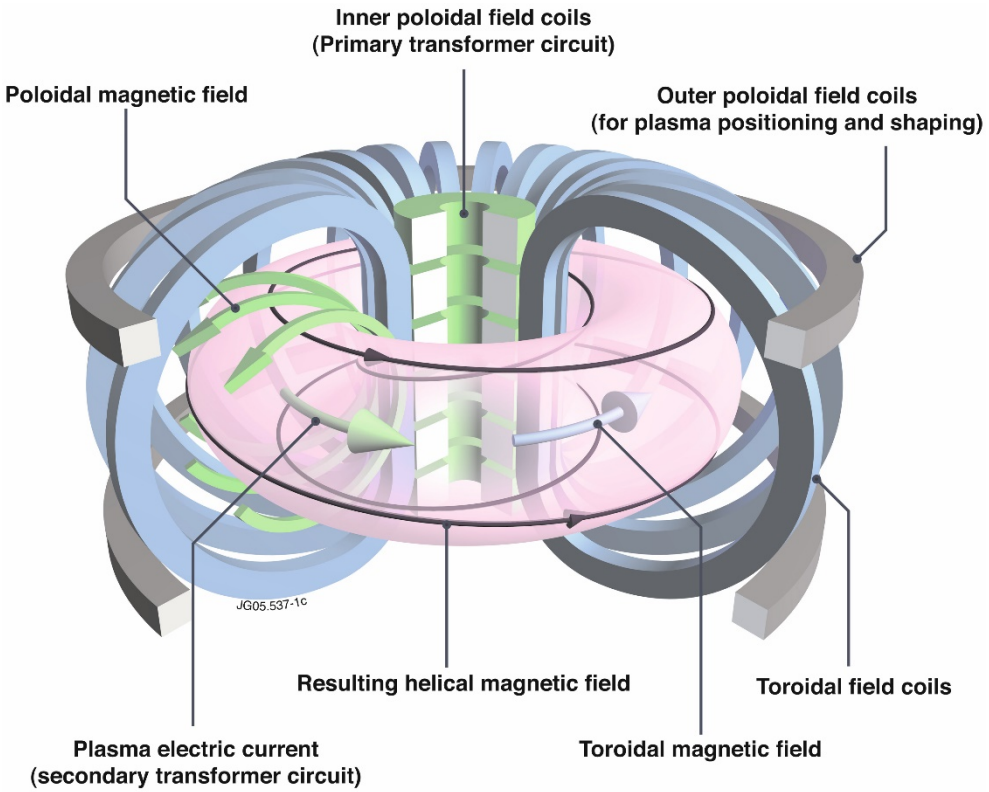

Figure 1.1 Schematic view of tokamak with plasma current and magnetic field [2].

In tokamak, $n\tau_E$ tends to increase with size of machine due to stiffness in plasma profile. As confinement improves in big device, large-scale tokamak device is preferred for plasma fusion, and it resulted in the construction of large devices such as JET and JT-60U. Furthermore, ITER (International Thermonuclear Experimental Reactor), the next large-scale tokamak, is under construction with

the international agreement. This future machine is expected to significantly improve the fusion research. In particular, it aims to solve the remaining obstacles in nuclear fusion and to prove the fusion energy as a resource of electrical power. For this reason, the success of ITER will be a key for the commercialization of nuclear fusion power plant. To achieve this goal, there is a need to address the remaining questions in the tokamak plasma before the ITER operation.

1.2. Plasma rotation and intrinsic rotation in tokamaks

In previous research, it has been found that the plasma rotation plays crucial role in the plasma performance especially on the MHD instabilities and micro-instabilities in tokamak plasma. Rotation can stabilize the Resistive Wall Mode (RWM) [3-8], which enables plasma to exceed the no wall limit and proceed to the higher operation regime. For micro-instabilities, the toroidal rotation may induce the shear in radial electric field and suppress the turbulence through the increased E x B shearing rate [9-12]. As micro-instabilities are weakened, the amplitude of anomalous transport can be reduced and energy confinement could be increased. Rotation shear at the edge region also can enhance the stability of edge localized mode (ELM)

in H−mode plasma and improve the stored energy in the edge pedestal [13]. Its influence on the neoclassical tearing mode was also reported [14].

1.2.1. Plasma rotation

Plasma rotation or flow of plasma is generally observed in present tokamaks. During the operation, the momentum sources such as neutral beam injection transfer the momentum to the plasma and the momentum is distributed in plasma through the transport process. In usual, the plasma rotation refers to the toroidal rotation, and this study deals with the toroidal rotation only. Toroidal rotation, u_ϕ, can be expressed with the governing equation as follows.

$$mn\frac{\partial\langle u_\phi\rangle}{\partial t} + \langle\nabla\cdot\overrightarrow{\Gamma_\phi}\rangle = \langle\vec{S}\rangle \qquad (1.3)$$

$$\vec{\Gamma}_\phi = (mn\vec{u}\vec{u})_\phi + \vec{\Pi}_\phi \qquad (1.4)$$

Here, quantities $(\vec{u}, n, m)$ refer flow velocity, plasma density and mass of a single fluid plasma (usually main ion). $\langle..\rangle$ refers flux averaged quantities. For a tokamak topology and cylindrical coordinates, the equation (1.3) can be expressed as follows.

$$\frac{\partial L_\phi}{\partial t} + \frac{1}{r}\frac{\partial}{\partial r}\left(r\Pi_{\phi r}\right) = \sum \tau_\phi \qquad (1.5)$$

where L_ϕ is the angular momentum ($L_\phi \equiv nmRV_\phi$), $\Pi_{\phi r}$ is the Reynolds stress, and $\sum \tau_\phi$ is the sum of the external torque. Here, the Reynolds stress term can be decomposed as follows.

$$\Pi_{\phi r} = -\chi_\phi \frac{\partial L_\phi}{\partial r} + V_p L_\phi + \Pi_{res} \qquad (1.6)$$

The terms on the right hand side represent the diffusive momentum flux ($-\chi_\phi \frac{\partial L_\phi}{\partial r}$), the convective momentum flux ($V_p L_\phi$), and the residual stress (Π_{res}), respectively [15].

1.2.2. Intrinsic rotation

Unlike the conventional tokamaks, recent studies for the ITER prediction suggest that the plasma rotation driven by external source would be small in ITER plasmas [16, 17]. It is due to a small momentum source when it is compared to the size of ITER. As a result, the degradation in the plasma performance and no RWM suppression due to the small rotation may expected in ITER.

Interestingly, the plasma rotation without external momentum

source has been observed in multiple tokamaks such as JET [18], Alcator C-Mod [19], Tore Supra [20], DIII-D [21] etc. and this can be the partial solution to generate the plasma rotation in ITER. This is called as "Intrinsic rotation". Previous studies have revealed that the intrinsic rotation in the present tokamaks has magnitude of $0.01 - 0.1\,M_A$ where M_A is Alfven Mach number. In the beginning, empirical approach in H-mode plasmas was made to predict the magnitude of the intrinsic rotation in ITER. Rice scaling is one of well-known results for the core intrinsic rotation based on inter-machine database [22]. It showed a relatively good agreement with the present devices and predicted that the intrinsic rotation in ITER will be order of $0.01\,M_A$. However, the recent subsequent studies in JET [23] and DIII-D [24] have suggested that Rice scaling does not work at high β_N plasmas in JET and the ITER intrinsic rotation prediction would be much smaller than the previous prediction of 1000 km/s. It shows the limitation of the empirical scaling approach; implying that the empirical scaling based on the H-mode database has failed. It is suggested that physics based study for the intrinsic rotation generation mechanisms associated with Π_{res} in the equation (1.6) is required even for the ITER prediction.

1.3. Intrinsic rotation study in Ohmic plasmas

For the physics study of the intrinsic rotation and its generation mechanisms in tokamaks, Ohmic plasma could be a best choice since there is no interaction with auxiliary heating such as ECH and ICRH as well as no external torque source.

It is important to note the history of the intrinsic rotation studies in Ohmic plasmas. Most of the intrinsic rotation studies in Ohmic plasmas have been focused on the rotation reversal phenomenon which was firstly reported in TCV [25]. Above a specific density threshold, the core intrinsic rotation is reversed from the co−current to the counter−current direction for diverted plasmas (but for limited plasmas, it is from the counter− to the co−current direction). The rotation reversal has been observed in other tokamaks such as Alcator C−Mod [26], ASDEX Upgrade [27], MAST [28], and KSTAR [29]. With experimental progresses in various tokamaks [30−41], there have been a lot of theoretical advances for the intrinsic rotation generation mechanisms as well as the rotation reversal [42−50], which include a specific symmetry breaking term of the radially/poloidally inhomogeneous turbulence, profile shearing, and the deviation of an equilibrium distribution from the Maxwellian. Most of them are related to $\mathbf{k}_{\parallel}$ symmetry breaking where it could be

mainly categorized into two features of the spectral shift of the single ballooning structure and the mode coupling in the spectral dispersion. Figures 1.2 (a) and 1.2 (b) show simplified pictures of them. At a local radial location, $\langle k_{\parallel} \rangle \neq 0$ is satisfied then it could result in a finite radial momentum flux as fluid-like contributions.

Even with the experimental and theoretical progresses, there have been no quantitative comparison between experiments and theories since most of the experiments had been focused on $V_{\phi}(0)$ as well as the sign, and theoretical comparisons were only focused on the explanation for the reversal (or bifurcation) of the residual stress. Although the rotation reversal phenomenon is interesting and lead to many theoretical advances for the intrinsic rotation generation mechanisms, the observation of the rotation reversal has been the starting point for intrinsic rotation studies in Ohmic plasma to focus on $V_{\phi}(0)$, particularly over the sign; which could make someone overlook the actual intrinsic rotation characteristics in Ohmic plasmas. More details are covered in the next chapter.

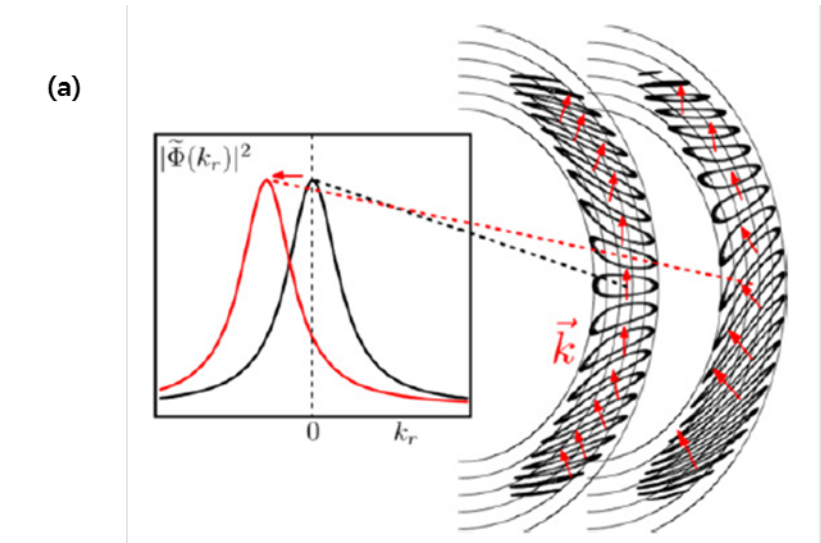

Figure 1.2 Simple pictures of the symmetry breaking mechanisms: (a) spectral shift [50] and (b) mode coupling in spectral dispersion [46].

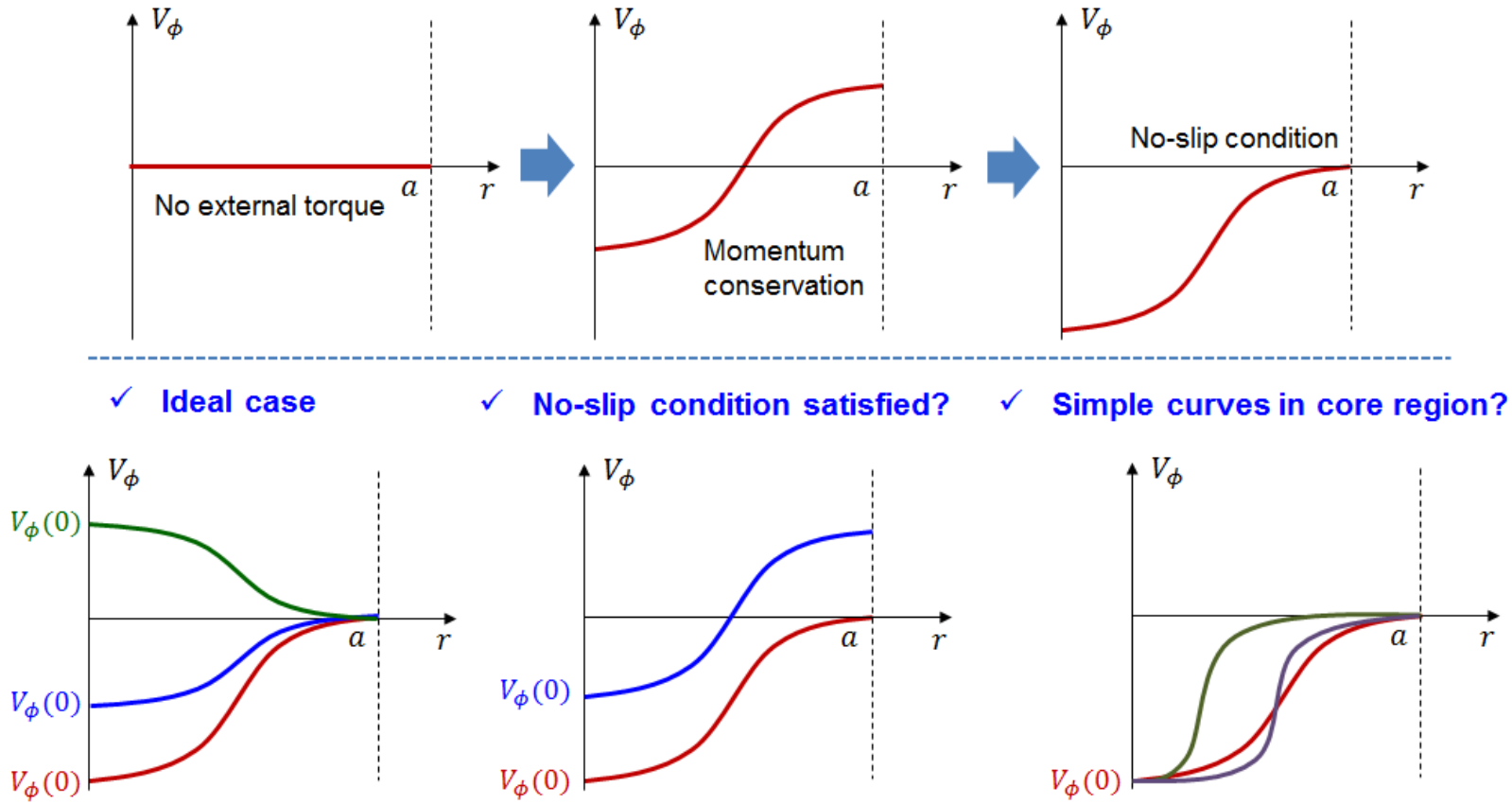

Figure 1.3 Schematic pictures of typical intrinsic rotation generation and several types of intrinsic rotation profiles.

1.4. Objectives and outline of this dissertation

With experiments in various tokamaks and theoretical progresses for the intrinsic rotation, there is no conclusive consensus on physics of intrinsic rotation generation. Even, the intrinsic rotation characteristics in experiments have been not well organized, either by devices or by plasma conditions. It could be due to very complex and diverse mechanisms of the intrinsic rotation, but one of possible reasons is that single parameter for the intrinsic rotation is used without considerations of the intrinsic rotation profiles in detail. In actual, most experimental analysis in various tokamaks (especially in Ohmic plasmas) has been done based on the core intrinsic rotation, $V_\phi(0)$, as described above, which could loss the actual intrinsic rotation characteristics in experiments. As shown in Figure 1.3 (Ideal case), $V_\phi(0)$ could be a good proxy for the intrinsic rotation characteristics in case of the ideal case. The magnitude of $V_\phi(0)$ represents the degree of change in the momentum transport and the sign of $V_\phi(0)$ indicates the direction of the momentum transport. However, if no−slip condition is not satisfied, or the profile is not a simple curves then as shown in Figure 1.3, it is difficult to predict the momentum transport characteristics with only $V_\phi(0)$.

In this research, the intrinsic rotation is studied in KSTAR Ohmic

plasmas based on intrinsic rotation profiles, called profile-based analysis, to capture the intrinsic rotation characteristics well. The characteristics of the intrinsic rotation will be studied by experiments and analyzed based on statistically sufficient databases. Then, to understand the physics of the intrinsic rotation generation, the experimental database will be compared with various theoretical models. Finally, the integrated modelling will be performed to calculate entire profiles of the intrinsic rotation in KSTAR Ohmic plasmas with the selected model.

Chapter 2. Experimental Observation of Intrinsic Rotation in KSTAR Ohmic Plasmas

2.1. Experimental approaches and setups

In KSTAR, the toroidal rotation and the ion temperature can be measured using x-ray imaging crystal spectrometers (XICS) [51] and charge exchange recombination spectrometers (CES) [52]. In the early KSTAR experiments for the intrinsic rotation study, XICS measurement was mainly used since it can be operated without the neutral beam injection which is one of external torque sources. However, its small field of view and a low emissivity in the edge region make it difficult to obtain a complete profile of the toroidal rotation in KSTAR. On the other hand, the CES measurement is reliable in obtaining entire profiles of the toroidal rotation when the neutral beam injection is applied to the plasma only. However, with proper operating conditions, it can be used for the intrinsic rotation study in Ohmic plasmas too. Due to this reason, the experiments in this thesis have been conducted using the CES measurement with the beam blip techniques under fine-tuned operating conditions for the full dissipation of the beam perturbation and the intrinsic rotation measurement in Ohmic plasmas. In addition to, dual measurement

systems of CES and XICS in KSTAR can improve further ability for the intrinsic rotation study. Its application will be dealt in detail.

The experimental approaches for tuning of the beam operating conditions are introduced. In KSTAR, main controllable beam operating conditions are the beam energy/power, the beam duration, and the beam frequency. Figure 2.1 shows the methodology of the intrinsic rotation measurement in KSTAR Ohmic plasmas with the beam blips. As a default setup, the CES measurement requires 10 ms beam injection at least. Therefore, with the beam injection of 20 ms as shown in Figure. 2.1 (a), the CES measurement is performed in two time-slices, and the toroidal rotation profiles can be seen in Figure 2.1 (b). Finally, the intrinsic rotation profile before the beam injection can be approximated by the backward extrapolation method. The blue line of Figure 2.1 (b) shows the intrinsic rotation profile estimated by the linear extrapolation from the toroidal rotation at the first and second frames.

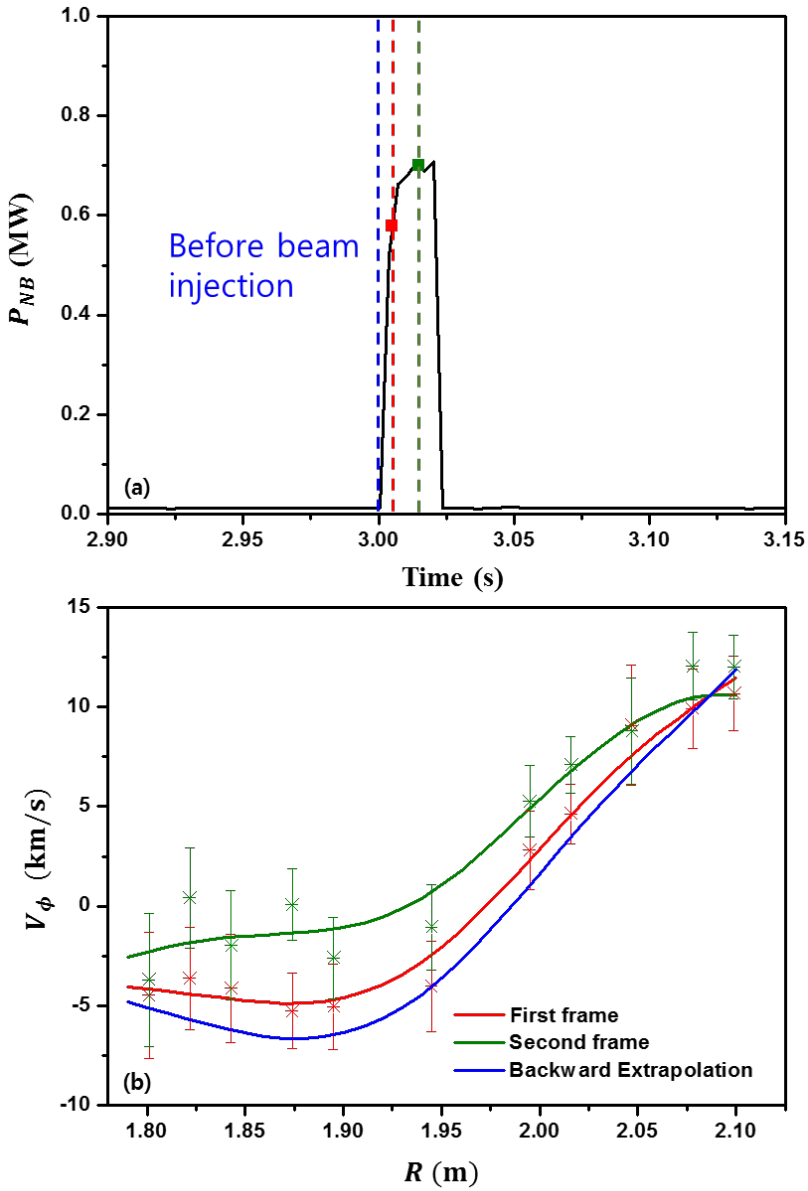

Figure 2.1 (a) An example of the beam blip injection in KSTAR for CES measurement, and (b) toroidal rotation profiles during the beam injection and the intrinsic rotation profile approximated by the backward extrapolation method.

For more database from the limited discharges, it could be useful to apply beam blips more frequently; however, the application of too frequent beam blips can distort the plasma information and provide beam induced toroidal rotation rather than intrinsic rotation even with the backward extrapolation for each beam blips. In the same vein, the beam duration and the beam energy/power have also pros and cons which means optimal operating conditions would exist for a specific experiment propose. Figure 2.2 and 2.3 show beam tuning experiments with different types of the beam blip operating conditions. In the beam blip tuning experiments, two beam sources of NB1 and NB2 were used in a single discharge. Although the footprint of two beam sources are slightly different, it is efficient to test more cases with limited discharges. An example discharge in Figure 2.2 was conducted with plasma current of 600 kA and 70 keV beam energy (0.88 MW beam power), 5 Hz beam frequency, and 20 ms beam duration for NB1 (before 2.5 sec) and 70 keV (0.98 MW), 10 Hz, and 20 ms for NB2 (after 2.5 sec). With 10 Hz beam frequency (from 2.5 s to 4.5 s in Figure 2.2), all plasma properties such as the line-averaged electron density, the core ion temperature, the core toroidal rotation and the stored energy are increased significantly due to the accumulation of the beam blip when each property is compared with reference values at 1.5 sec. On the other hand, with 5 Hz beam

frequency (from 1.5 s to 2.5 s in Figure 2.2), the changes of the line-averaged electron density, the core ion temperature, and the stored energy are less than 10 % of its reference values; which means the accumulation of the beam blip perturbation is not much large. Note that, the core toroidal rotation is still significantly changed approximately from −10 km/s to 0 km/s due to beam blips. It implies that the full dissipation time of the beam blip perturbation could be different between the toroidal rotation and other properties. Another example discharge in Figure 2.3 was conducted with plasma current of 400 kA and 70 keV beam energy (0.88 MW beam power), 3 Hz beam frequency, and 30 ms beam duration for NB1 (before 2.5 sec) and 60 keV (0.76 MW), 3 Hz, 30 ms for NB2 (after 2.5 sec). Although different two beam sources of NB1 and NB2 are used in this discharge, it is observed that there is no significant different between both cases; implying the only important things are operating conditions. Here, although there is no significant change in the ion temperature and the plasma stored energy at the every blips, the line averaged electron density and the toroidal rotation seem not to be fully dissipated even with a low beam power and frequency. Another notable thing is the density perturbation for the low plasma current (400 kA) discharge could be significantly larger than that for the high plasma current (600 kA) discharge.

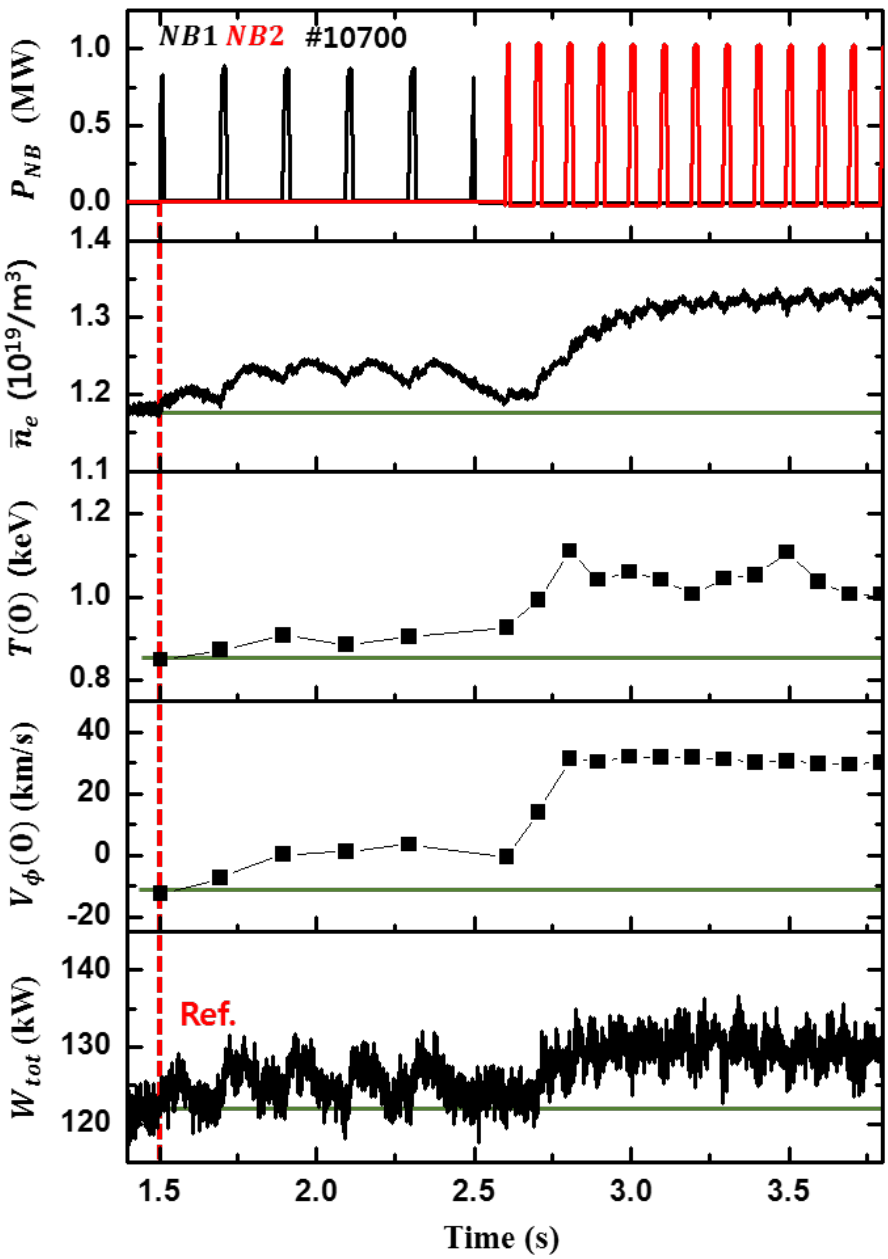

Figure 2.2 Experiment (600 kA) for beam blip tuning in KSTAR.

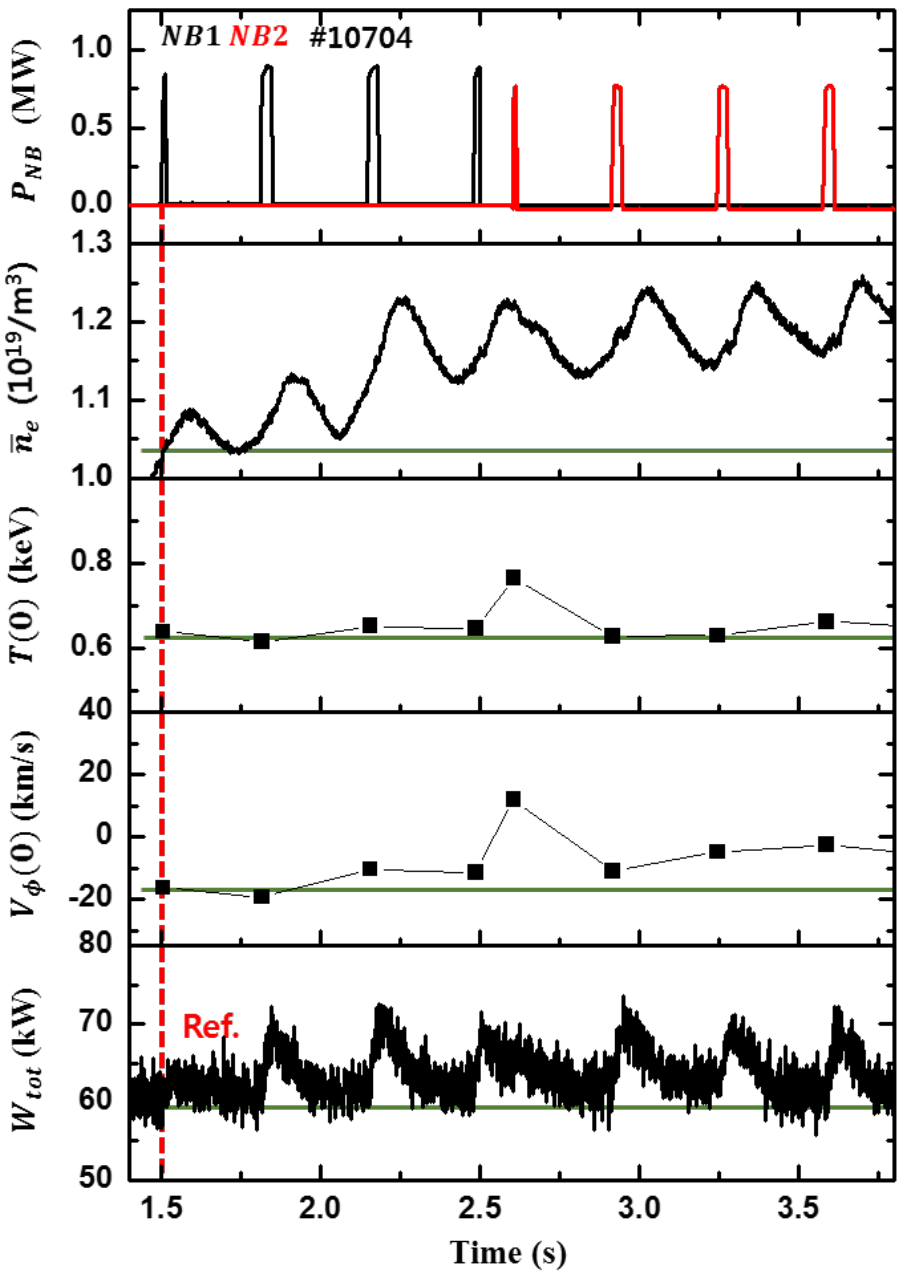

Figure 2.3 Experiment (400 kA) for beam blip tuning in KSTAR.

Unlike the beam blip experiments in other devices, with dual measurement systems of CES and XICS in KSTAR, the beam blip experiments in KSTAR can be used for the perturbative transport analysis too. Figure 2.4 shows a time-trace of experiments for the perturbative transport analysis with the beam blip injection in 400 kA KSTAR Ohmic plasmas. In this discharge, the beam blips were applied with the following conditions: 20 ms beam duration, 2 Hz beam frequency, 70 keV beam energy and 1 MW beam power. Each beam blip induces a few percent (<10%) increase in the plasma stored energy and the line-averaged electron density, but these changes are dissipated within about 200-300 ms. However, the dissipation time of the core toroidal rotation with a large variation seems longer than 300 ms even for simple viewing. For a better resolution, the core toroidal rotation evolution is plotted in Figure 2.5 (a) by summing the evolution from 2 s to 4 s. In Figure 2.5 (a), the beam blip was applied for 20 ms, resulting in an increase in the core toroidal rotation, reaching a maximum value of about 100 ms, as defined in the $\Delta\tau_{peak}$. Then, the core toroidal rotation gradually decreases for 300 ms down to the level before the beam blip had been applied. Here, it is clearly seen that the dissipation time of the beam blip perturbation on the core toroidal rotation ($\Delta\tau_{dissp}$) is about 400 ms in this discharge. Here, the total increase in the core toroidal

rotation is up to 35 km/s and a phase information parameter for the transport analysis, $\Delta\tau_{conf}$, is about 200 ms. One notable thing is the evolution of the core toroidal rotation can be significantly different depending on the operating conditions. Figure 2.5 (b) shows the evolution of the core toroidal rotation with beam blips in 500 kA KSTAR Ohmic plasmas. For both two experiments in Figures 2.5 (a) and 2.5 (b), the toroidal magnetic field is same and the difference of the line-averaged electron density is approximately 10 %. Even with exactly same beam blip conditions, the evolution of the core toroidal rotation is significantly different. For 500 kA discharge in Figure 2.5 (b), the dissipation time of the beam blip perturbation is about 750 ms. More importantly, for this discharge, the total increase in the core toroidal rotation is about 25 km/s which is less than 35 km/s of 400 kA discharge. The dissipation time for the smaller change of the toroidal rotation is about twice as long.

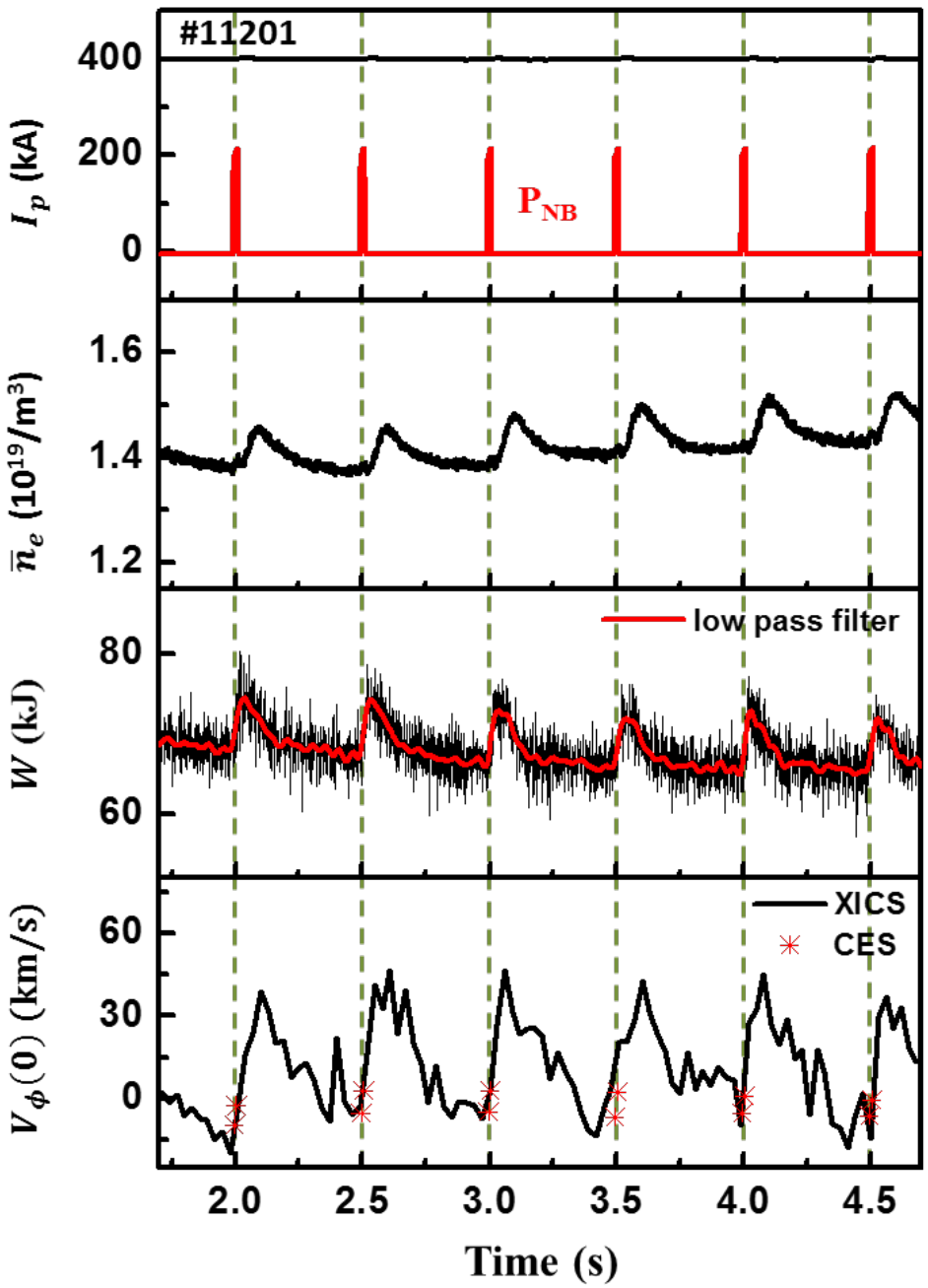

Figure 2.4 Time trace of a beam blip discharge in KSTAR Ohmic plasmas. 2 Hz beam frequency and 20 ms beam duration are used.

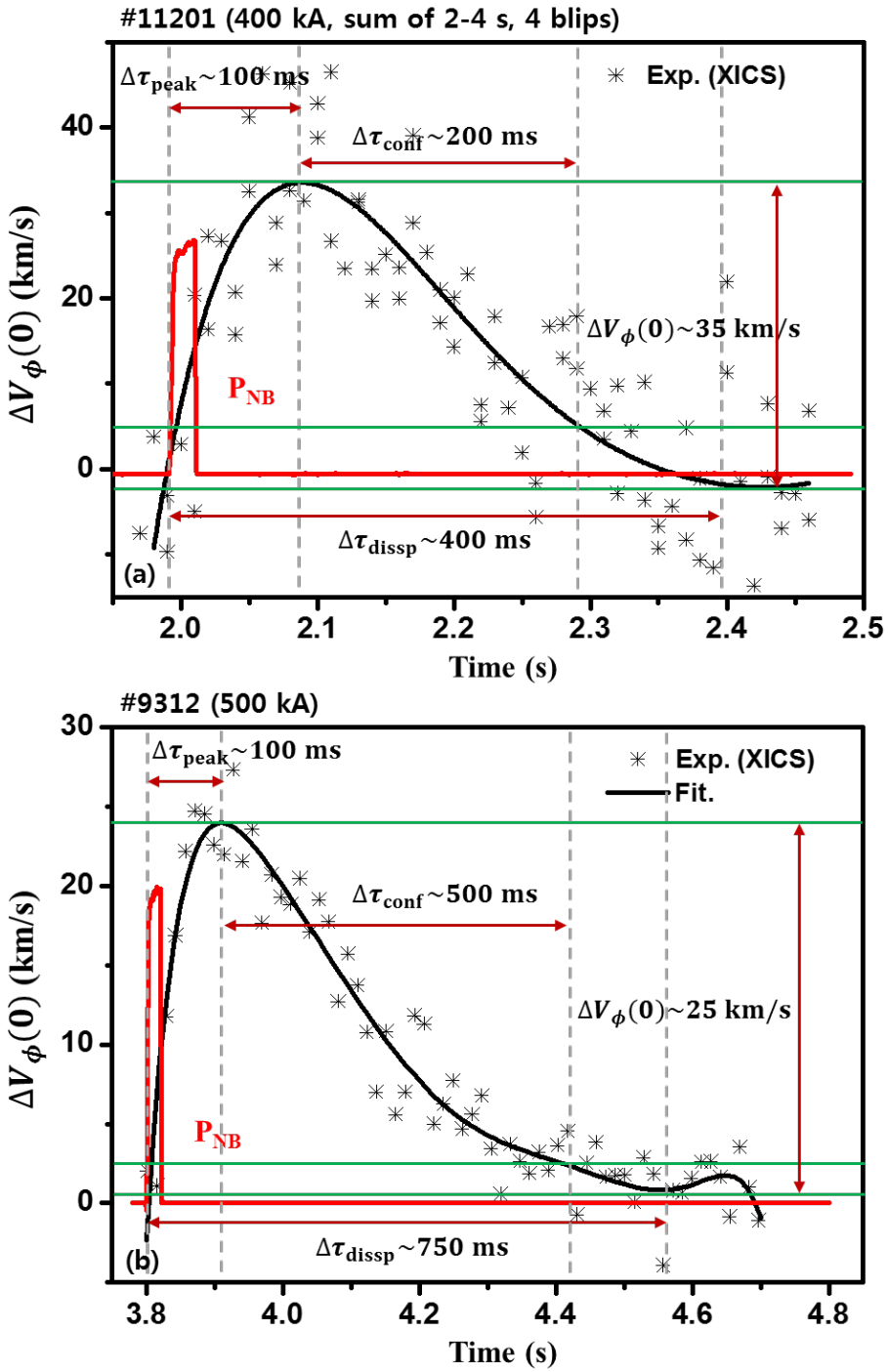

Figure 2.5 Evolution of the core toroidal rotation in the beam blip experiment in KSTAR Ohmic plasmas; (a) 400 kA and (b) 500 kA

In fact, the optimal beam blip conditions for the intrinsic rotation measurement and the perturbative transport analysis depend on plasma operating conditions such as the plasma current and the plasma density. Through trial and error, some rules of the beam blip operating conditions for the intrinsic rotation study have been obtained in KSTAR.

- Beam blip operating conditions for the full dissipation of the beam perturbation to the toroidal rotation cannot be simply determined by comparing other properties such as the temperature and the stored energy.

- Even with a low beam energy and a short beam duration, the beam frequency larger than 2 Hz is not sufficient for the full dissipation of the beam perturbation.

- The toroidal rotation at the first frame of the beam blip is not much different from the intrinsic rotation. It means that the toroidal rotation profiles at the first frame could be used as the approximate intrinsic rotation profiles.

- For the pure intrinsic rotation study, the beam duration of 10

ms (a minimum duration for the diagnosis with a default setup) could be better; whereas 20 ms could be better for the transport analysis study since a relatively large change of the toroidal rotation is required for a sufficient resolution.

By considering above rules, further experiments have been performed for the intrinsic rotation study in KSTAR Ohmic plasmas with the beam energy of 70−100 keV, the beam duration of 10−20 ms, and the beam frequency of 1−2 Hz in KSTAR Ohmic plasmas.

2.2. Typical features of intrinsic rotation profiles

2.2.1. 4 regions of intrinsic rotation profile

In this chapter, typical features of the intrinsic rotation profiles in KSTAR Ohmic plasmas are introduced. In usual, the intrinsic rotation in KSTAR Ohmic plasmas is in the counter−current direction and has a hollow profile regardless of operational conditions such as the plasma current, the toroidal magnetic field, and the plasma shape. Figure 2.6 (a) shows a typical profile of the intrinsic rotation with plasma current of 800 kA, toroidal magnetic field in 2.8 T, a limited plasma configuration with $\kappa \sim 1.4$, and $\bar{n}_e \sim 3.3 \times 10^{19}$. The typical profile can be divided into four regions; core and/or sawtooth region, gradient region, anchor point region, and edge region.

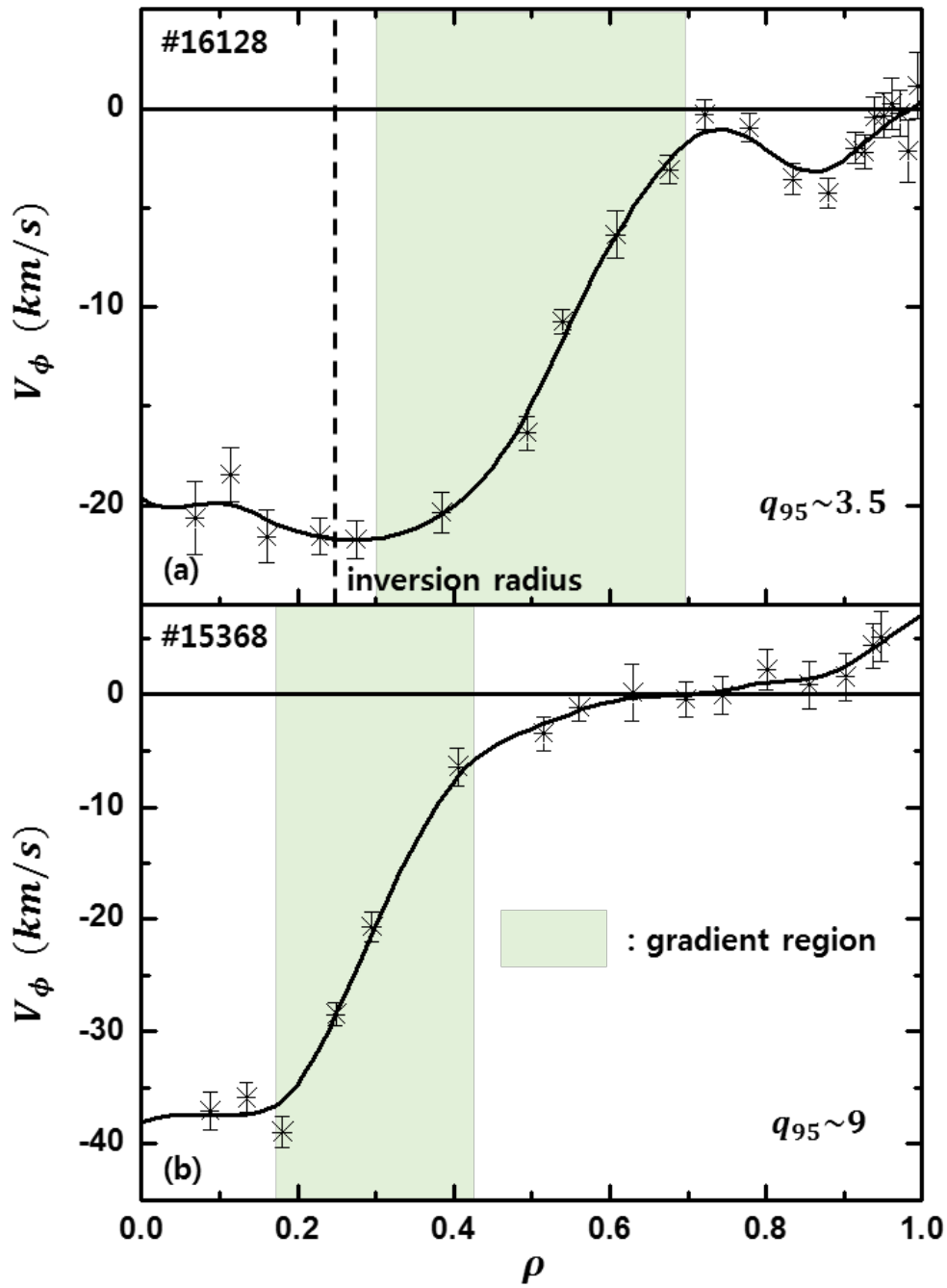

Figure 2.6 Typical feature of the intrinsic rotation profile in KSTAR Ohmic plasmas: (a) w/ and (b) w/o sawtooth activity.

- Core and/or sawtooth region, inside $\rho \sim 0.3$ in Figure 2.6 (a), shows a roughly flat or a somewhat bulging shape. This feature seems to be related to the neoclassical toroidal viscosity associated with the sawtooth activity [53, 54] so that it is localized inside the inversion radius in usual. For normal Ohmic plasma operations in KSTAR, the sawtooth activity is commonly observed so that this feature is also prevalent.

- Gradient region, approximately between $\rho \sim 0.3$ and $\rho \sim 0.7$ in Figure 2.6 (a), shows a steep gradient of the profile so that the region is referred to as the gradient region. For normal discharges in KSTAR Ohmic plasmas, the rotation gradient has a positive value, but the gradient can vary depending on the plasma density and the collisionality.

- Anchor point region, approximately $\rho \sim 0.7$ in Figure 2.6 (a), shows a nearly flat shape again. It is called an "anchor point" since it plays a peripheral boundary for the gradient region. Interestingly, it is far away from the actual plasma boundary. Usually, the toroidal rotation gradient near the anchor point does not change even with the varying of it in the gradient region.

- Edge region, approximately between $\rho \sim 0.7$ and $\rho \sim 1.0$ in Figure 2.6 (a), covers the area between the anchor point and the actual plasma boundary. For the region, the profile and/or the magnitude of the intrinsic rotation seems to depend on various operating conditions. Due to a low resolution around the actual plasma boundary, the edge intrinsic rotation is approximately defined as the intrinsic rotation at $\rho \sim 0.8$ for further analysis on the edge intrinsic rotation.

One notable thing is that the nearly flat shape in core region is also observed in discharges where the sawtooth activity is not observed. In Figure 2.6 (b), the nearly flat shape of the intrinsic is still observed inside $\rho \sim 0.2$. It means that the inner boundary of the gradient region does not origin from the sawtooth activity only although it is predominant in most experiments.

2.2.2. Variance of edge rotation at similar profile shape

In general, the boundary rotation of the limited plasmas would be thought of close to zero rotation regardless of the operating conditions. In KSTAR, however, the non-negligible edge intrinsic rotation is commonly observed and it is very sensitive to operating

conditions and wall conditions even for the limited plasmas. Figure 2.7 (a) shows intrinsic rotation profiles from two discharges with a limited configuration and different toroidal magnetic fields in KSTAR. Both discharges were operated on the same day and other operating conditions were fixed except the toroidal magnetic field. Here, the edge intrinsic rotation is approximately 10 km/s for the 2 T discharge while it is approximately 5 km/s for the 3 T discharge. Although the different of 5 km/s seems to be not large, it is not negligible when considering the usual level of the core intrinsic rotation (<20 km/s). As shown in Figure 2.7 (b), the difference of the edge intrinsic rotation is observed for two discharges operated on different days although both discharges were operated with the nearly same operating conditions. One has approximately 5 km/s of the edge intrinsic rotation and another has approximately −5 km/s of that. By considering that the wall conditions can vary significantly depending on the operating day, the difference of the edge intrinsic rotation could result from the different wall conditions. Note that here, under the similar operating conditions, the difference of the edge intrinsic rotation only appears as a global shift, with no clear difference in the overall profiles.

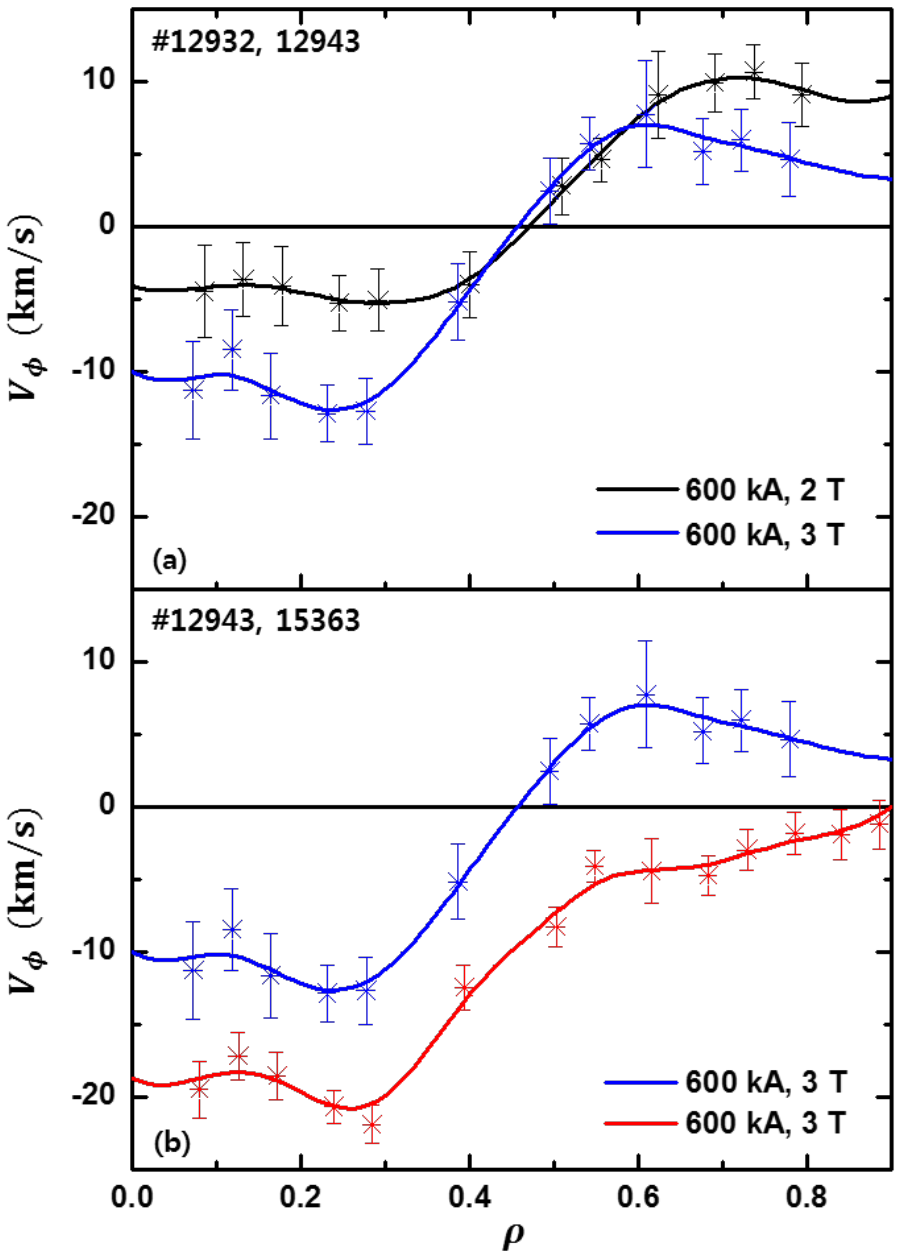

Figure 2.7 Intrinsic rotation profiles with different edge rotation in KSTAR Ohmic plasmas: (a) different toroidal magnetic fields and (b) different operating days.

2.2.3. Variance of profile shape at the same $V_\phi(0)$

It is possible to observe the different intrinsic rotation profiles at the same core intrinsic rotation in KSTAR Ohmic plasmas. In Figure 2.8, two discharges have the same core intrinsic rotation rotation, but its profiles are different. For the red line (400 kA, 3 T), the gradient region is located approximately between ρ~0.2 and ρ~0.6, but it is located approximately between ρ~0.4 and ρ~0.7 for the blue line (800 kA, 2.8 T) and shows an internal transport barrier (ITB) like structure. These observations clearly demonstrate the limitations of the intrinsic rotation analysis based on $V_\phi(0)$ as mentioned in chapter 1.4.

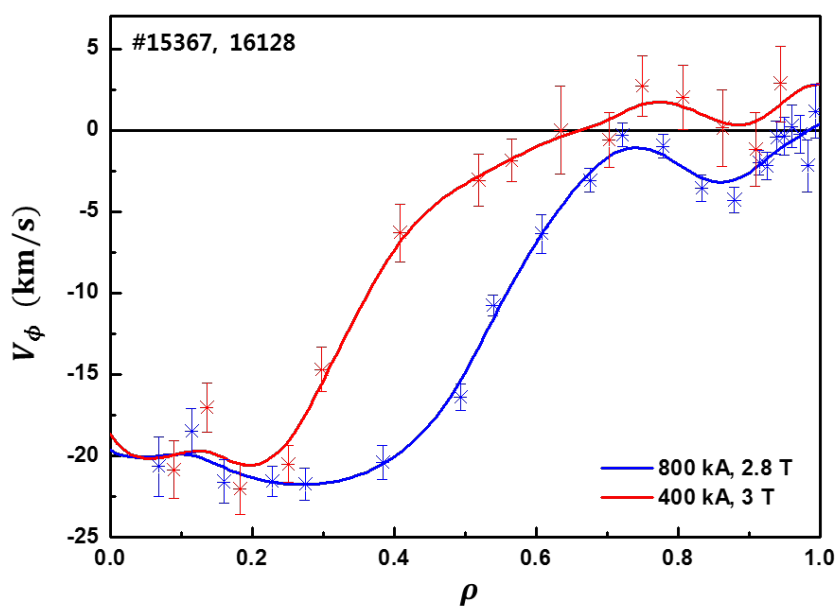

Figure 2.8 Two different intrinsic rotation profiles at the same core intrinsic rotation in KSTAR Ohmic plasmas.

Chapter 3. Analysis of Experimental Characteristics in KSAR Ohmic Plasmas

A quantitative analysis using the entire KSTAR Ohmic plasma database would be helpful for the understanding of the intrinsic rotation. Until the 2016 KSTAR experiment campaign, approximately 300 datasets have been accumulated for this analysis. All of the datasets were obtained from experiments with beam blips where the intrinsic rotation profiles can be measured using CES. Although these datasets are all equipped with the profile measurements of the ion temperature and the intrinsic rotation, not all of the datasets contain other kinetic profiles such as the electron temperature and the electron density. Especially, the electron density profiles are only available in the 2016 campaign datasets, which form less than a half of the total database. The KSTAR Ohmic plasma database covers plasma current (I_{p}) ranging from 400 kA to 800 kA, toroidal magnetic field (B_{T}) from 2.0 T to 3.0 T, and elongation (κ) from 1.3 to 1.8 where most of the plasmas are limited on the central column. This corresponds to the q_{95} range from 2.5 to 10. Further details of the distribution of the operating parameters can be found in Figure 3.1. Unlike the elongation distribution, which is somewhat concentrated,

the distributions of the plasma current and the toroidal magnetic field are a relatively even; this is helpful for non-biased analysis for both properties. Using this database, the profile-based analysis were conducted to determine the characteristics of the intrinsic rotation in KSTAR Ohmic plasmas and its underlying physics. First, the intrinsic rotation characteristics with the plasma density is investigated which covers the rotation reversal phenomenon in the view of the profile-based analysis. Second, the q_{95} dependence of the location of the gradient region and the anchor point region is investigated since the distinction between the gradient region and the anchor point is a unique phenomenological feature of the intrinsic rotation characteristics in KSTAR Ohmic plasmas. Third, the parametric dependence of the normalized toroidal rotation gradient (u') is investigated since u' is a key factor in the indication of the residual stress in the gradient region ($u' \sim -\Pi_{\mathrm{res}}/\chi_\phi$). Fourth, the correlation between u' and momentum transport components is investigated for the further understanding of the u' evolution. For this analysis, the effective collisionality ($\nu_{\mathrm{eff}} \equiv 0.1 Z_{eff} R n_e / T_e^2$) rather than the line-averaged electron density is used, since its correlation with the variation of u' is greater in KSTAR Ohmic plasmas. Here, where Z_{eff} is the effective charge number, which is assumed as 1.5 for all of the datasets due to a limitation of its measurement, R is the major

radius in m, T_e is the electron temperature in keV at the radial point, and n_e is fixed at the line-averaged electron density in $10^{19}\,m^{-3}$. Although Z_{eff} is expected to change depending on the density and the plasma current, the variation of Z_{eff} would not have much effect on the overall trend of the collisionality dependence. Each result is described in the following sub-chapters.

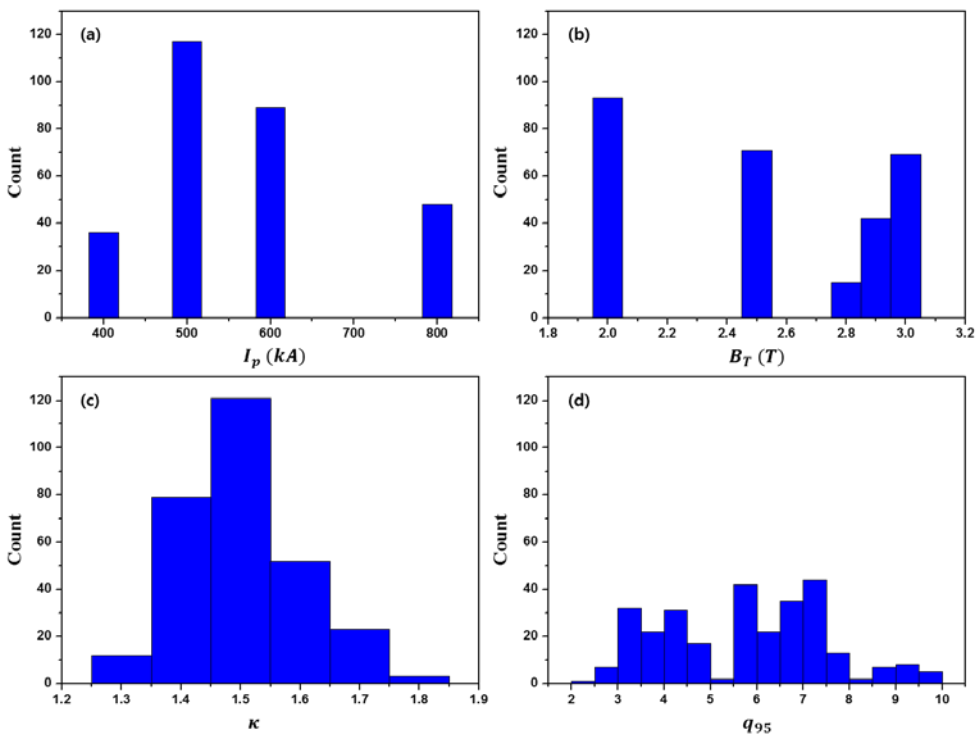

Figure 3.1 Distribution of Ohmic plasma database for the intrinsic rotation study until the 2016 experiment campaign in KSTAR: (a) Plasma current, (b) toroidal magnetic field, (c) elongation, and (d) q_{95}.

3.1. Plasma density dependence of intrinsic rotation profile

One of unsolved issues of the intrinsic rotation in Ohmic plasmas is the rotation reversal phenomenon which is usually observed with the density ramp-up. In KSTAR Ohmic plasmas, the rotation reversal phenomenon is also observed in the density ramp-up experiments. Figure 3.2 shows the temporal evolution of the plasma current, the beam power, the line-averaged electron density, the core electron and ion temperature, and the core intrinsic rotation during the rotation reversal in the discharge #12935. The discharge was conducted with a limited plasma configuration using the beam blip techniques under fine-tuned operating conditions for the full dissipation of the beam perturbation. As the line-averaged electron density increases, the core intrinsic rotation evolves from the co- to the counter-current direction while no significant changes in the electron and the ion temperature are observed. At the same time, the profile evolution of the intrinsic rotation for this discharge is plotted in Figure 3.3 (a). It is noted here that the rotation reversal, a sign change of the core intrinsic rotation, mainly result from a change of the toroidal rotation gradient in the localized region, $0.3 < \rho < 0.6$, while the intrinsic rotation at $\rho \sim 0.6 - 0.7$ stays nearly constant during the rotation reversal in KSTAR Ohmic plasmas. It is the

peripheral boundary, called the "anchor point", for the gradient region as described in chapter 2.2.1. Similar features of the evolution of the intrinsic rotation profiles during the rotation reversal have also been reported for Alcator C-Mod [32] and ASDEX Upgrade [38]; implying the rotation reversal observed in KSTAR Ohmic plasmas is not different from that observed in other devices. Noteworthy is that the rotation reversal can occur without the sawtooth activity in KSTAR although the rotation reversal has been observed with the sawtooth activity in most devices. The experiment presented in Figure 3.3 (b) was conducted with $q_{95}\sim9$, where a clear sawtooth activity signature is not evident. The core intrinsic rotation evolved from 5 km/s to -30 km/s as the density was increased. For the discharges, the gradient region seems to be located in $0.2 < \rho < 0.5$ and the anchor point is approximately $\rho\sim0.5-0.6$. Notably, unlike the discharge in Figure 3.3 (a), the intrinsic rotation at the anchor point changes as well as the core intrinsic rotation even though the magnitude is relatively small. The cause of the change of the anchor point during the rotation reversal in this discharge is not yet clear; however, in any case, the toroidal rotation gradient at the anchor point is nearly zero during the rotation reversal, which would be a better criteria for the anchor point. Here, the most significant change that results in the rotation reversal is the change of the toroidal

rotation gradient in the gradient region. Therefore, it is important to closely examine the characteristics of the gradient region to understand the phenomenon of the rotation reversal.

Conventionally, the rotation reversal implies a bifurcation-like abrupt sign change of the core intrinsic rotation. Inevitably, the definition requires the change of the sign of the intrinsic rotation at the core. With the conventional definition of the rotation reversal, some specific operating conditions such as the plasma current, the toroidal magnetic field, and the plasma shape are required in KSTAR Ohmic plasmas for the rotation reversal. However, further experimental results in KSTAR Ohmic plasmas suggest a doubt about the conventional definition since the sign of the core intrinsic rotation is not an indispensable indicator for the rotation reversal. By considering the continued experiments in some tokamaks including KSTAR, a more general definition of rotation reversal, a large change of the intrinsic toroidal rotation gradient produced by minor changes in the control parameters, was introduced in recent (the experimental results in this thesis contributed to it) to capture the characteristics of the rotation reversal phenomenon [55]. According to the more general definition of rotation reversal, the sign change of the core intrinsic and/or its gradient are not required.

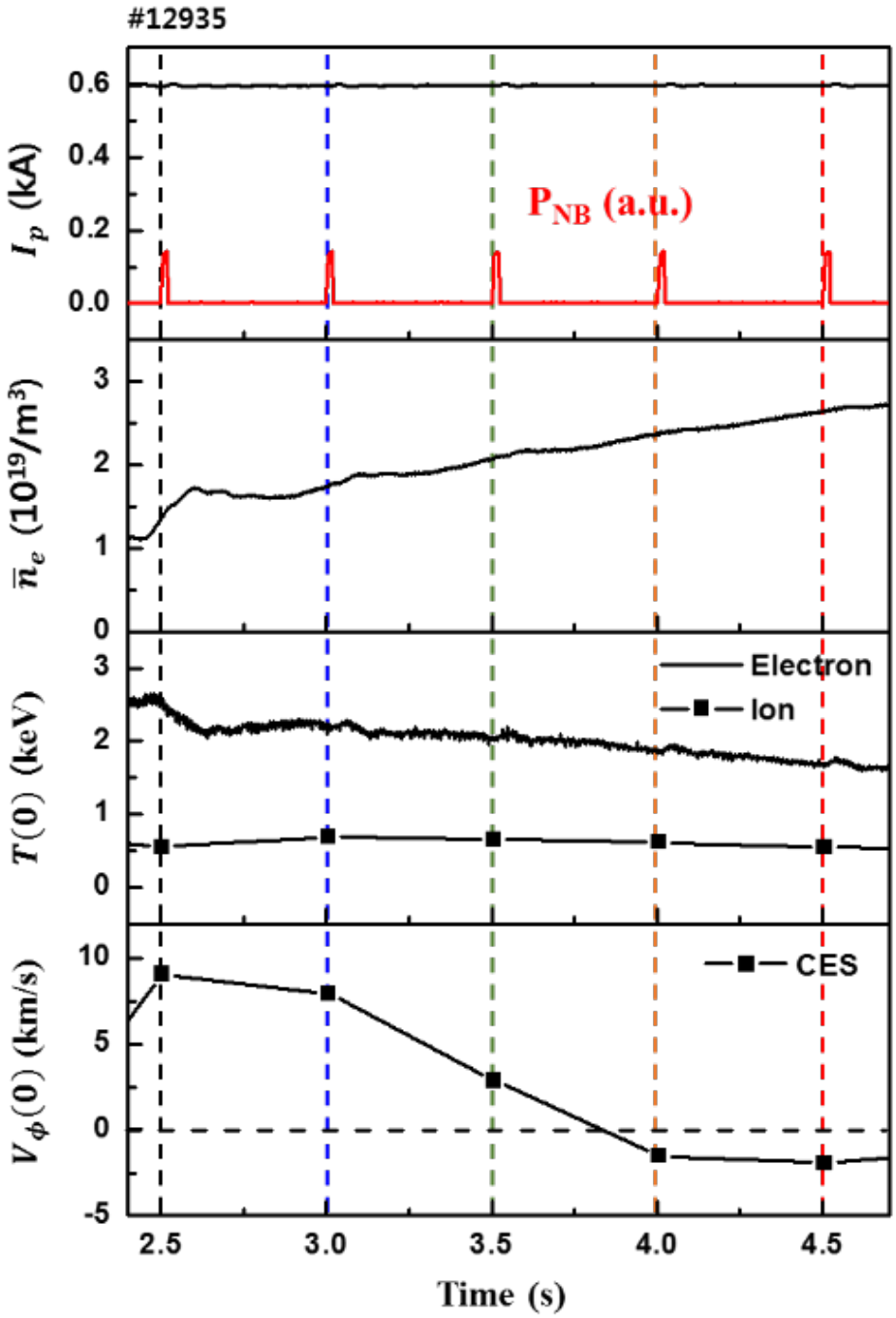

Figure 3.2 Time trace of the rotation reversal discharge#12935 in KSTAR Ohmic plasmas.

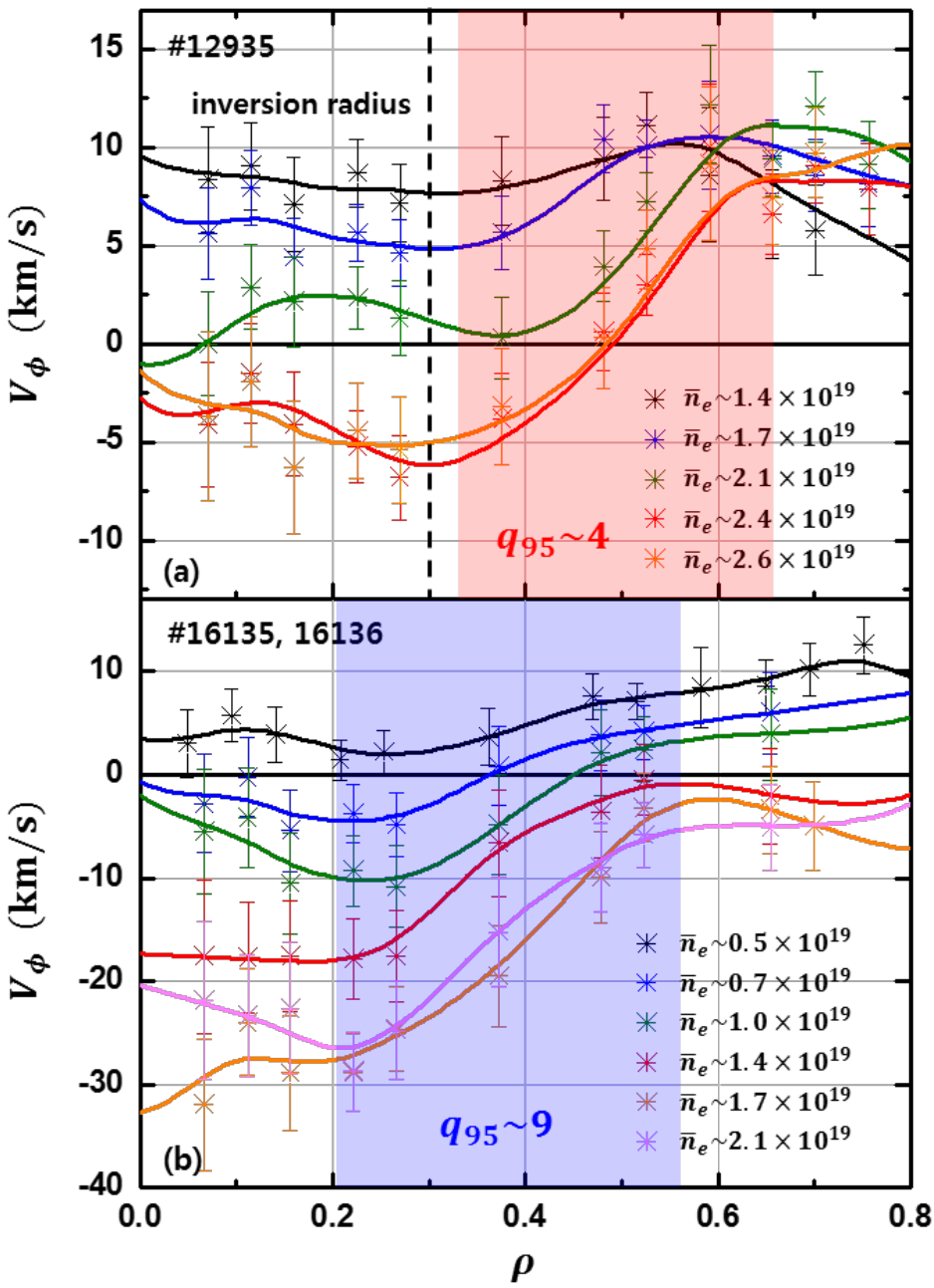

Figure 3.3 Evolution of the intrinsic rotation profiles during the rotation reversal (conventional definition) in KSTAR Ohmic plasmas: (a) w/ and (b) w/o sawtooth activity.

Figure 3.4 shows the evolution of the intrinsic rotation profiles from the discharges, which is applicable for the more general definition of the rotation reversal, but not for the conventional rotation reversal. For these discharges, the crossing of the zero rotation by the core intrinsic rotation is not expected even with the nearly flat shape in the gradient region which is a normal variation as shown in Figures 3.3 (a) and 3.3 (b). Instead, for these discharges, the control parameters of the line-averaged electron density changes only less than 30 % but the normalized rotation gradient ($u' \equiv -(R/v_{th,i})dV_\phi/dr$) changes approximately two to three times at the mid-point of the gradient region. It is noted that, in the phenomenological point of view, a difference is not evident between the discharges in Figures 3.3 and 3.4, except for the sign change of the core intrinsic rotation. Like the conventional rotation reversal with the sign change of the core intrinsic rotation as shown in Figure 3.3, the change of the core intrinsic rotation in Figure 3.4 mainly results from the change of the rotation gradient in the local region as the density increases and the anchor point region is clearly observed. The difference is caused by the difference in the toroidal rotation at the edge and/or the anchor point which can vary depending on the various operating conditions as described in chapter 2.2.2. In other words, it is reasonable to follow the more general definition for the

rotation reversal phenomenon in KSTAR Ohmic plasmas. In this case, the rotation reversal is commonly observed in KSTAR Ohmic plasmas with the increase of the density regardless of the operating conditions such as the plasma current, the toroidal magnetic field, and the plasma shape. Therefore, it is not required to distinguish the rotation reversal from the usual intrinsic rotation in KSTAR Ohmic plasmas. The rotation reversal phenomenon can be treated as just a behaviour of the intrinsic rotation, the change of u' in the gradient region depending on the plasma density and/or the collisionality in KSTAR Ohmic plasmas.

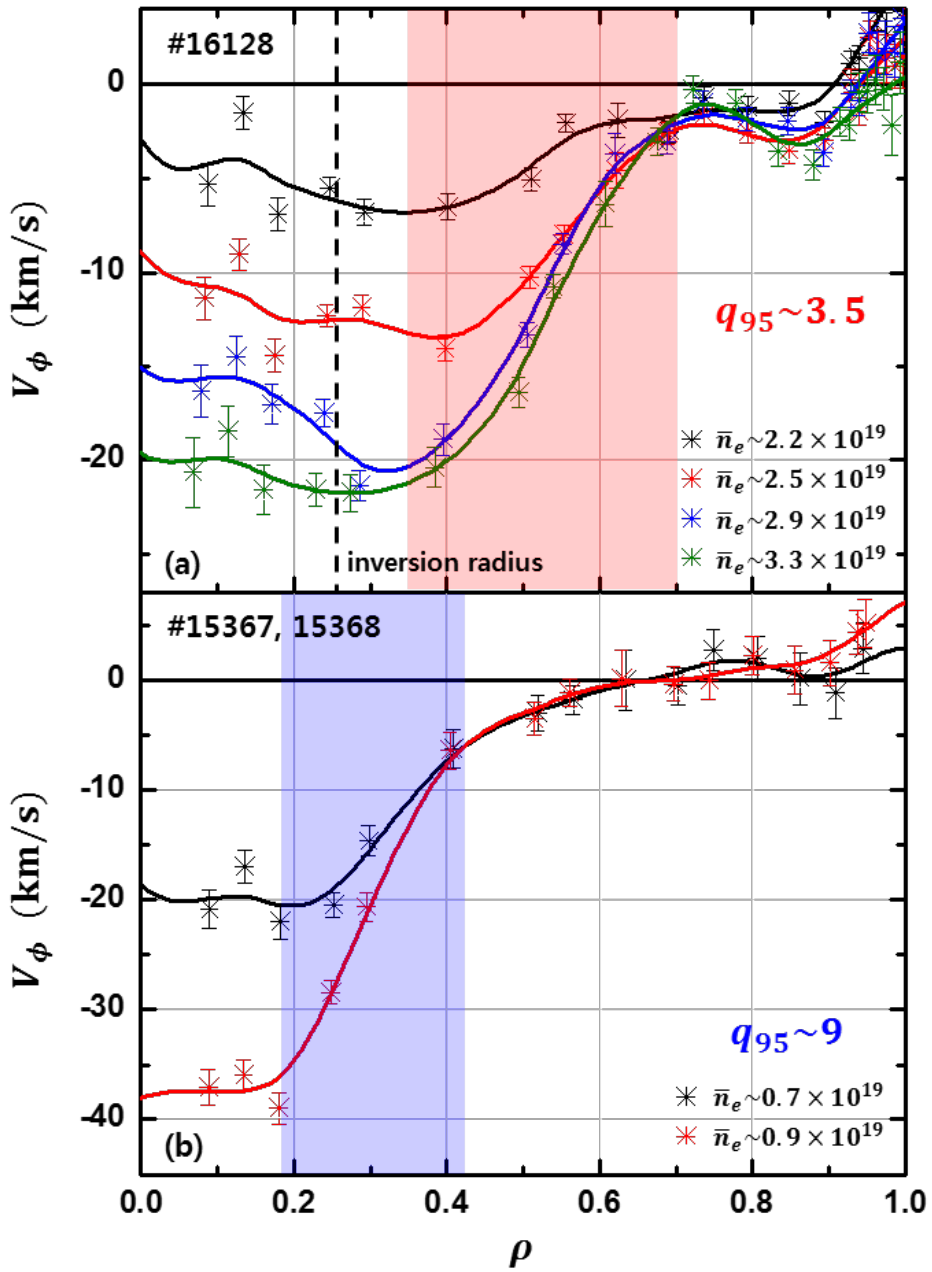

Figure 3.4 Evolution of the intrinsic rotation profiles during the rotation reversal (more general definition) in KSTAR Ohmic plasmas: (a) w/ and (b) w/o sawtooth activity.

3.2. q_{95} dependence of intrinsic rotation profile

As shown in Figures 3.4 (a) and 3.4 (b), it is easily observed that the locations of the gradient region and the anchor point vary with q_{95} in KSTAR Ohmic plasmas. In Figure 3.4 (a), the gradient region seems to be located in $0.4 < \rho < 0.7$ for low q_{95} discharges; whereas, the gradient region seems to be located in $0.2 < \rho < 0.4$ for high q_{95} discharges in Figure 3.4 (b).This trend is clearly captured in the plot of u' versus ν_{eff} for several of the q_{95} subsets, as follows: the low q_{95} subset of $q_{95} < 5$, the mid q_{95} subset of $5 < q_{95} < 8$, and the high q_{95} subset of $8 < q_{95}$. As shown in Figure 3.5, for all of the subsets, there is no clear dependence of u' on ν_{eff} at $\rho = 0.15$; however, at $\rho = 0.25$, u' changes from ~0 to -2 as ν_{eff} increases for the high q_{95} subset, while the other subsets remain at a nearly zero u'. Similarly, the dependence of u' on ν_{eff} is observed at other radial positions for each of the q_{95} subsets. For the mid q_{95} subset, the dependence of u' on ν_{eff} is observed in $\rho = 0.4 - 0.5$ but it is observed in $\rho = 0.5 - 0.6$ for the low q_{95} subsets. From this plot, it is possible to determine the rough locations of the gradient region and the anchor point; for the high q_{95} datasets, the gradient region is roughly located in $0.15 < \rho < 0.5$, it is in $0.25 < \rho < 0.6$ for the mid q_{95} subset and $0.4 < \rho < 0.7$ for the low q_{95} subset. The anchor point is located just outside the

gradient region with a nearly zero gradient. Clearly, the locations of the gradient region and the anchor point seems to depend on q_{95} where the gradient region and the anchor point are closer to the edge for the lower q_{95} subsets. Furthermore, no clear difference is observed in the mid q_{95} subset between the different toroidal magnetic fields and plasma currents, implying that q_{95} would be a more proper parameter to explain the difference in each of the subsets than the toroidal magnetic field and/or the plasma current. It is also noteworthy that the inner boundary of the gradient region is also observed in the high q_{95} datasets as well, where the sawtooth activity is not evident; that is, the inner boundary of the gradient region is not determined by the sawtooth activity only.

Figure 3.6 (a) shows the intrinsic rotation profiles from different q_{95} discharges for a better understanding. The gradient region seems to be located in $0.4 < \rho < 0.7$ for the q_{95}~3.5 discharge; whereas, the gradient region seems to be located in $0.3 < \rho < 0.6$ for the q_{95}~6.0 discharge and $0.2 < \rho < 0.5$ for the q_{95}~9.5 discharge. Figure 3.6 (b) shows the approximate location of the anchor point, ρ_{anchor}, versus q_{95} using the discharges with a relatively clear anchor point in the KSTAR Ohmic plasma database. Clearly, the locations of the gradient region and the anchor point seems to depend on q_{95} where the gradient region and the anchor point get closer to the edge for the

lower q_{95} discharges.

The q_{95} dependence of the locations of the gradient region and the anchor point could be possibly connected to the local q value and/or the magnetic shear ($s \equiv \frac{r}{q}\frac{\partial q}{\partial r}$). Figures 3.7 (a) and 3.7 (b) show the q profiles and the magnetic shear profiles, respectively, that have been calculated from EFIT [56] for the low, mid, and high q_{95} subsets, where the full lines represent the mean value and the error bar shows the standard variation. Then, the q values and the magnetic shear at the anchor point are evaluated in Figures 3.7 (c) and 3.7 (d), where the approximate locations are $\rho = 0.7 \pm 0.025$, $\rho = 0.6 \pm 0.025$, and $\rho = 0.5 \pm 0.025$ for the low, mid, and high q_{95} subsets, respectively. Unlike the above expectations, significant differences of the magnetic shear, as well as the q value at the anchor point, are observed between the q_{95} subsets. This, however, needs to be investigated more delicately with the measurements of the motional stark effect (MSE) and the exact location of the anchor point; for example, the q value at the axis tends to be overestimated according to the comparison with the measured sawtooth inversion radius in KSTAR. The only obvious point here is that the q value and the magnetic shear would be smaller in the gradient region than those at the anchor point.

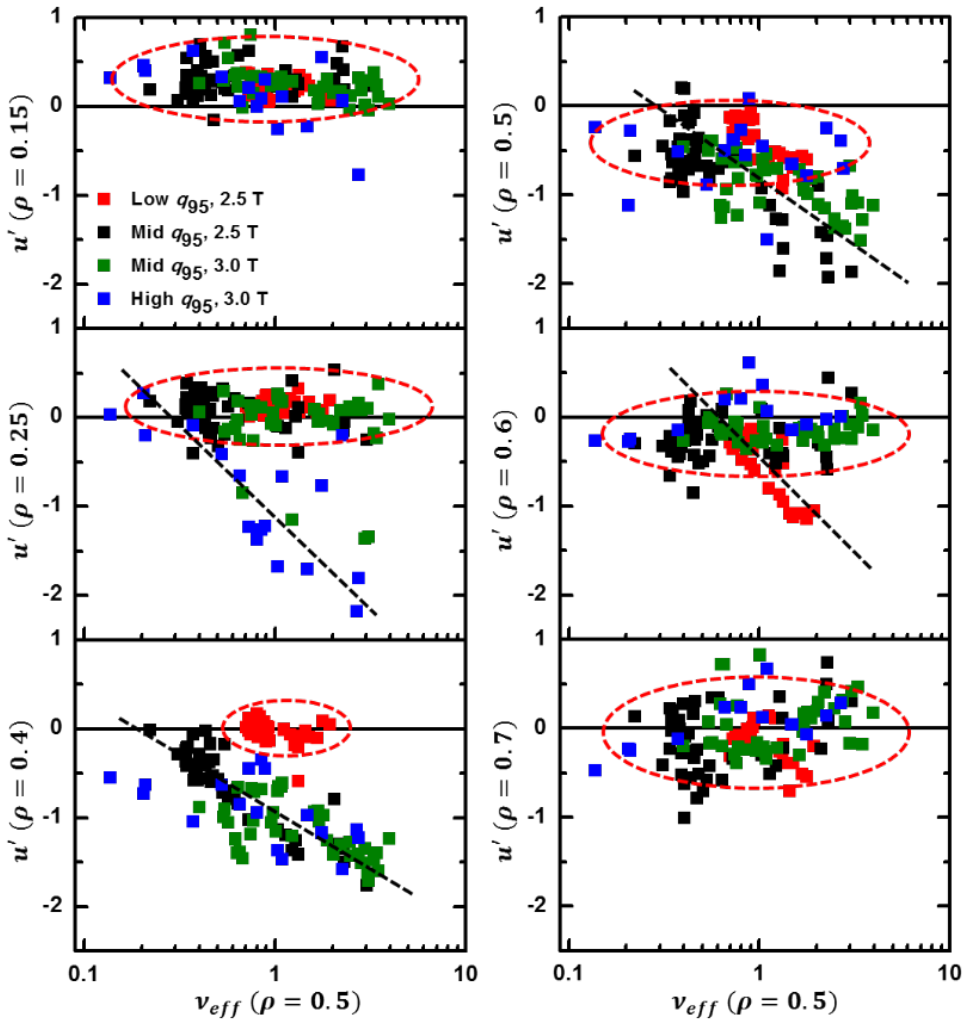

Figure 3.5 u' versus ν_{eff} are plotted in various radial positions from $\rho = 0.15$ to $\rho = 0.7$. q_{95} dependence of the locations of the gradient region and the anchor point in the KSTAR Ohmic plasma database where high, mid, and low q_{95} subsets are presented.

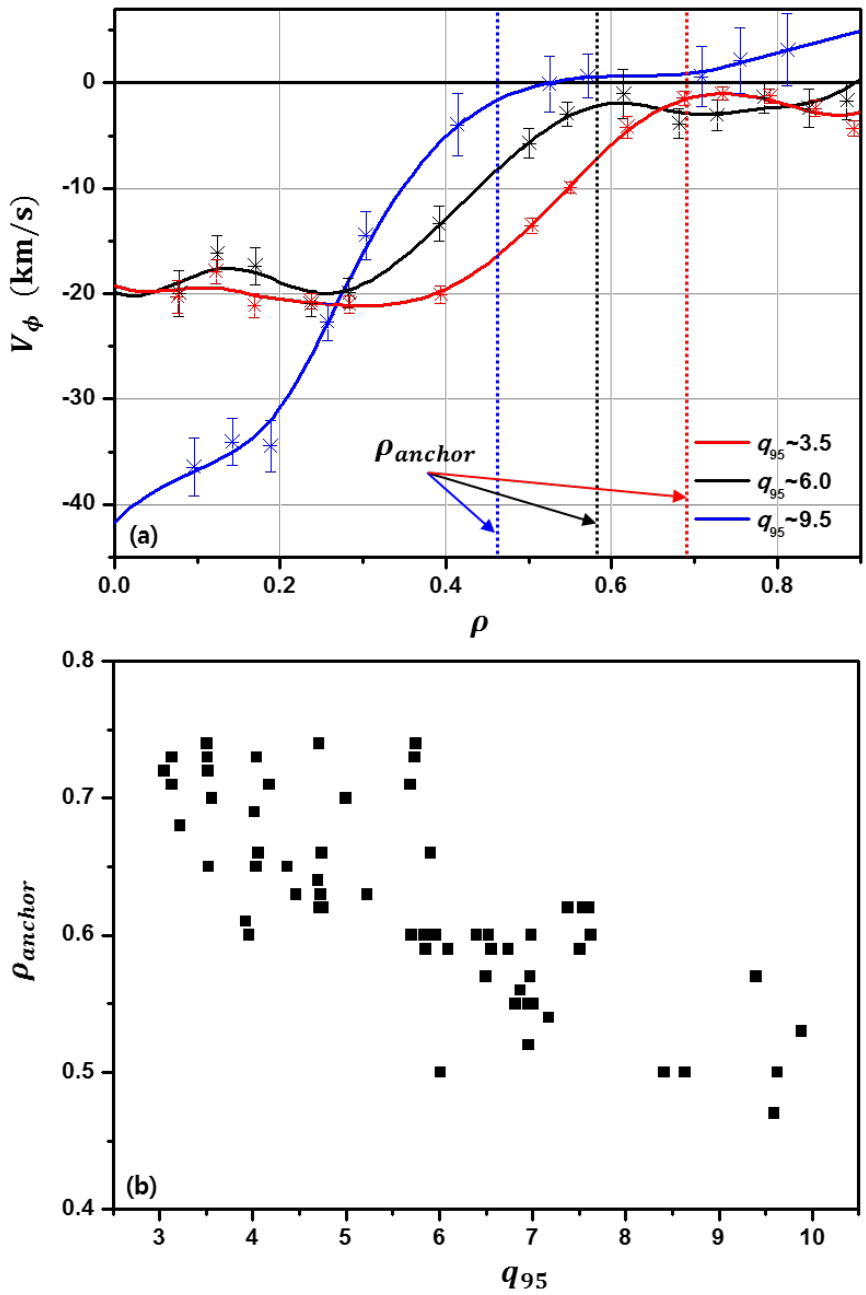

Figure 3.6 (a) Intrinsic rotation profiles from different q_{95} discharges and (b) the approximate location of the anchor point versus q_{95} in the KSTAR Ohmic plasma database.

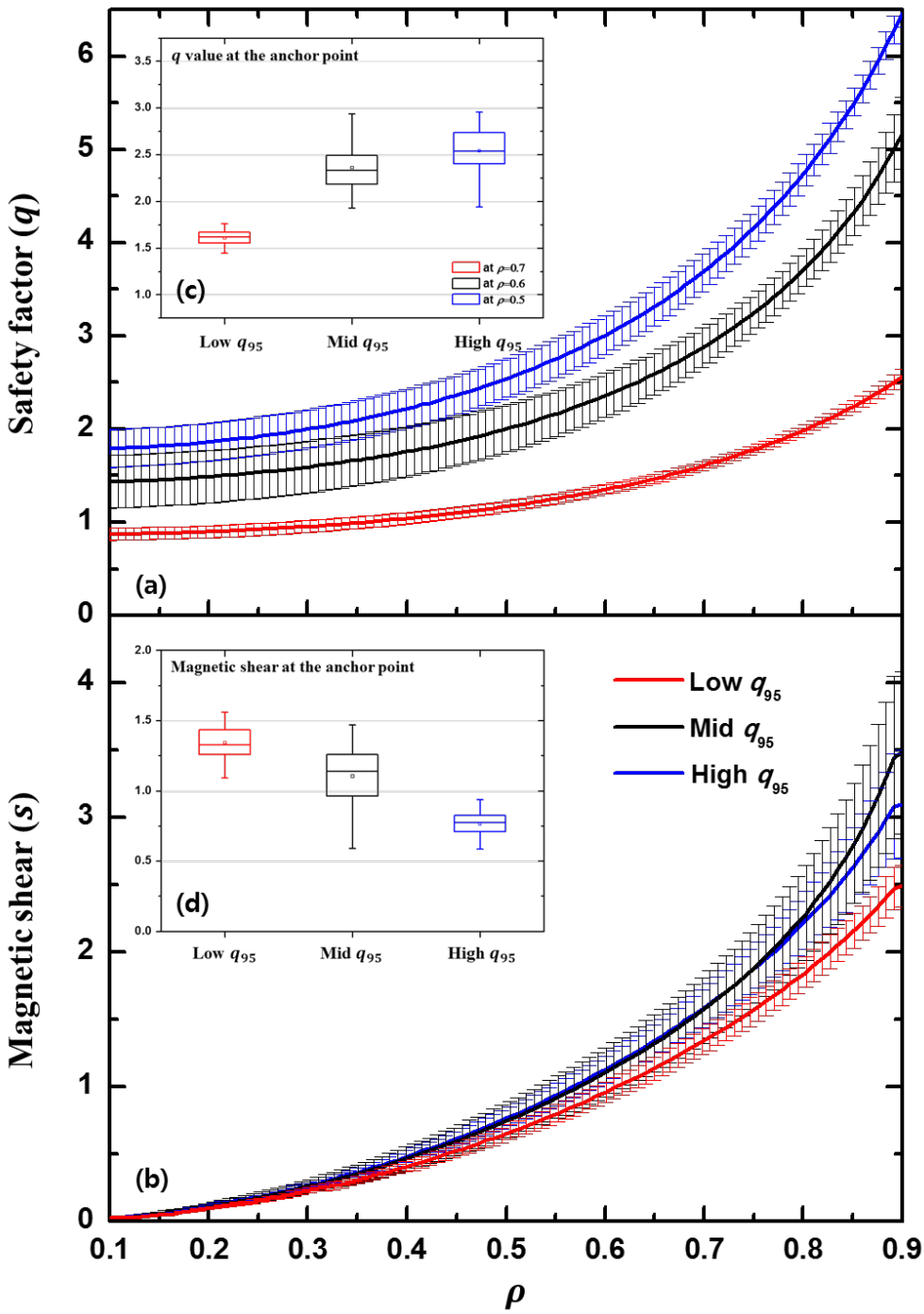

Figure 3.7 (a) q profiles and (b) the magnetic shear profiles with different q_{95} subsets. (c) the q value and (d) the magnetic shear at the anchor point for each of the subsets.

3.3. Parametric dependence of u' in gradient region

The parametric dependencies of u' in the gradient region were investigated to understand the intrinsic rotation characteristics using the KSTAR Ohmic plasma database. By considering the q_{95} dependence of the location of the gradient region, the analysis was performed at $\rho = 0.5$ for the low q_{95} subset, $\rho = 0.4$ for the mid q_{95} subset, and $\rho = 0.3$ for the high q_{95} subset. In Figures 3.8 (a) to 3.8 (d), u' is plotted versus the effective collisionality (ν_{eff}), the normalized logarithmic gradient of the ion temperature (R/L_{T_i}), the electron temperature (R/L_{T_e}), and the electron density (R/L_{n_e}). A dependence of u' on ν_{eff} is clearly observed in Figure 3.8 (a), where u' is inversely proportional to $\log(\nu_{eff})$ regardless of the subsets; this represents the plasma density dependence of the intrinsic rotation as well as the rotation reversal during the density ramp-up. Interestingly, it seems that it is not possible to specify a certain point in time for the rotation reversal in the experimental observations, which implies that the rotation reversal would not be a bifurcation process in KSTAR. Since most of the experiments in this study have been performed in a "comfortable" density regime (less than 50 % of the Greenwald density fraction), only the left side of the U-curves that are reported in Ref. 29 seems to be observed. On the

other hand, u' tends to increase toward the counter direction as R/L_{T_i} increases or R/L_{T_e} decreases, but the degrees of change in R/L_{T_i}, and R/L_{T_e} are small when they are compared with the usual variation of the normalized gradient length. Although the plot is fairly scattered, it looks like there is a certain dependence of u' on R/L_{n_e} in KSTAR, similarly to observations in ASDEX Upgrade [38]. However, caution is needed, since the different q_{95} subsets contribute to the plot where R/L_{n_e} is relatively small for the low q_{95} subset compared with the others, and it is distributed over a larger range for the mid and high q_{95} subsets. Although the correlation between q_{95} and R/L_{n_e} is not clear as shown in Figure 3.8 (f), it will be clarified when a more accurate density measurement is available in KSTAR. Figure 3.8 (e) shows that the increase of ν_{eff} occurs simultaneously with the decrease of T_e/T_i during the density ramp-up.

Here, since the difference of ν_{eff} between the 500-to-600 kA datasets and the 800 kA datasets for the low q_{95} subset is clearly observed, two marks (half-filled square for the 500-to-600 kA datasets, fully-filled square for the 800 kA datasets) are used in Figures 3.8 (a) and 3.8 (e). Two possible reasons should be considered here. First, ν_{eff} does not completely unify vastly different plasma currents. It would be related to assumptions used in

this study such as a fixed Z_{eff} that can be varied with the plasma current and the density. Second, the ECE diagnostic of the 500-to-600 kA datasets is conducted on the high field side (HFS), whereas for most of the 800 kA datasets, the low field side (LFS) is used. Since the normalized radius (ρ) on both sides would not be located on the exact same flux surface, a significant difference between T_e and ν_{eff} ($\propto 1/T_e^2$) will be derived from the slight radial difference with a large R/L_{T_e}. It is noteworthy that nearly-zero or small u' values with a positive sign are observed, while extremely large u' values up to -2 are observed with a negative sign. This small positive u' seems to result from the influence of an outward-extending sawtooth activity.

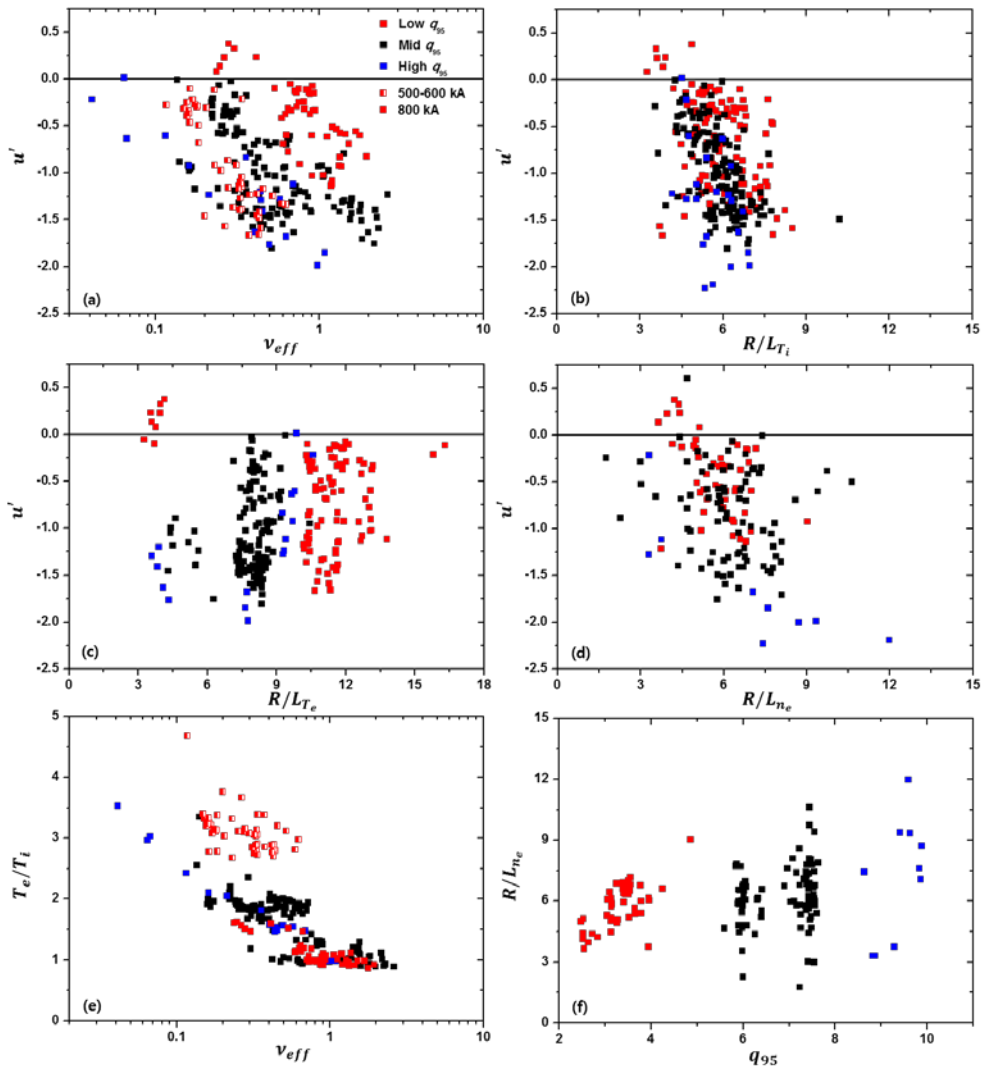

Figure 3.8 Parametric dependences of u' versus (a) ν_{eff}, (b) R/L_{T_i}, (c) R/L_{T_e}, and (d) R/L_{n_e}, and (e) T_e/T_i versus ν_{eff}, and (f) R/L_{n_e} versus q_{95} at the gradient region in the KSTAR Ohmic plasma database. Each colour represents each q_{95} subset.

It is interesting that there is no significant levels of the positive u' in the KSTAR Ohmic plasma database while the negative u' up to -2 is typically observed. Naturally a question arises whether a positive u' can be observed at a much lower collisionality. Due to the lower limit of the density in tokamaks, it is difficult to consistently lower the density in Ohmic plasmas. As an alternative, ECH injection would be useful for an investigation of the low collisionality regime. Figures 3.9 and 3.10 show the relations between $\bar{n}_e$, ν_{eff}, and u', and the linear growth rate (γ) multiplied by the sign of the real frequency (ω_r) for the datasets with and without ECH. To exclude the other factors as far as possible, all of the datasets in these figures are taken at the same plasma current, toroidal magnetic field, and plasma shape of $q_{95} > 7$, where it is not expected that the sawtooth would significantly affect the intrinsic rotation at $\rho = 0.5$. The experimental observation shows that the ECH injection makes ν_{eff} lower than in Ohmic plasmas at the same line-averaged electron density so that a much lower ν_{eff} regime can be explored, as shown in Figure 3.9 (a). Interestingly, u' seems to show a similar trend versus ν_{eff} regardless of the ECH injection in KSTAR as shown in Figure 3.10 (a), while u' versus $\bar{n}_e$ is different for the datasets with and without ECH as shown in Figure 3.10 (b). It is possible to think in a different direction, but the above argument is more convincing when it is

considered that ν_{eff} better unifies the plasma density dependence of the intrinsic rotation than the density in Ohmic plasmas. Here, the positive u' is not clearly observed even for a very low ν_{eff} regime, if the measurement error is considered. The plasma is TEM dominant at $\rho = 0.5$, and the linear growth rate of TEM for the ECH plasma with a lesser ν_{eff} than Ohmic plasmas is large as shown in Figure 3.9 (b). It is clear that a sign change of u' in KSTAR is non-existent even when the collisionality is much lower and/or TEM becomes more unstable.

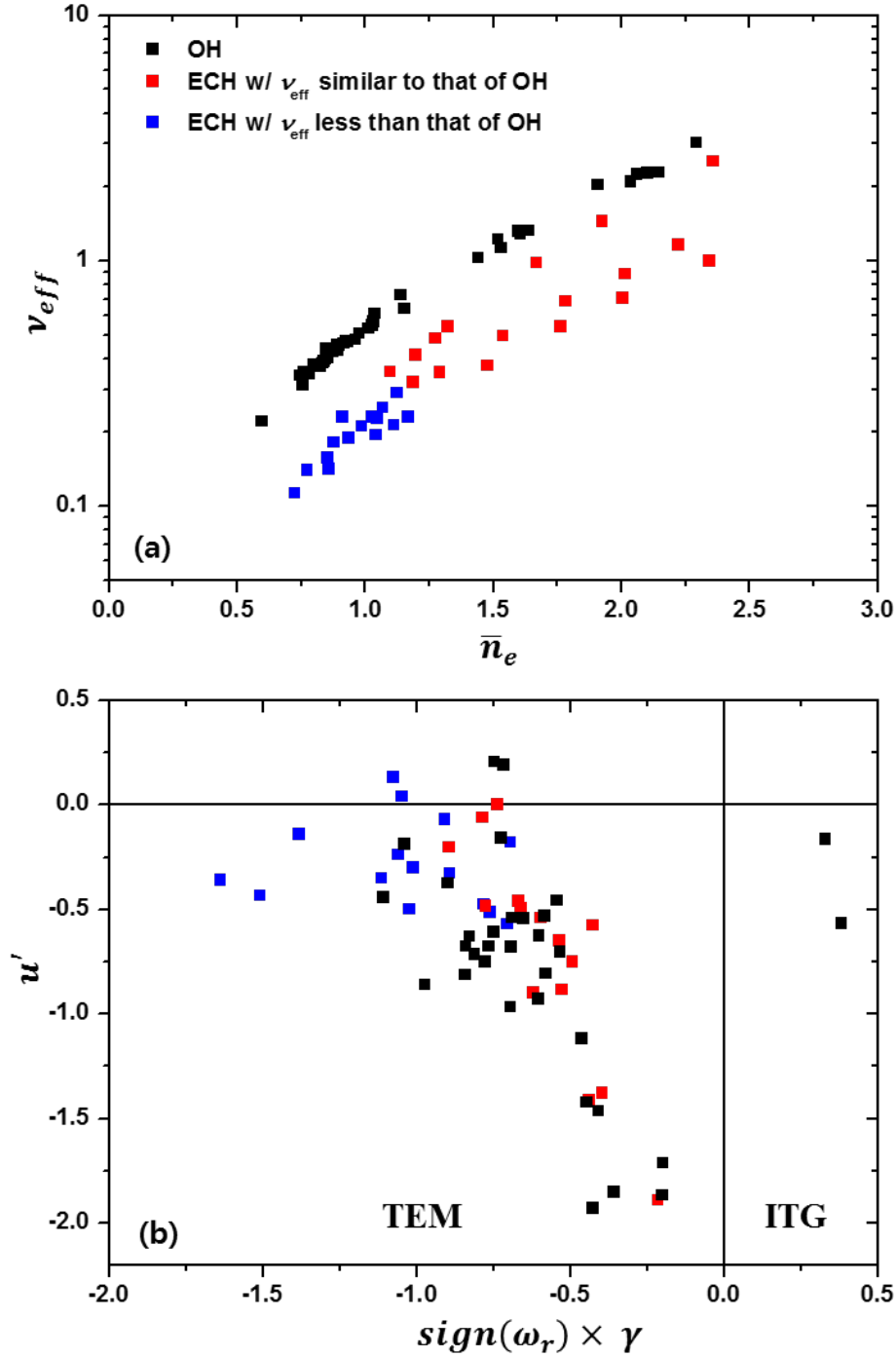

Figure 3.9 Parametric dependence of (a) ν_{eff} on $\bar{n}_e$ and (b) linear growth rate (γ) multiplied by the sign of the real frequency (ω_r) at $\rho = 0.5$ for the datasets with and without ECH in KSTAR.

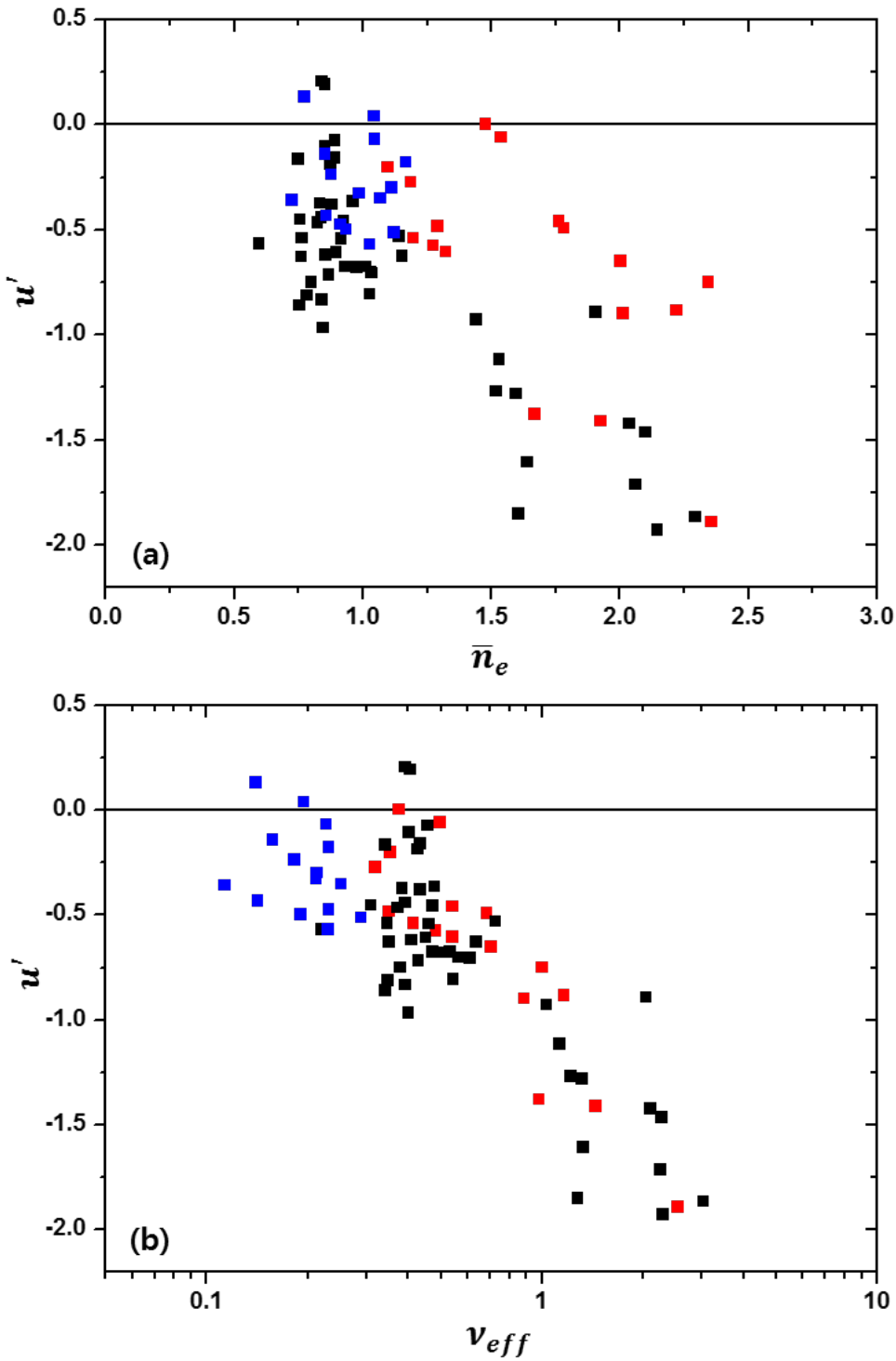

Figure 3.10 Parametric dependence of (a) u' on ν_{eff} and (b) u' on $\overline{n}_e$ at $\rho = 0.5$ for the datasets with and without ECH in KSTAR.

3.4. Correlation between u' and momentum transport components

To understand the behaviour of the intrinsic rotation, it is important to decompose the residual stress and other momentum transport components. The experiments using perturbative methods or balanced momentum sources are very useful for this decomposition analysis [57−62]. In this chapter, the methodology and the results of the perturbative momentum transport analysis in KSTAR Ohmic plasmas were introduced. The perturbative method using the beam blip allows us to perform a transport analysis by implementing the equation (1.6) in the transport code, ASTRA [63] to solve the equation (1.5). In this analysis, the torque from the beam blips can be calculated by using NUBEAM [64]. Since the change in the stored energy and the line−averaged electron density is only of several percent as described in chapter 2.1, we can assume no variations in the momentum diffusivity (χ_ϕ), the normalized pinch (RV_p/χ_ϕ), and the residual stress (Π_{res}) during this period for the beam blip perturbation. For simplicity, the momentum diffusivity and the normalized pinch are assumed to be radially constant and the effect of the sawtooth activity is neglected (a possible profile such as $Pr\chi_i$, where χ_i is calculated from the power balance, can be assumed for

χ_ϕ). The residual stress term can be replaced by the momentum diffusivity, the normalized pinch term, and the stationary profile before the beam blip injection as follows.

$$\Pi_{\text{res}} \equiv \chi_\phi \frac{\partial L_{\phi,init}}{\partial r} - V_p L_{\phi,init} \qquad (3.1)$$

Here, $L_{\phi,init}$ is L_ϕ before the beam blip. This allows us to have two unknowns and two measured quantities so that the unknowns can be obtained. By solving the time evolution of the toroidal rotation considering the beam blip torque, the confinement time of the core toroidal rotation ($\Delta\tau_{conf}$) and the change in the amplitude of the core toroidal rotation (ΔV_ϕ) can be obtained in terms of χ_ϕ and RV_p/χ_ϕ. To find the values to best reproduce the experiment, χ_ϕ and RV_p/χ_ϕ are scanned to minimize the difference ratio (ϵ).

$$\epsilon \equiv \frac{\sqrt{\left(\Delta\tau_{conf,exp} - \Delta\tau_{conf,sim}\right)^2}}{\Delta\tau_{conf,exp}} + \frac{\sqrt{\left(\Delta V_{\phi,exp}(0) - \Delta V_{\phi,sim}(0)\right)^2}}{\Delta V_{\phi,exp}(0)} \qquad (3.2)$$

(exp: obtained from the experiments, sim: from the simulations)

Figure 3.11 shows an example of this transport analysis result in KSTAR Ohmic plasmas. In this case, the best matching values of χ_ϕ and RV_p/χ_ϕ are found to be of about 1.1 m^2/s and -6, respectively.

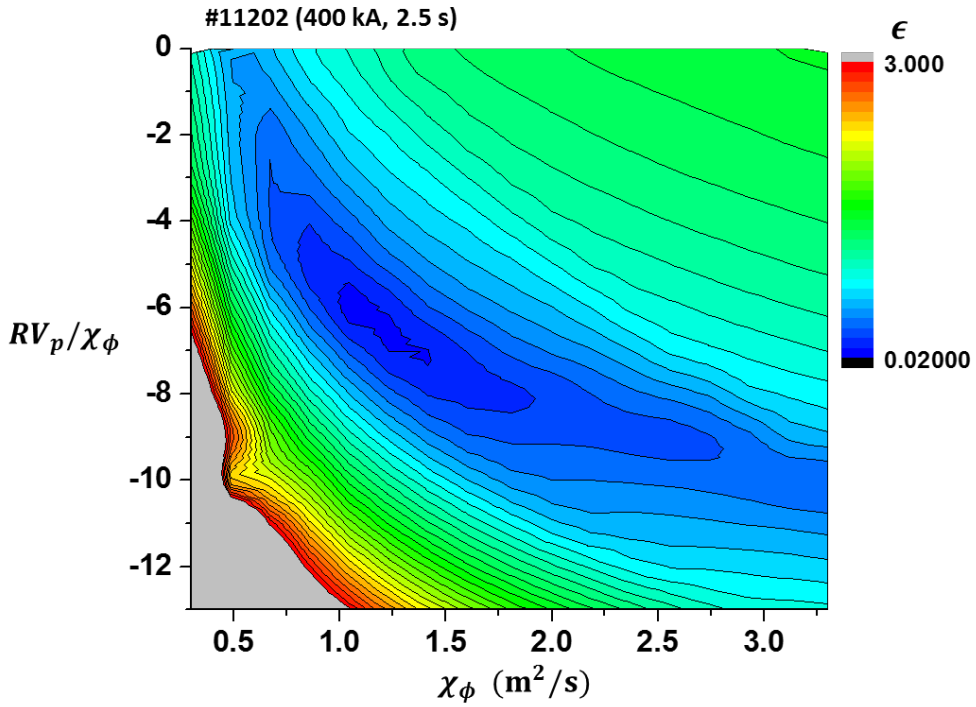

Figure 3.11 Difference ratios (ϵ) versus χ_ϕ and RV_p/χ_ϕ from the transport simulations of the beam blip experiment in the discharge #11202 at 2.5 s at KSTAR

Above analysis is applied for two different u' cases to investigate the mechanism of the u' change. Although $u' \sim -\Pi_{res}/\chi_\phi$ is satisfied in the gradient region, it is impossible to obtain further information for each component with stationary profiles only. Figures 3.12 (a) and 3.12 (b) show the evolution of the core toroidal rotation (black line) measured after beam blips using XICS. It was also compared with the simulated one as follows above analysis methodology. Two cases of u' are compared, as follows: low u' and

high u' cases that are due to the different ν_{eff} values of 0.5 and 1.3 at $\rho = 0.5$. For the two cases, the line-averaged electron densities are $1.0 \times 10^{19}\mathrm{m}^{-3}$ and $1.6 \times 10^{19}\mathrm{m}^{-3}$, respectively. The operating conditions are the same and the background plasma is not much changed after the beam blips. To compare the beam blip effects and the evolution of the core toroidal rotation, the volume integrated beam driven torque ($\mathrm{T_{NB}}$) calculated from NUBEAM is presented in Figures 3.12 (a) and 3.12 (b). The torque exists after the beam duration of 20 ms since the collisional torque contributes to it. For the low u' case, the beam driven torque exists approximately 200 ms after the beam blip while it exists approximately 100 ms for the high u' case. Here, it is clear that the change of the core toroidal rotation ($\Delta V_{\phi}(0)$) due to the beam blip perturbation remains at the much higher rotation (~ 15 km/s) for the low u' case compared with the rotation (<10 km/s) for the high u' case when the beam torque is nearly dissipated (0.25 s, the blue area in Figures 3.12 (a) and 3.12 (b)). Then, the change of the core toroidal rotation is nearly dissipated before the second blip injection for the low u' case while it is not fully dissipated for the high u' case when the second blip is injected. It is clearly observed in the toroidal rotation profile at the second beam blip. For the low u' case, the toroidal rotation profile at the second beam blip is not much different from the profile at the first

beam blip, as can be seen in Figure 3.13 (a). However, the increase of the toroidal rotation is clearly observed at the second beam blip for the high u' case compared with the profile at the first beam blip as shown in Figure 3.13 (b). These findings can be explained by the momentum confinement time ($\propto 1/\chi_\phi$) of the low u' case that is shorter than that of the high u' case, since the evolution of the core toroidal rotation without any torque sources approximately represents the pure momentum transport phenomenon. By solving the time evolution of the core toroidal rotation with the methodology in Ref. 29, the evolutions of the measured core toroidal rotation are well matched with the evolutions of the simulated core toroidal rotation with $\chi_\phi = 0.7\ \mathrm{m^2/s}$ and $\chi_\phi = 0.3\ \mathrm{m^2/s}$ for each case (green line in Figures 3.12 (a) and 3.12 (b)), which correspond to $Pr = 0.5$ and $Pr = 0.3$, respectively.

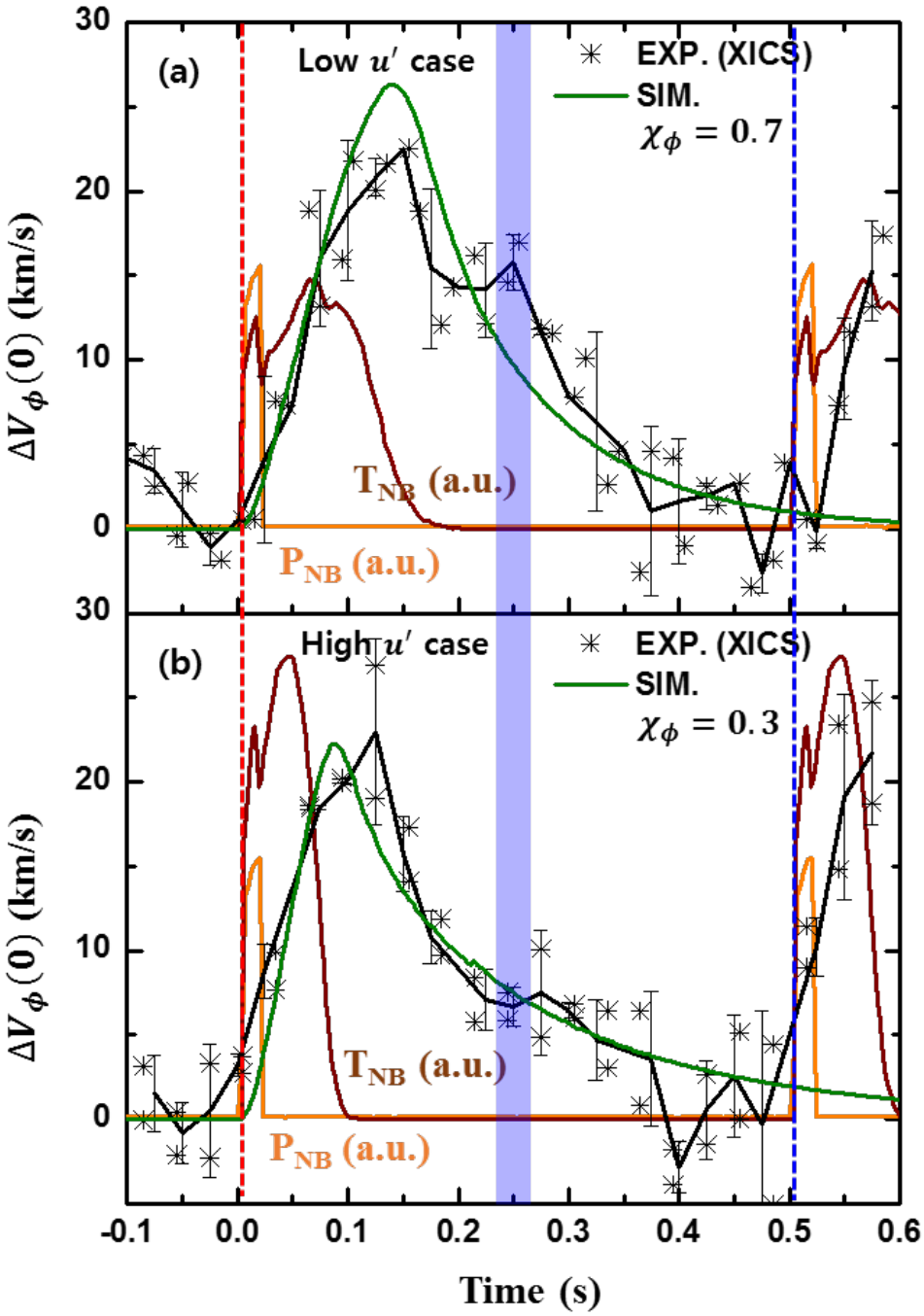

Figure 3.12 (a) to (b) Evolution of the core toroidal rotation after a beam blip perturbation for two different u' cases (low and high cases that are due to different ν_{eff}) compared with the simulation for which $\chi_\phi = 0.7\ \mathrm{m^2/s}$ and $\chi_\phi = 0.3\ \mathrm{m^2/s}$, respectively, are assumed.

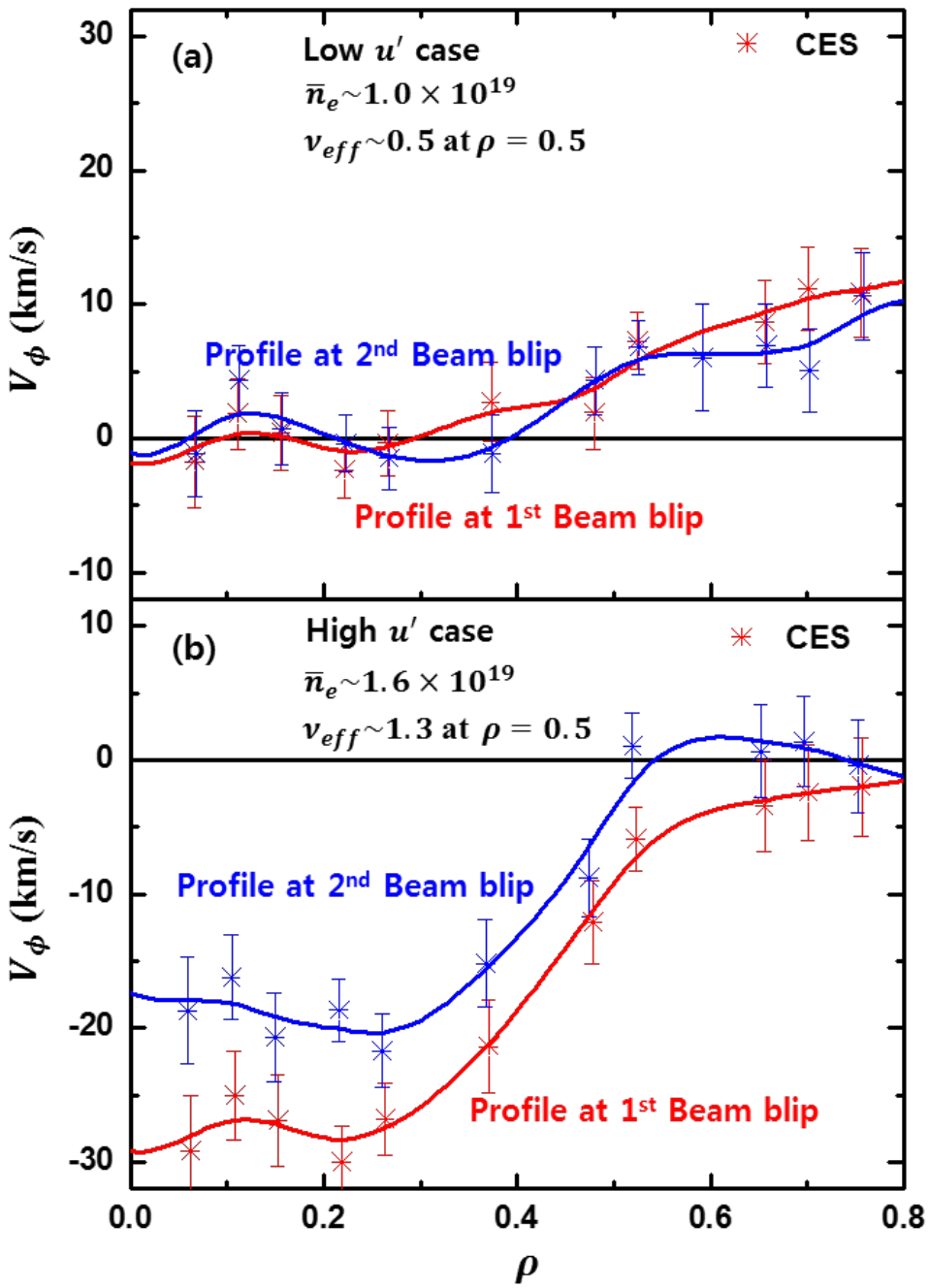

Figure 3.13 (a) to (b) Toroidal rotation profiles at the first (red) and the second (blue) beam blips for the different u' cases.

Figure 3.14 shows the calculated momentum diffusivity (χ_ϕ) and normalized residual stress ($-\Pi_{\rm res}/nmv_{th}$) for 400 discharges and 500 kA discharges in KSTAR Ohmic plasmas. This summarized plot shows that the change of u' in the gradient region could be dominated by the reduction of the momentum diffusivity with the increase of the collisionality rather than the change of the residual stress.

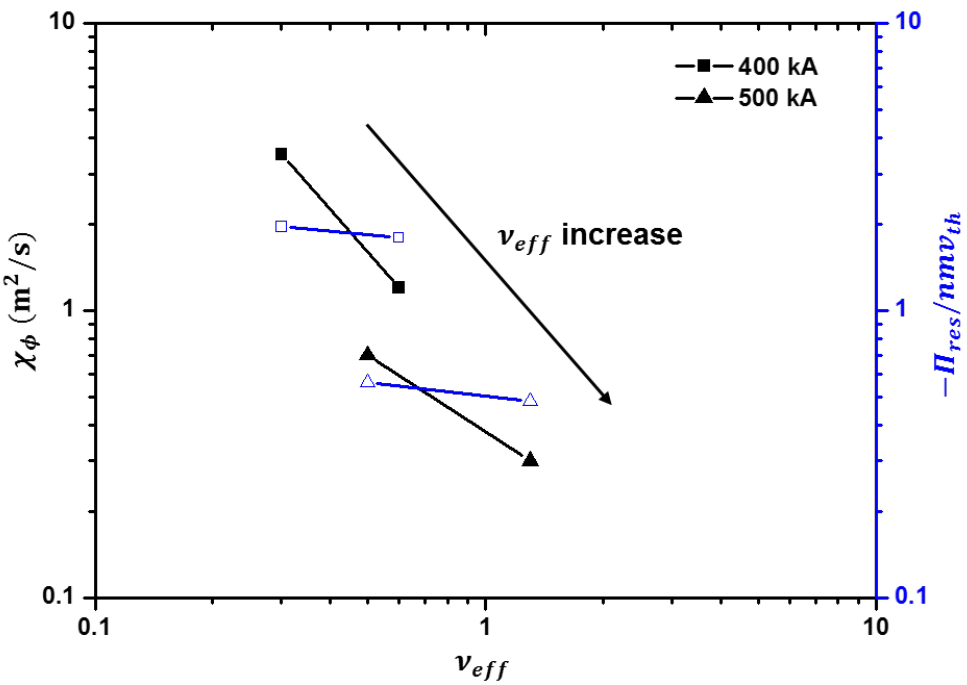

Figure 3.14 Calculated momentum diffusivity (χ_ϕ) and normalized residual stress ($-\Pi_{\rm res}/nmv_{th}$) for 400 discharges and 500 kA discharge in KSTAR Ohmic plasmas.

Chapter 4. Quantitative Comparison of Experimental Data with Theoretical Models

4.1. Neoclassical transport model

For the neoclassical theory [65], the toroidal rotation profiles is obtained by assuming the zero radial momentum flux. Here, the toroidal rotation can be generated by the gradient of density and temperature. Its possibility for the intrinsic rotation in KSTAR Ohmic plasmas was checked by using a simplified formulation for the neoclassical flow. Without any additional momentum sources, the toroidal rotation gradient can be written as follows from a two fluid treatment [66];

$$u' \cong 0.107 K_2 \frac{q^2}{R v_{th}} \frac{T_i}{e B_\theta} \left(\frac{R}{L_{T_i}} \right)^2 \qquad (4.1)$$

Here, K_2 is -1.83 for PS regime and 1.17 for banana regime. Figure 4.1 shows the calculated u' from the equation (4.1) and the measured u' at $\rho = 0.5$ with a subset of the KSTAR database which has all kinetic profiles. $\rho = 0.5$ is selected as the location that can effectively capture the change of u' since most of the datasets used

in this analysis are included in the low and mid q_{95} subsets. The result shows that the neoclassical transport model cannot present a sufficient magnitude of u' to compare with the measured u' in the gradient region. The magnitude of the measured u' is up to 1.5, but that of the calculated u' from the neoclassical transport model is always less than 0.5. Even if we consider $K_2 = 1.17$ in this calculation, the conclusion will not change.

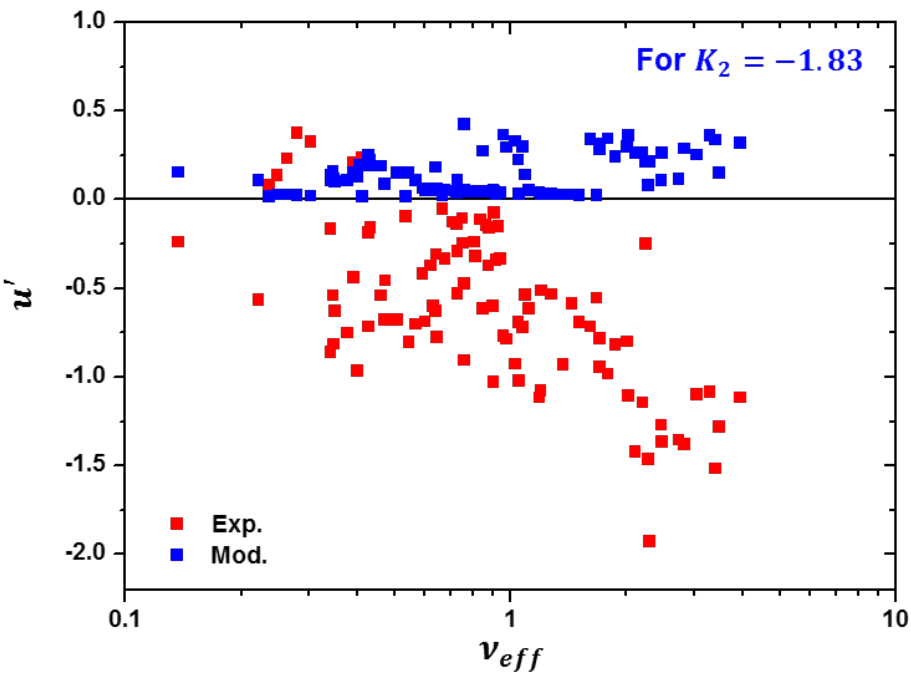

Figure 4.1 Calculated u' from the neoclassical transport model and the measured u' versus ν_{eff} at $\rho = 0.5$, represented as blue and red squares, respectively, in the selected KSTAR database.

4.2. Turbulent transport model

As mentioned in chapter 4.1, the neoclassical transport model prediction seems to be not sufficient to explain the experimental observation of the significant magnitude of u' in KSTAR Ohmic plasmas. In recent years, there have been a lot of theoretical advances for the intrinsic rotation mechanisms associated with the turbulent transport, which include a specific symmetry breaking mechanism. Here, we compared some of the frequently mentioned mechanisms related to the turbulent transport.

4.2.1. Turbulence mode transition model

As described in chapter 3.1, the change of u' in the gradient region with the increase of the density and the collisionality has been referred as the rotation reversal in the conventional view. In most devices, the co- to the counter-current rotation reversals are observed near the LOC to SOC transition [27, 29, 32, 34, 38]. Based on the observations, it has been suggested that a change of the most dominant turbulence from TEM to ITG mode would be a key mechanism for the rotation reversal phenomenon [34-37, 39]. In experiments, analysis of the fluctuation spectra can be useful in an evaluation of the turbulence characteristics since both of the micro-

instabilities contribute to the spectra [67, 68]. The fluctuation spectra have been measured in KSTAR during the rotation reversal using multi-channel microwave imaging reflectometry (MIR) [69]. Figure 4.2 shows the measured fluctuation spectra in the discharge #12935 that are represented in Figure 3.2. It is notable that Quasi-coherent (QC) modes with tens of kHz frequency are observed at $\rho \sim 0.3$ in the middle of the rotation reversal phenomenon (3.4 s with $\bar{n}_e \sim 2.1 \times 10^{19} m^{-3}$ and $\nu_{eff} \sim 0.25$ in Figure 4.2), but then they disappeared as the density and the collisionality increase. Recent reports stated that the QC modes in the fluctuation spectra would be linked to the TEM instability [70-73]; therefore, the observation of the QC mode in the middle of the rotation reversal is likely to indicate that the plasma is still TEM dominant at that time. It means that the change of u' in the gradient region with the increase of the density and the collisionality would not be related to the turbulence mode transition.

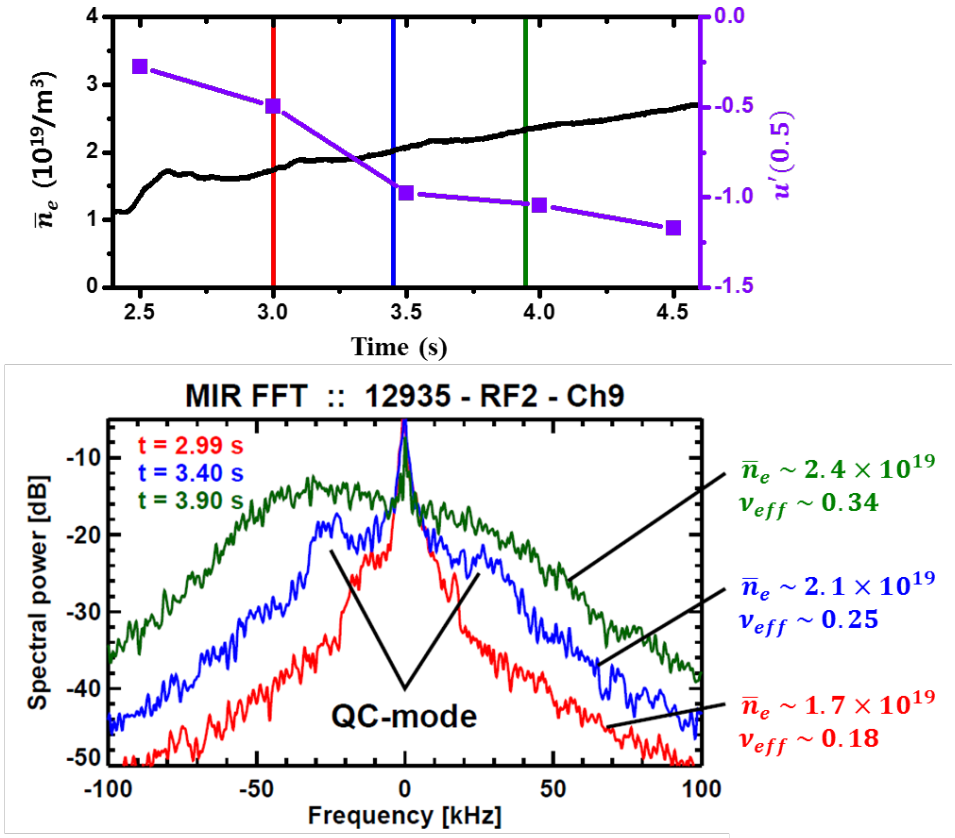

Figure 4.2 Fluctuation spectra from the discharge #12935 in KSTAR. QC modes are observed at tens of kHz frequency at 3.4 s with $\bar{n}_e \sim 2.1 \times 10^{19} m^{-3}$ and $\nu_{eff} \sim 0.25$, but then they disappeared as the density and the collisionality increase.

As another useful methodology for the investigation of the turbulence characteristics, linear gyrokinetic calculations were carried out using GKW [74]. With the available datasets for this analysis, u' and ν_{eff} versus the linear growth rates ($R\gamma/v_{th,i}$) at $\rho \sim 0.5$ are plotted in Figure 4.3. In Figure 4.3, the linear growth rates

(γ) represent the positive value through a multiplication of the sign of the real frequency (ω_r). The negative linear growth rates consequently imply that the plasma is unstable and TEM dominant, whereas the positive growth rates mean the ITG mode is a dominant unstable mode. The stable mode appears as 0. The calculations were conducted with the real plasma geometry and the measured kinetic profiles using assumptions of electrostatic, kinetic electrons, collisional plasmas, and $k_y\rho_i = 0.3$. In Figure 4.3, TEM is dominant at $\rho = 0.5$ in most of the cases; however, their growth rate becomes smaller as the collisionality increases and u' increases in the negative direction. All of the above described analysis implies that the transition of the dominant turbulence mode from TEM to ITG may not be a triggering mechanism of the change of u' and/or the rotation reversal in KSTAR Ohmic plasmas.

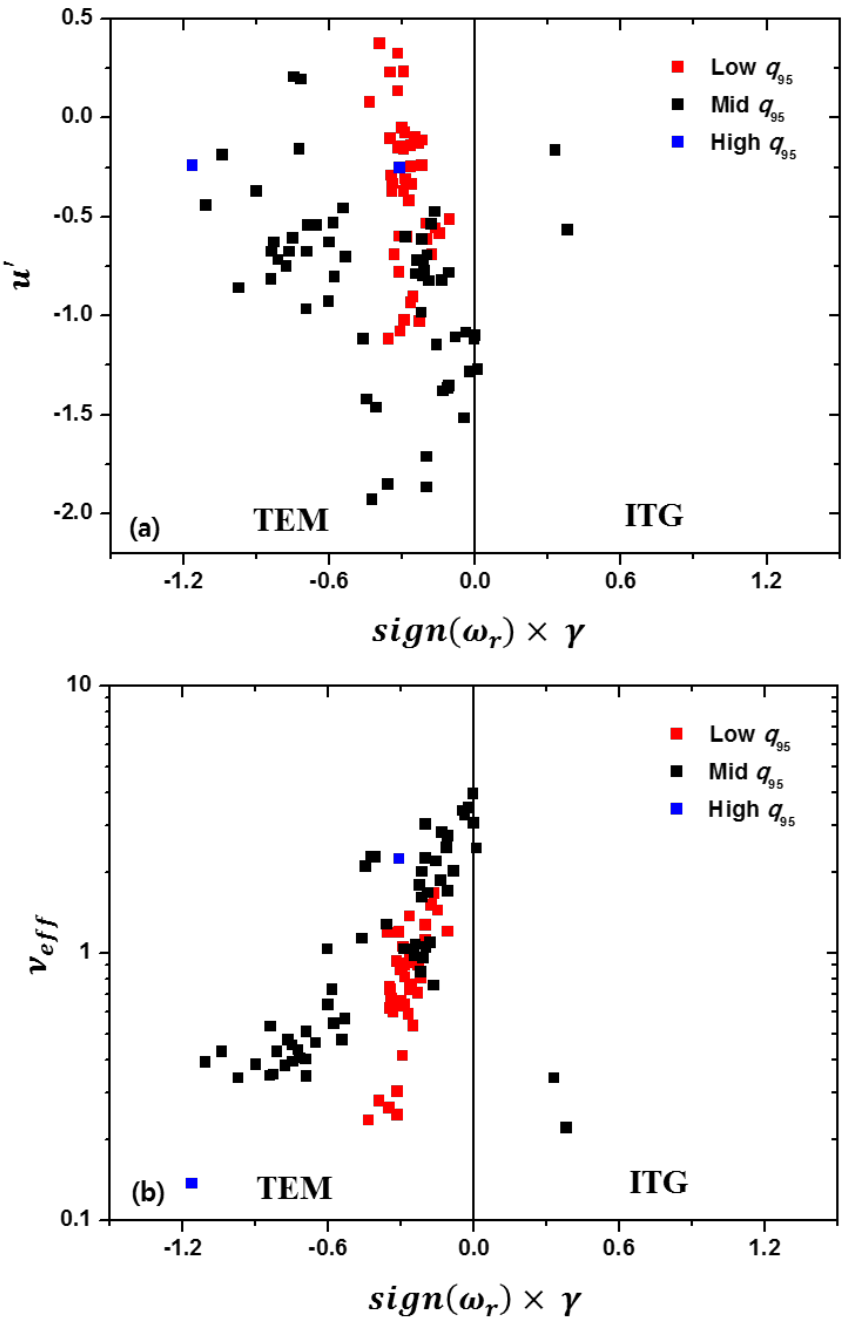

Figure 4.3 (a) u' and (b) ν_{eff} versus the linear growth rate (γ) multiplied by the sign of the real frequency (ω_r) of the dominant turbulent mode calculated with GKW using the KSTAR database with $k_y\rho_i = 0.3$ at $\rho = 0.5$.

The local nonlinear GKW was conducted to calculate the actual momentum fluxes during the change of u' with the increase of the density and the collisionality. Figure 4.4 (a) shows the turbulent heat (Q_e and Q_i), particle (Γ), and momentum fluxes (Π) that were normalized to the fluxes at the reference point of the lowest collisionality. Here, the collisionality is scanned consistently with T_e/T_i from 3 to 1 ($\nu \propto 1/(T_e/T_i)^2$) with a constant T_i and the fixed $R/L_{n_e} = 6$, $R/L_{T_i} = 6$, and $R/L_{T_e} = 10$, which are representative values at $\rho = 0.5$ during the change of u' as described in chapter 3.3 and the fixed $q = 1.5$ and $s = 1.0$. The momentum flux was calculated with a finite u', which captures the diffusive momentum flux only ($\Pi \sim \chi_\phi$). It is clearly observed that all of the turbulent fluxes rapidly decrease as the collisionality increases and it goes to nonlinearly stable conditions. Note that the plasma in this analysis is always TEM dominant, and the maximum linear growth rate of $0.1 \leq k_y\rho_i \leq 1$ decreases as the collisionality increases as shown in Figure 4.4 (b); this is in agreement with the linear growth rates for the experimental database in Figure 4.3. The comparison with the collisionless simulations indicates that the TEM stabilization arises from the decrease of T_e/T_i, as well as from the increase of the collisionality. Both weaken TEM, resulting in the decrease of all of the turbulent transport.

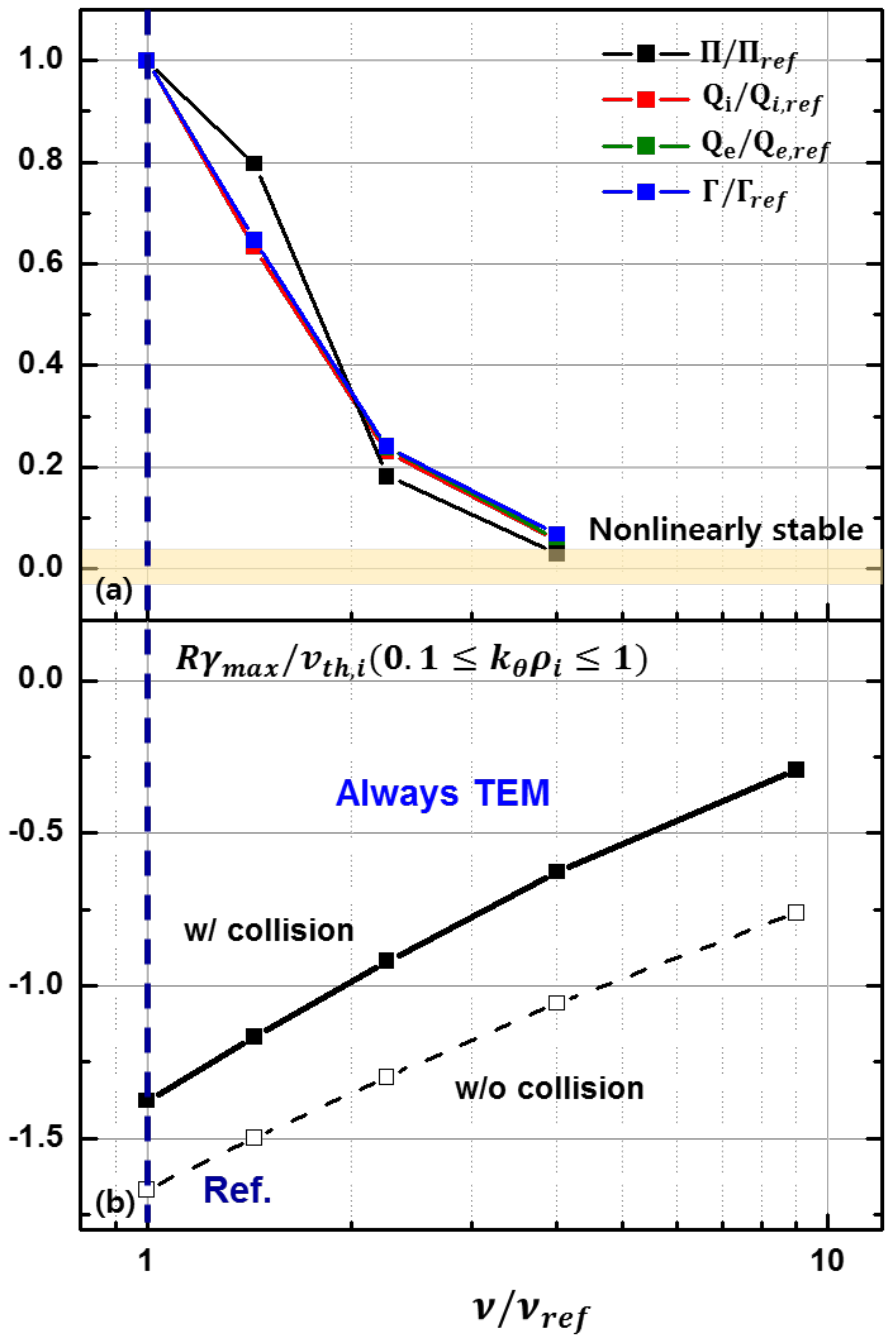

Figure 4.4 (a) Trends of the turbulent transport from the nonlinear gyrokinetic calculations and (b) the maximum linear growth rate (γ_{max}) of $0.1 \leq k_y\rho_i \leq 1$ from the multiplication of the real frequency (ω_r) sign with respect to the collisionality.

The result is partially consistent with the perturbative analysis as described in chapter 3.4. In both cases, the change of u' in the gradient region seems to be dominated by the reduction of the momentum diffusivity with the increase of the collisionality.

4.2.2. Non-Maxwell distribution model

Another mechanism was introduced to explain the rotation reversal in MAST [28]. It is the neoclassical equilibrium effect due to the deviation of the equilibrium distribution function from a Maxwellian [49] that is significantly dependent on the collisionality. To evaluate whether the mechanism would be dominant for the change of u' in KSTAR or not, a simplified approach based on equations (3) and (4) in Ref. 28 was applied for the KSTAR database. Here, the assumptions of $\widetilde{\Pi}_0 = 0.3$, $\widetilde{\Pi}_\infty = 1$, and $\nu_c = 1.7$ from Ref. 28 are followed, and the Prandtl number ($Pr \equiv \chi_\phi/\chi_i$) is assumed to be unity.

$$u' \approx -\left(\frac{\partial \rho}{\partial r}\right)\frac{1}{2P_r}\left(\frac{R}{L_{T_i}}\right)^2\left(\frac{\rho_i}{r}\right)q\widetilde{\Pi}(\nu_*) \qquad (4.2)$$

$$\widetilde{\Pi}(\nu_*) = \frac{\widetilde{\Pi}_0(\nu_*/\nu_c - 1)}{1+(\nu_*/\nu_c)(\widetilde{\Pi}_0/\widetilde{\Pi}_\infty)} \qquad (4.3)$$

Figure 4.5 shows the simple prediction of u' from the neoclassical equilibrium effect and the measured u' at $\rho = 0.5$ in the KSTAR

database. Although the residual stress from the neoclassical equilibrium effect in this calculation does not appear to be negligible in KSTAR, it is far less than the magnitude of the measured u'. Furthermore, it looks distinctly different from the measured u'. The predicted u' from the neoclassical equilibrium effect is always positive whereas the measured u' is negative for most of the datasets. In addition, the predicted u' from the neoclassical equilibrium effect does not show any clear dependence on ν_{eff}. This finding is because the normalized collisionality ($\nu_* \equiv qR\nu_{ii}/(v_{ti}\epsilon^{3/2})$) is approximately from 0.1 to 1.0 at $\rho = 0.5$ in the KSTAR database, which is far less than the assumed ν_c. If ν_c can be reduced to approximately 0.1, only then could this conclusion be changed. In recent, GKW calculations coupled with NEO [75] performed on the ASDEX Upgrade data showed that the predicted u' values were significantly smaller than the measured values and didn't show a clear dependence on ν_{eff} [76]. This approach is expected to help clarify the interpretation of the simplified approach above.

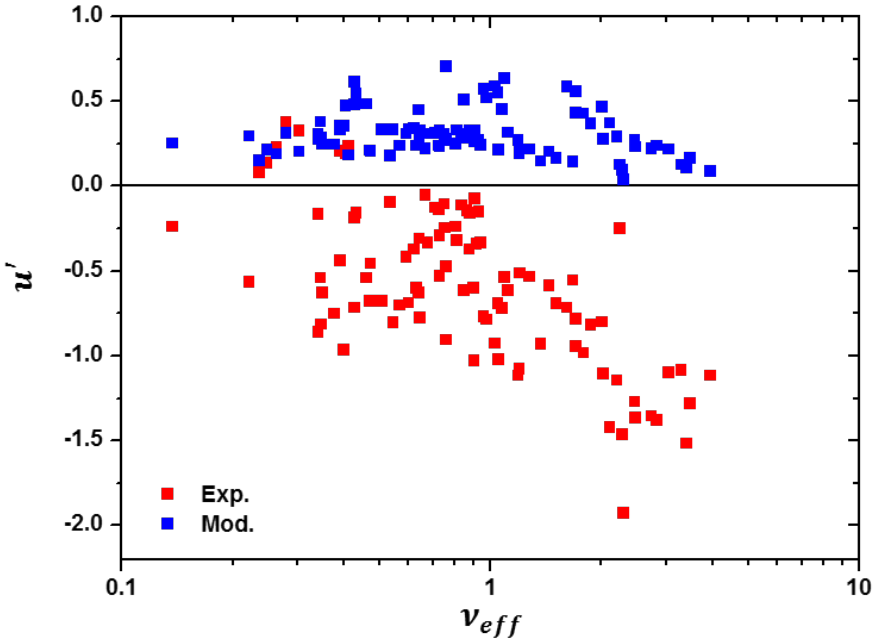

Figure 4.5 Simple prediction of u' from the neoclassical equilibrium effect and the measured u' versus ν_{eff} at $\rho = 0.5$, represented as blue and red squares, respectively, in the KSTAR database.

4.2.3. Intensity gradient model

The mode coupling due to the turbulence intensity gradient is one of possible mechanisms for the intrinsic rotation generation. It can break $k_{\parallel}$ symmetry and generate the intrinsic rotation. The intensity gradient can be measured in experiments so that its contributions can be separately estimated in principle. To investigate its contributions on the intrinsic rotation in KSTAR Ohmic plasmas, a simplified formula from Ref. 46 was used and its possibility was evaluated. For

the strong overlap case among modes, u' associated with the intensity gradient can be expressed as follows;

$$u' \cong -\frac{\hat{s}}{q}\frac{\langle x^2 \rangle}{\rho_i^2}\frac{\rho_i}{R}\frac{R}{\epsilon}\frac{\partial \epsilon}{\partial r} \qquad (4.4)$$

Since the intensity (ϵ) information does not exist for most datasets in KSTAR, the contributions from the intensity gradient was simply estimated rather than the quantitative analysis. In KSTAR Ohmic plasmas, $\frac{\hat{s}}{q} \sim 1$, $\frac{\rho_i}{R} \sim \frac{1}{100}$, $\frac{\langle x^2 \rangle}{\rho_i^2} \sim 1$ and $\frac{R}{\epsilon}\frac{\partial \epsilon}{\partial r} \sim \frac{1}{\sqrt{\rho_i a}} \sim 1-10$ are expected. It implies the contributions from the intensity gradient is much less than the measured u' in the gradient region. In actual, the normalized intensity gradient ($\frac{R}{\epsilon}\frac{\partial \epsilon}{\partial r}$) could be estimated from the fluctuation amplitude which can be directly measured in experiments. Figure 4.6 shows the normalized fluctuation amplitude of the electron temperature measured by using the ECE imaging (ECEI) diagnostic in KSTAR [77] and its gradient length for the discharge #12935 in Figure 3.2 (one of few discharges which have ECEI). The normalized fluctuation amplitude of the electron temperature does not change much during the density ramp-up. Here, the intensity gradient could be expressed as $\frac{R}{\epsilon}\frac{\partial \epsilon}{\partial r} \sim \frac{R}{L_{\delta T_e}}$ and it represents that the magnitude of $\frac{R}{\epsilon}\frac{\partial \epsilon}{\partial r}$ is not much different from above expectation.

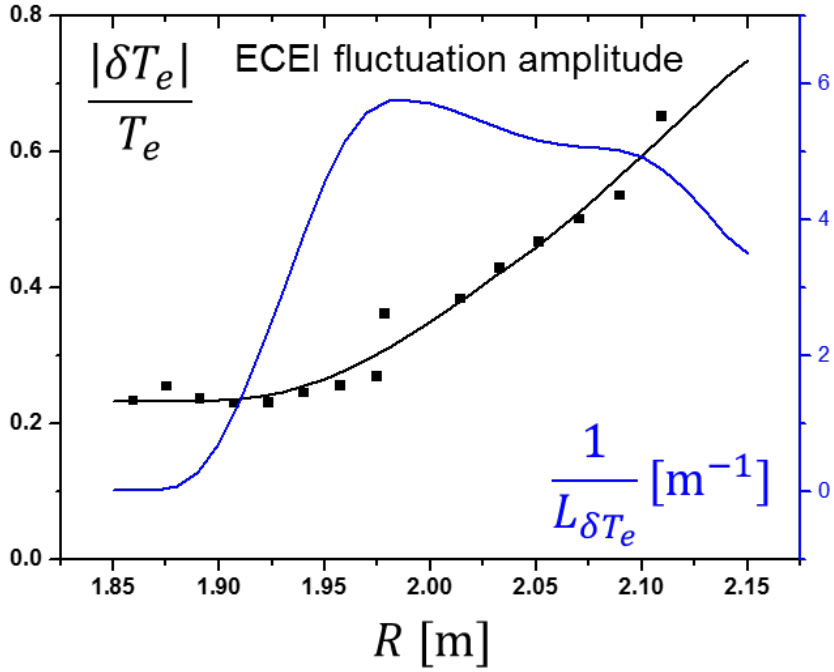

Figure 4.6 Fluctuation amplitude of the electron temperature measured by using ECEI and its gradient length for the discharge #12935 in KSTAR (see Figure 3.2).

4.2.4. Finite ballooning tilting model

In ASDEX Upgrade, an intrinsic rotation generation mechanism has been investigated with a finite ballooning tilting angle (θ_0) in linear gyrokinetic simulations [38]. The experimental observations from ASDEX Upgrade, in terms of both the magnitude of the normalized rotation gradient and its dependence on R/L_n, were well reproduced [38]. In this study, the mechanism was investigated using the KSTAR database. To calculate the magnitude of the normalized rotation

gradient from the mechanism, linear GKW simulations were conducted with the real plasma geometry, the measured kinetic profiles and $k_y\rho_i = 0.3$ with the assumptions of electrostatic, kinetic electron, and collisional plasma. The pinch term [78, 79] was not considered in this calculation since its contribution on u' was usually much less than 0.5. A unique θ_0 was used for all of the datasets. Figure 4.7 (a) shows the predicted u' and the measured u' versus ν_{eff} at $\rho = 0.5$ in the datasets presented in Figures 4.1, 4.3 and 4.5. Some of the datasets with a linear growth rate less that is than 0.1 ($R\gamma/v_{th,i}$) were filtered out since the calculated fluxes are unreasonable for the nearly stable plasmas (a number of unreasonable positive value results, which are unfiltered by the criteria but have a low linear growth rate, still remain). Interestingly, the predicted u' could represent the similar magnitude order in the experiment, and it is also quantitatively dependent on ν_{eff} as in the experiment. Here, $\theta_0 = -1.0$ was used in this analysis, which is arbitrary but comparable to that from global simulations [48]. Considering that R/L_n is fairly scattered in the KSTAR database, the ν_{eff} dependence of the predicted u', unlike the result of ASDEX Upgrade, would not result from the R/L_n dependence. It is also notable that the best matching value of θ_0 for the KSTAR database is much larger than the value of -0.25 for the TEM datasets that was

used in ASDEX Upgrade, implying that there could be different processes contributing to the ballooning tilting angle in KSTAR and ASDEX Upgrade. In addition to the features of the gradient region, the existence of the anchor point is an important implications for the validation of the intrinsic rotation mechanism. The above analysis was applied to the typical anchor point for the mid and low q_{95} datasets, $\rho = 0.7$, to investigate whether the mechanism can also capture the anchor point characteristics. In Figure 4.7 (b), the predicted u' and the measured u' versus ν_{eff} at $\rho = 0.7$ were plotted for the given database. The measured u' comprises nearly zero values regardless of ν_{eff}, which shows the anchor point characteristics. Interestingly, the predicted u' at $\rho = 0.7$ shows relatively lower values than the predicted u' at $\rho = 0.5$ even with the same $\theta_0 = -1.0$. Additionally, it does not represent the clear dependence on ν_{eff}; these characteristics are in line with the experiments. It is surprising that the simplified calculation for the residual stress with the finite ballooning tilting shows quite similar characteristics with both of the experimental observations of the gradient region and the anchor point.

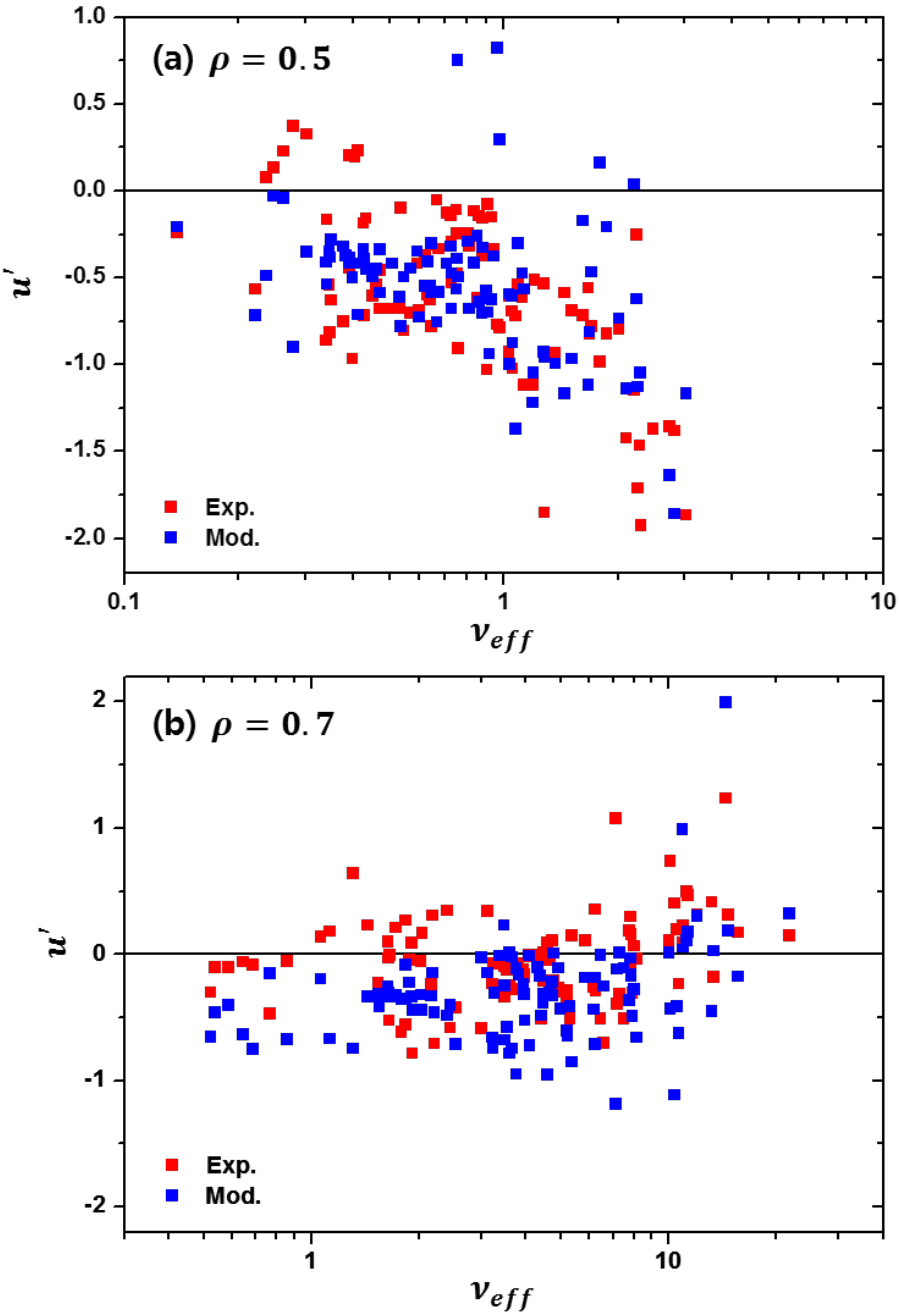

Figure 4.7 Predicted u' from the profile shearing effect and the measured u' versus ν_{eff} at (a) $\rho = 0.5$ and (b) $\rho = 0.7$ in the KSTAR database where $\theta_0 = -1.0$ is assumed.

The manner in which the residual stress with the finite ballooning tilting can reproduce the different collisionality dependences at the gradient region and the anchor point is of a significant interest. To investigate the reason, further calculations were carried out. In the calculations, several sets of the magnetic shear (s) and the q value were evaluated since both are considered as key parameters in the division of the gradient region and the anchor point in the KSTAR experiments. Here, the collisionality is scanned consistently with T_e/T_i from 3 to 1 ($\nu \propto 1/(T_e/T_i)^2$) with a constant T_i and the fixed $R/L_{n_e} = 6$, $R/L_{T_i} = 6$, and $R/L_{T_e} = 10$, which are representative values at $\rho = 0.5$ during the change of u' in KSTAR. For simplicity, circular geometry, electrostatic, kinetic electrons, collisional plasmas, and $k_y\rho_i = 0.3$ were assumed. Figure 4.8 (a) shows the predicted u' versus ν with different magnetic shears and q values in the linear GKW calculations. Interestingly, the predicted u' with $s = 0.5$ increases to a negative value as the collisionality increases, which is similar to the characteristics of u' in the gradient region. However, for $s = 1.5$ cases, the predicted u' shows a monotonic decrease to the zero value as the collisionality increases. The q value used in the calculations does not affect the trend, but the magnitude of the predicted u' is smaller for the large q values regardless of the magnetic shear. These findings seems to explain the analysis results

in the above comparison between the predicted one and the measured one; furthermore, it is consistent with the experimental observations, where the gradient region is only observed with the small q value and the weak magnetic shear.

Now, the question regarding the way that the residual stress changes to increase u' with the increase of the collisionality or the decrease of T_e/T_i in the gradient region can be considered. The momentum diffusivity and the residual stress would be strongly coupled with the turbulence amplitude since it is usually considered that the turbulent transport would be dominant for the momentum flux; therefore, with the given symmetry breaking, the variation of the momentum diffusivity and the residual stress could be approximately estimated from the linear growth rate. In Figure 4.8 (b), it is clearly observed that the linear growth rate of the dominant mode decreases with the increase of the collisionality, or the decrease of T_e/T_i, regardless of the q value and the magnetic shear. This means that both the momentum diffusivity and the residual stress would decrease with the increase of the collisionality, or the decrease of T_e/T_i. This is consistent with the experimental observation in chapter 3.4 and the nonlinear GKW calculations in chapter 4.2.1.

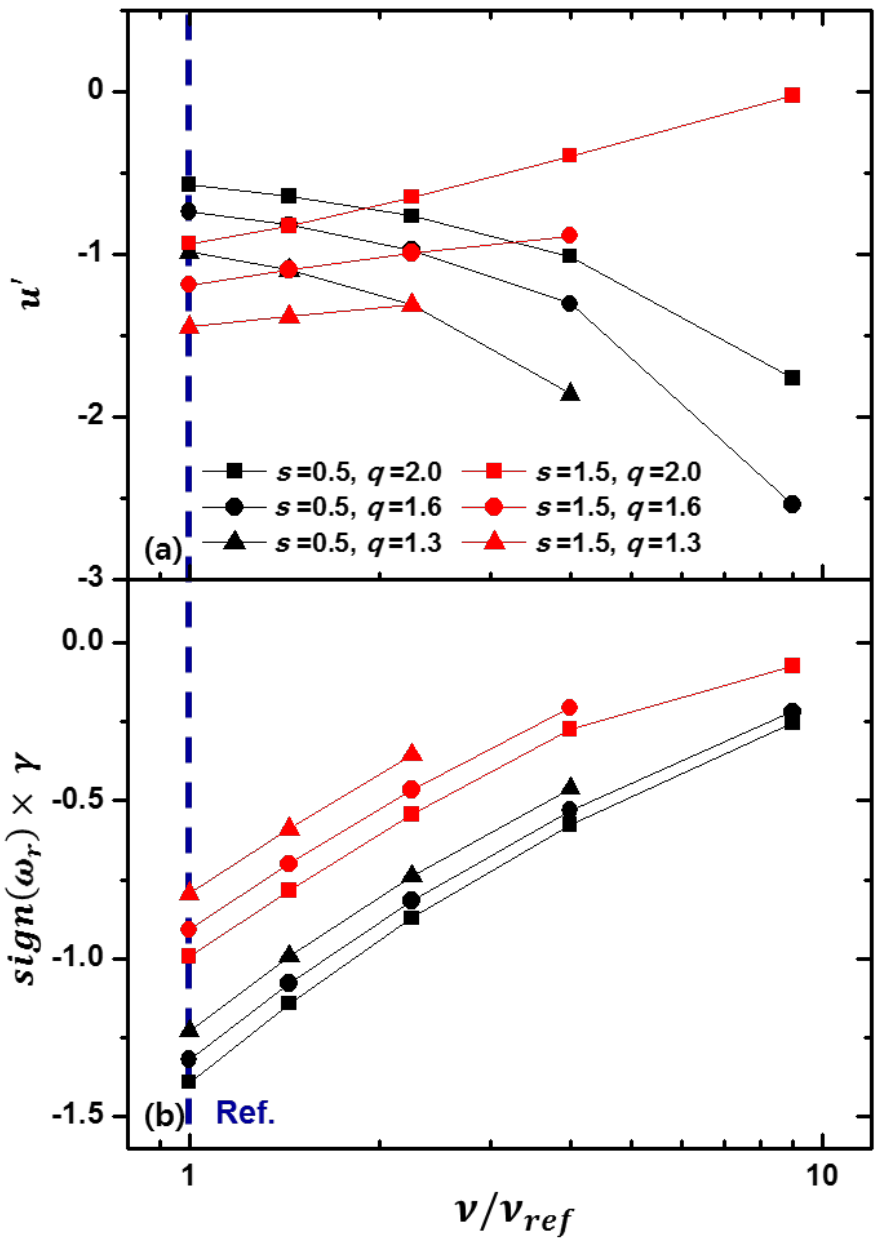

Figure 4.8 (a) Predicted u' from the finite ballooning tilting, (b) linear growth rate (γ) multiplied by the sign of the real frequency (ω_r) of the dominant mode with different $\hat{s}$ and q values versus the collisionality. The collisionality is scanned consistently with T_e/T_i from 3 to 1.

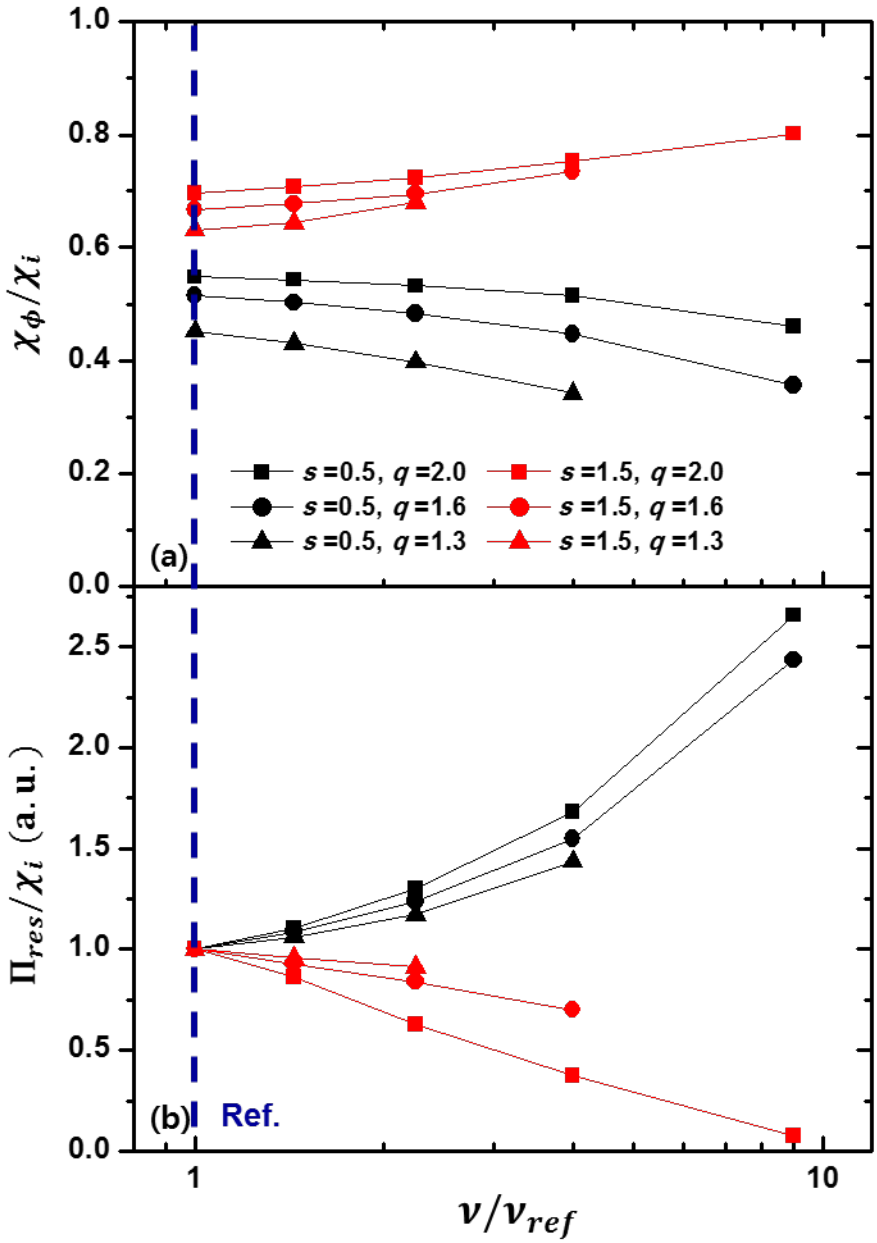

Figure 4.9 (a) χ_ϕ/χ_i, and (b) Π_{res}/χ_i with different $\hat{s}$ and q values versus the collisionality. The collisionality is scanned consistently with T_e/T_i from 3 to 1.

At this time, it should be noted that the relative dependence of Π_{res} and χ_ϕ on the collisionality. As shown in Figure 4.9 (b), Π_{res}/χ_i increases as the collisionality increases for $s = 0.5$ cases, but decreases for $s = 1.5$. On the other hand, χ_ϕ/χ_i does not change much with the increase of the collisionality regardless of the q value and the magnetic shear as shown in Figure 4.9 (a). It implies that the reduction of the momentum diffusivity would be comparatively larger than the reduction of the residual stress, which could result in the increase of u' in the gradient region, where the magnetic shear is weak and the q value is small. Meanwhile, at the anchor point where the magnetic shear is strong and the q value is large, the profile shearing effect is limited so that a nearly zero u' and the absence of a dependence on the collisionality are observed. Although the finite ballooning tilting model with arbitrary and finite θ_0 is used in the calculations, it is interesting that most of the intrinsic rotation characteristics observed in KSTAR Ohmic plasmas as described in chapter 3 can be explained by the model prediction.

Chapter 5. Application to KSTAR Ohmic Plasmas with Integrated Modelling

5.1. Integrated modelling for intrinsic rotation prediction

By comparing and analyzing the characteristics of the intrinsic rotation observed in the experiment and some theoretical models, it was confirmed that there is a high possibility model which is the finite ballooning tilting model. In this chapter, we describe how to calculate the intrinsic rotation profiles through the integrated modeling that integrates the model calculation code with the transport code. This integrated modeling is based on the KSTAR experimental data, and other plasma properties such as T_{i}, T_{e}, and n_{e} except the plasma rotation are fixed at the measured values. Here, a single loop calculation is used for the integrated modelling and the intrinsic rotation prediction in KSTAR Ohmic plasmas. This approach is valid when the plasma properties except the plasma rotation are fixed and the plasma rotation does not effect on the momentum transport component calculations. Figure 5.1 shows a schematic diagram of this system. ASTRA was introduced as a transport code to solve the plasma rotation, and the integrated modelling system was built by combining the GKW code for the model calculation proposed in

chapter 4 with the ASTRA code. First, the various plasma properties in the experiment are reflected in ASTRA. Second, the information used in GKW calculations is calculated from the ASTRA code and transferred to the GKW code. Then, the components constituting the momentum transport are calculated and transferred to the ASTRA code. In the calculations where no external torque is injected, the intrinsic rotation profile is determined solely by V_p/χ_ϕ and $\Pi_{\mathrm{res}}/\chi_\phi$, and χ_ϕ does not effect on the intrinsic rotation profiles (but it effects on the time-evolution of the plasma rotation when there is some perturbations to the plasma rotation). Here, the GKW calculation for a radial point consumes about 10-100 CPU hours, but since only a single loop is considered as mentioned above, the total calculation time would be acceptable.

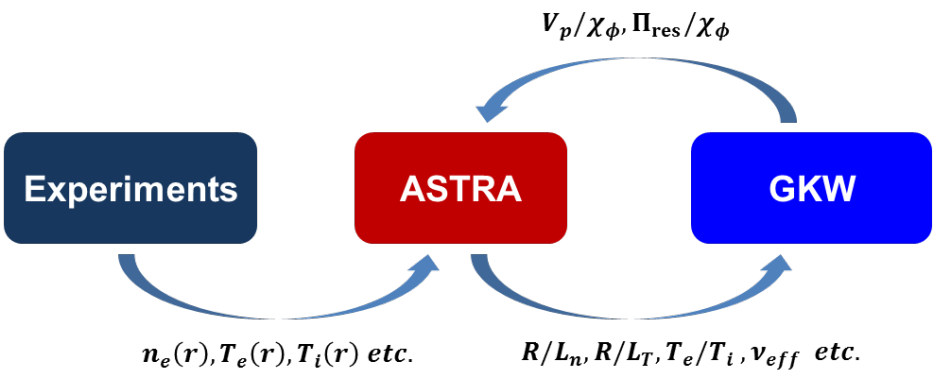

Figure 5.1 Schematic diagram of the integrated modelling system for the intrinsic rotation prediction in KSTAR Ohmic plasmas using ASTRA and GKW.

5.2. Prediction of intrinsic rotation in KSTAR Ohmic plasmas

Intrinsic rotation profiles in KSTAR Ohmic plasma was predicted by applying the integrated modeling system developed in chapter 5.1. As a test case, the intrinsic rotation profile evolution according to the plasma density in a single discharge is selected. Here, the intrinsic rotation profiles at the low u' case and the high u' case were predicted and compared with the measured intrinsic rotation profiles. In this calculation, the finite ballooning tilting angle (θ_0) is assumed to be -1.0 for the all radius to reflect the result of chapter 4, and the calculation boundary is fixed at $\rho = 0.9$. In Figures 5.2 (a) and 5.2 (b), the predicted intrinsic rotation (red line) at the core is similar to the experimental values for both cases. Furthermore, the change of u' and the anchor point characteristic seem to be well captured. Nevertheless, it is observed that u' in the gradient region is under-estimated than the measured one. In order to have a similar u' in the gradient region, θ_0 should be twice larger than the previous one for the low u' case and four times larger for the high u' case. In this integrated modelling system, the sawtooth activity was not considered so that the required θ_0 might be reduced when we consider the momentum redistribution caused by the sawtooth activity. It is interesting that this system predicts the characteristics

of the plasma density dependence of u' in the gradient region and the anchor point, although there is a limit to precisely predict the intrinsic rotation profile in experiments. When the more accurate plasma equilibrium and the estimation for θ_0 are prepared, it is expected that this system will show more precise results.

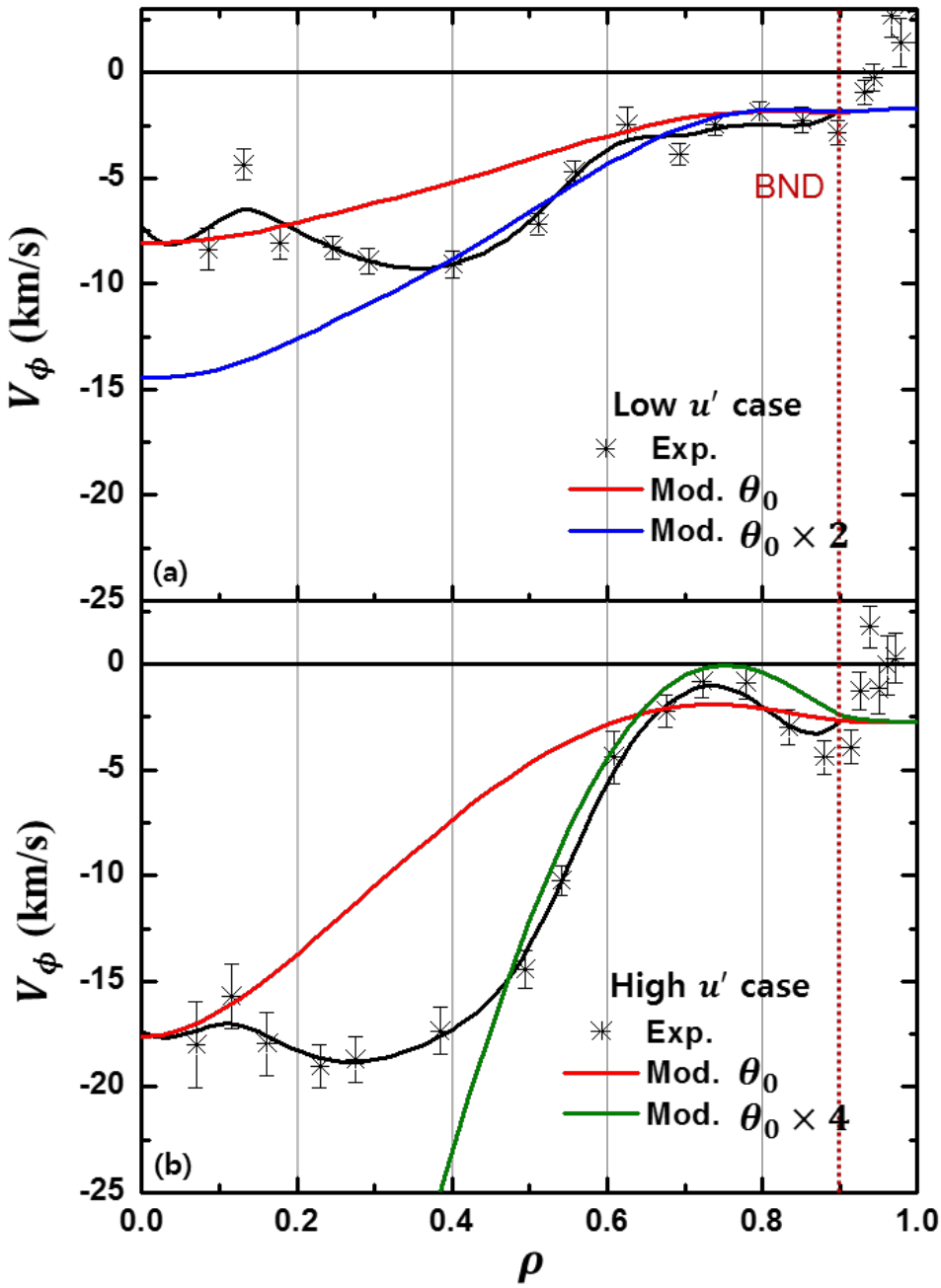

Figure 5.2 Examples of the predicted intrinsic rotation profiles with the above integrated modelling system and the intrinsic rotation profiles in experiments: (a) the low u' case and (b) the high u' case.

Chapter 6. Conclusions and Future works

For the intrinsic rotation study in KSTAR Ohmic plasmas, a new approach of the experiment was designed to measure intrinsic rotation profiles where the discharge is conducted with the beam blip techniques under the optimal operating conditions of the beam. For the several years of the KSTAR experimental campaigns, statistically sufficient intrinsic rotation profiles under various operating and plasma conditions were accumulated and its characteristics were investigated from the profile-based analysis (far different from the conventional $V_\phi(0)$ based analysis). The typical feature of the intrinsic rotation profiles were investigated where two main features of the intrinsic rotation are the normalized toroidal rotation gradient (u') change in the gradient region with the increase of the plasma density and the collisionality (represents the conventional rotation reversal phenomenon in KSTAR) and the existence of an anchor point. It was found that the locations of the gradient region and the anchor point is closely related to q_{95} and the strong dependence of u' on ν_{eff} is clearly observed in the gradient region, whereas the dependence on R/L_{T_i}, R/L_{T_e}, and R/L_{n_e} is unclear. Further analysis implies that the increase of u' in the gradient region with the increase of the plasma density and the collisionality would occur

when the reduction of the momentum diffusivity is comparatively larger than the reduction of the residual stress. It is supported by the perturbative analysis of the experiments and the linear/nonlinear gyrokinetic simulations. The absence of the sign change of u' even at a much lower collisionality by additional electron cyclotron heating (ECH) brings further experimental support to this interpretation. The experimental observations were compared with the theoretical models. It seems that the residual stress associated with a finite ballooning tilting well reproduces the experimental observations of both the gradient region and the anchor point; the difference was explained by the magnetic shear and the q value in the regions. The integrated modelling which combines ASTRA and GKW was applied to predict the intrinsic rotation profiles in KSTAR Ohmic plasmas with the selected theoretical model. Although the predicted intrinsic rotation profiles do not exactly match with the measured intrinsic rotation profiles in experiments, the change of u' with the increase of the plasma density and the collisionality and the existence of the anchor point region seems to be well captured by the integrated modelling.

This study shows the limitation of the $V_\phi(0)$ based analysis, which has been usually conducted for the intrinsic rotation study in various tokamaks, and represents the importance of the profile–

based analysis. As a result of this study, the experimental in KSTAR Ohmic plasmas and several ECH plasmas were characterized, and a possible mechanism of the intrinsic rotation generation was suggested through a comparison of theoretical models with the collected large database in KSTAR until the 2016 experiment campaign. This study contributed to the understanding of the intrinsic rotation characteristics and its generation mechanism in KSTAR Ohmic plasmas. This study could be extended further by investigating another operating regime in KSTAR such as Ohmic H-mode and operations with auxiliary heating. For the possible mechanism of the intrinsic rotation generation, the finite ballooning tilting model could be more precisely investigated through a global nonlinear simulation.

Bibliography

[1] J. D. Lawson, “Some Criteria for a Power Producing Thermonuclear Reactor”, Proceedings of the Physical Society, 70, 6 (1957)

[2] Eurofusion organization, “Tokamak Principle”: https://www.euro-fusion.org/2011/09/tokamak-principle-2/?view=gallery-11

[3] A. Bondeson and D. J. Ward, “Stabilization of External Modes in Tokamaks by Resistive Walls and Plasma Rotation”, Physical Review Letters, 72, 2709 (1994)

[4] Y. Liu, A. Nondeson, Y. Gribov and A. Polevoi, “Stabilization of resistive wall modes in ITER by active feedback and toroidal rotation”, Nuclear Fusion, 44 232 (2004)

[5] M. Takechi, G. Matsunaga, N. Aiba, T. Fujita, T. Ozeki, Y. Koide, Y. Sakamoto, G. Kurita, A. Isayama, Y. Kamada, and the JT-60 team, “Identification of a Low Plasma-Rotation Threshold for Stabilization of the Resistive-Wall Mode”, Physical Review Letters, 98, 055002 (2007)

[6] L. J. Zheng, M. T. Kotshenreuther and J. W. Van Dam, “Kinetic analysis of the resistive wall modes in the ITER advanced tokamak scenario”, Nuclear Fusion, 49, 075021 (2009)

[7] L. J. Zheng, M. T. Kotschenreuther and J. W. Van Dam, “Rotational stabilization of resistive wall modes in ITER advanced tokamak scenarios”, Physics of Plasmas, 17 056104 (2010)

[8] J. W. Berkery, S. A. Sabbagh, R. Betti, B. Hu, R. E. Bell, S. P. Gerhardt, J. Manickam, and K. Tritz, “Resistive Wall Mode Instability at Intermediate Plasma Rotation”, Physics Review Letters, 104, 035003 (2010)

[9] K. C. Shaing and E. C. Crume Jr, “Bifurcation Theory of Poloidal Rotation in Tokamaks: A Model for the L−H transition”, Physical Review Letters, 63, 21 (1989)

[10] R. J. Groebner, K. H. Burrell, and R. P. Seraydarian, “Role of Edge Electric Field and Poloidal Rotation in the L−H Transition”, Physical Review Letters, 64, 3015 (1990)

[11] K. Ida and S. Hidekuma, “Edge Electric−Field Profiles of H−Mode Plasmas in the JFT−2M Tokamak”, Physical Review Letters, 65, 1364 (1990)

[12] H. Matsumoto, K. H. Burrell, T. N. Carlstrom, E. J. Doyle, P. Gohil, R. J. Groebner, T. Lehecka, N. C. Luhmann Jr, M. A. Mahdavi, T. H. Osborne, W. A. Peebles, and R. Philipona, “Suppression of the edge turbulence at the L−H transition in DIII−D”, Plasma Physics and Controlled Fusion, 34, 615 (1992)

[13] N. Aiba, S. Tokuda, M. Furukawa, N. Oynama and T. Ozeki, "Effects of a sheared toroidal rotation on the stability boundary of the MHD modes in the tokamak edge pedestal", Nuclear Fusion, 49, 065015 (2009)

[14] R. J. Buttery, R. J. La Haye, P. Gohil, G. L. Jackson, H. Reimerdes, and E. J. Straitm "The influence of rotation on the β_N threshold for the 2/1 neoclassical tearing mode in DIII-D", Physics of Plasmas, 15, 056115 (2008)

[15] P. H. Diamond, C. J. McDervitt, O. D. Gurcan, T. S. Hahm, W. X. Wang, E. S. Yoon, I. Holod, Z. Lin, V. Naulin and R. Singh, "Physics of non-diffusive turbulent transport of momentum and the origins of spontaneous rotation in tokamaks", Nuclear Fusion, 49, 045002 (2009)

[16] F. D. Halpern, A. H. Kritz, G. Bateman, A. Y. Pankin, R. V. Budny, and D. C. McCune, "Predictive simulations of ITER including neutral beam driven toroidal rotation", Physics of Plasmas, 15, 062505 (2008)

[17] R. V. Budny, R. Andre, G. Bateman, F. Halpern, C. E. Kessel, A. Kritz and D. McCune, "Predictions of H-mode performance in ITER", Nuclear Fusion, 48, 075005 (2008)

[18] L.-G. Eriksson, E. Righi and K.-D. Zastrow, "Toroidal rotation in ICRF-heated H-modes on JET", Plasma Physics and

Controlled Fusion, 39, 27 (1997)

[19] J. E. Rice, M. Greenwald, I. H. Hutchinson, E. S. Marmar, Y. Takase, S. M. Wolfe, F. Bombarda, "Observation of Central Toroidal Rotation in ICRF Heated Alcator C-Mod Plasmas", Nuclear Fusion, 38, 75 (1998)

[20] G. T. Hoang, P. Monier-Garbet, T. Aniel, C. Bourdelle, R. V. Budny, F. Clairet, L.-G. Eriksson, X. Garbet, C. Grisolia, P. Platz, J. C. Vallet, "An H minority heating regime in Tore Supra showing improved L mode confinement", Nuclear Fusion, 40, 913 (2000)

[21] J. S. deGrassie, K. H. Burrel, L. R. Baylor, W. Houlberg, J. Lohr, "Toroidal rotation in DIII-D in electron cyclotron heating and Ohmic H-mode discharges", Physics of Plasmas, 11, 4323 (2004)

[22] J. E. Rice, A. Ince-Cushman, J. S. deGrassie, L.-G. Eriksson, Y. Sakamoto, A. Scarabosio, A. Bortolon, K. H. Burrell, B. P. Duval, C. Fenzi-Bonizec, M. J. Greenwald, R. J. Groebner, G. T. Hoang, Y. Koide, E. S. Marmar, A. Pochelon and Y. Podpaly, "Inter-machine comparison of intrinsic toroidal rotation in tokamaks", Nuclear Fusion, 47, 1618 (2007)

[23] M. F. F. Nave, L.-G. Eriksson, C. Giroud, T. J. Johnson, K. Kirov, M.-L. Mayoral, J.-M. Noterdaeme, J. Ongena, G. Saibene, R.

Sartori, F. Rimini, T. Tala, P. deVries, K.-D. Zastrow, "JET intrinsic rotation studies in plasmas with a high normalized beta and varying toroidal field ripple", Plasma Physics and Controlled Fusion, 54, 074006 (2012)

[24] J. S. deGrassie, W. M. Solomon, J. E. Rice, and J.-M. Noterdaeme, "Dimensionless size scaling of intrinsic rotation in DIII-D", Physics of Plasmas, 23, 082501 (2016)

[25] A. Bortolon, B. P. Duval, A. Pochelon and A. Scarabosio, "Observation of Spontaneous Toroidal Rotation Inversion in Ohmically Heated Tokamak Plasmas", Physics Review Letters, 97, 235003 (2006)

[26] J. E. Rice, A. C. Ince-Cushman, M. L. Reinke, Y. Podpaly, M. J. Greenwald, B. LaBombard and E. S. Marmar, "Spontaneous core toroidal rotation in Alcator C-Mod L-mode, H-mode, and ITB plasmas, Plasma Physics and Controlled Fusion, 50, 124042 (2008)

[27] C. Angioni, R. M. McDermott, F. J. Casson, E. Fable, A. Bottino, R. Dux, R. Fischer, Y. Podoba, T. Putterich, F. Ryter, E. Viezzer, and ASDEX Upgrade Team, "Intrinsic Toroidal Rotation, Density Peaking, and Turbulence Regimes in the Core of Tokamak Plasmas", Physical Review Letters, 107, 215003 (2011)

[28] J. C. Hillesheim, F. I. Parra, M. Marnes, N. A. Crocker, H. Meyer, W. A. Peebles, R. Scannell, A. Thornton and the MAST Team, “Dependence of intrinsic rotation reversals on collisionality in MAST”, Nuclear Fusion, 55, 032003 (2015)

[29] D. H. Na, Yong-Su Na, S. G. Lee, C. Angioni, S. M. Yang, H.-S. Kim, T. S. Hahm, W. H. Ko, H. Jhang, W. J. Lee and KSTAR Team, “Observation of the intrinsic rotation in KSTAR Ohmic L-mode plasmas”, Nuclear Fusion, 56, 036011 (2016)

[30] B. P. Duval, A. Bortolon, A. Karpushov, R. A. Pitts, A. Pochelon, A. Scarabosio and the TCV Team, “Bulk plasma rotation in the TCV tokamak in the absence of external momentum input”, Plasma Physics and Controlled Fusion, 49, B195 (2007)

[31] B. P. Duval, A. Bortolon, A. Karpushov, R. A. Pitts, A. Pochelon, O. Sauter, A. Scarabosio, G. Turri, and the TCV Team, “Spontaneous L-mode plasma rotation scaling in the TCV tokamak, Physics of Plasmas, 15, 056113 (2008)

[32] J. E. Rice, B. P. Duval, M. L. Reinke, Y. A. Podpaly, A. Bortolon, R. M. Churchill, I. Cziegler, P. H. Diamond, A. Dominguez, P. C. Ennever, “Observation of core toroidal rotation reversals in Alcator C-Mode ohmic L-mode plasmas”, Nuclear Fusion, 51, 083005 (2011)

[33] J. E. Rice, I. Cziegler, P. H. Diamond, B. P. Duval, Y. A. Podpaly,

M. L. Reinke, P. C. Ennever, M. J. Greenwald, J. W. Hughes, Y. Ma, E. S. Marmar, M. Porkolab, N. Tsujii, and S. M. Wolfe, "Rotation Reversal Bifurcation and Energy Confinement Saturation in Tokamak Ohmic L-Mode Plasmas", Physics Review Letters, 107, 265001 (2011)

[34] J. E. Rice, M. J. Greenwald, Y. A. Podpaly, M. L. Reinke, P. H. Diamond, J. W. Hughes, N. T. Howard, Y. Ma, I. Cziegler, B. P. Duval, P. C. Ennever, D. Ernst, C. L. Fiore, C. Gao, J. H. Irby, E. S. Marmar, M. Porkolab, N. Tsujii, and S. M. Wolfe, "Ohmic energy confinement saturation and core toroidal rotation reversal in Alcator C-Mod plasmas", Physics of Plasmas, 19, 056106 (2012)

[35] J. E. Rice, C. Gao, M. L. Reinke, P. H. Diamond, N. T. Howard, H. J. Sun, I. Cziegler, A. E. Hubbard, Y. A. Podpaly, W. L. Rowan, J. L. Terry, M. A. Chilenski, L. Delgado-Aparicio, P. C. Ennever, D. Ernst, M. J. Greenwald, J. W. Hughes, Y. Ma, E. S. Marmar, M. Porkolab, A. E. White and S. M. Wolfe, "Non-local heat transport, rotation reversals and up/down impurity density asymmetries in Alcator C-Mod ohmic L-mode plasmas", Nuclear Fusion, 53, 033004 (2013)

[36] M. L. Reinke, J. E. Rice, I. H. Hutchinson, M. Greenwald, N. T. Howard, J. W. Hughes, J. Irby, Y. Podpaly, J. L. Terry and A.

White, “Non-neoclassical up/down asymmetry of impurity emission on Alcator C-Mod”, Nuclear Fusion, 53, 043006 (2013)

[37] C. Gao, J. E. Rice, H. J. Sun, M. L. Reinke, N. T. Howard, D. Mikkelson, A. E. Hubbard, M. A. Chilenski, J. R. Walk, J. W. Hughes, P. C. Ennever, M. Porkolab, A. E. White, C. Sung, L. Delgado-Aparicio, S.G. Baek, W. L. Rowan, M. W. Brookman, M. J. Greenwald, R. S. Granetz, S. W. Wolfe, E. S. Marmar and The Alcator C-Mod Team, “Non-local heat transport in Alcator C-Mod ohmic L-mode plasmas”, Nuclear Fusion, 54, 083025 (2014)

[38] R. M. McDermott, C. Angioni, G. D. Conway, R. Dux, E. Fable, R. Fisher, T. Putterich, F. Ryter, E. Viezzer and the ASDEX Upgrade Team, “Core intrinsic rotation behavior in ASDEX Upgrade ohmic L-mode plasmas”, Nuclear Fusion, 54, 043009 (2014)

[39] K. Ida and J. E. Rice, “Rotation and momentum transport in tokamaks and helical systems”, Nuclear Fusion, 54, 045001 (2014)

[40] J. E. Rice, “Experimental observations of driven and intrinsic rotation in tokamak plasmas”, Plasma Physics and Controlled Fusion, 58, 083001 (2016)

[41] Y. J. Shi, J. M. Kwon, P. H. Diamond, W. H. Ko, M. J. Choi, S. H.

Ko, S. H. Hahn, D. H. Na, J. E. Leem, J. A. Lee, S. M. Yang, K. D. Lee, M. Joung, J. H. Jeong, J. W. Yoo, W. C. Lee, J. H. Lee, Y. S. Bae, S. G. Lee, S. W. Yoon, K. Ida and Y.-S. Na, "Intrinsic rotation reversal, non-local transport, and turbulence transition in KSTAR L-mode plasmas", Nuclear Fusion, 57, 066040 (2017)

[42] O. D. Gurcan and P. H. Diamond, "Intrinsic rotation and electric field shear", Physics of Plasmas, 14, 042306 (2007)

[43] P. H. Diamond, C. J. McDevitt, O. D. Gurcan, T. S. Hahm, V. Naulin, "Transport of parallel momentum by collisionless drift wave turbulence", Physics of Plasmas, 15, 012303 (2008)

[44] Y. Camenen, A. G. Peeters, C. Angioni, F. J. Casson, W. A. Hornsby, A. P. Snodin, and D. Strintzi, "Transport of Parallel Momentum Induced by Current-Symmetry Breaking in Toroidal Plasmas", Physics Review Letters, 102, 125001 (2009)

[45] O. D. Gurcan, P. H. Diamond, C. J. McDevitt, and T. S. Hahm, "A simple model of intrinsic rotation in high confinement regime tokamak plasmas", Physics of Plasmas, 17, 032509 (2010)

[46] O. D. Gurcan, P. H. Diamond, P. Hennequin, C. J. McDevitt, X. Garbet, and C. Bourdelle, "Residual parallel Reynolds stress due to turbulence intensity gradient in tokamak plasmas", Physics of Plasmas, 17, 112309 (2010)

[47] R. E. Waltz, G. M. Staebler, and W. M. Solomon, “Gyrokinetic simulation of momentum transport with residual stress from diamagnetic level velocity shears”, Physics of Plasmas, 18, 042504 (2011)

[48] Y. Camenen, Y. Idomura, S. Jolliet, and A. G. Peeters, “Consequences of profile shearing on toroidal momentum transport”, Nuclear Fusion, 51, 073039 (2011)

[49] M. Barnes, F. I. Parra, J. P. Lee, E. A. Belli, M. F. F. Nave, and A. E. White, “Intrinsic Rotation Driven by Non-Maxwellian Equilibria in Tokamak Plasmas”, Physical Review Letters, 111, 055005 (2013)

[50] P. H. Diamond, Y. Kosuga, O. D. Gurcan, C. J. McDevitt, T. S. Hahm, N. Fedorczak, J. E. Rice, W. X. Wang, S. Ku, J. M. Kwon, G. Dif-Pradalier, J. Abiteboul, L. Wang, W. H. Ko, Y. J. Shi, K. Ida, W. Solomon, H. Jhang, S. S. Kim, S. Yi, S. H. Ko, Y. Sarazin, R. Singh and C. S. Chang, “An overview of intrinsic torque and momentum transport bifurcations in toroidal plasmas”, Nuclear Fusion, 53, 104019 (2013)

[51] S. G. Lee, J. G. Bak, U. W. Nam, M. K. Moon, Y. Shi, M. Bitter, and K. Hill, “The first experimental results from x-ray imaging crystal spectrometer for KSTAR”, Review of Scientific Instruments, 81, 10E506 (2010)

[52] W. H. Ko, H. H. Lee, D. C. Seo, M. Kwon, “Charge exchange spectroscopy system calibration for ion temperature measurement in KSTAR”, Review of Scientific Instruments, 81, 10E740 (2010)

[53] A. Scarabosio, A. Bortolon, B. P. Duval, A. Karpushov and A. Pochelon, “Toroidal plasma rotation in the TCV tokamak”, Plasma Physics and Controlled Fusion, 48, 663 (2006)

[54] J. Seol, S. G. Lee, B. H. Park, H. H. Lee, L. Terzolo, K. C. Shaing, K. I. You, G. S. Yun, C. C. Kim, K. D. Lee, W. H. Ko, J. G. Kwak, W. C. Kim, Y. K. Oh, J. Y. Kim, S. S. Kim, and K. Ida, “Effects of Electron-Cyclotron-Resonance-Heating-Induced Internal Kink Mode on the Toroidal Rotation in the KSTAR Tokamak”, Physics Review Letters, 109, 195003 (2012)

[55] Y. Camenen, C. Angioni, A. Bortolon, B. P. Duval, E. Fable, W. A. Hornsby, R. M. McDermott, D. H. Na, Y.-S. Na, A. G. Peeters and J. E. Rice, “Experimental observations and modelling of intrinsic rotation reversals in tokamaks”, Plasma Physics and Controlled Fusion, 59, 034001 (2017)

[56] L.L. Lao, H. St. John, R.D. Stambaugh, A.G. Kellman and W. Pfeiffer, “Reconstruction of current profile parameters and plasma shapes in tokamaks”, Nuclear Fusion, 25, 1611 (1985)

[57] P. C. de Vries, K. M. Rantamaki, C. Giroud, E. Asp, G. Corrigan,

A. Eriksson, M. de Greef, I. Jenkins, H. C. M. Knoops, P. Mantica, H. Nordman, P. Strand, T. Tala, J. Weiland, K.-D. Zastrow and JET EFDA Contributors, "Plasma rotation and momentum transport studies at JET", Plasma Physics and Controlled Fusion, 48, 1693 (2006)

[58] T. Tala, K.-D. Zastrow, J. Ferreira, P. Mantica, V. Naulin, A. G. Peeters, G. Tardini, M. Brix, G. Corrigan, C. Giroud, and D. Strintzi, "Evidence of Inward Toroidal Momentum Convection in the JET Tokamak", Physical Review Letters, 102, 075001 (2009)

[59] P. Mantica, T. Tala, J. S. Ferreira, A. G. Peeters, A. Salmi, D. Strintzi, J. Weiland, M. Brix, C. Giroud, G. Corrigan, V. Naulin, G. Tardini, K.-D. Zastrow, and JET-EFDA Contributors, "Perturbative studies of toroidal momentum transport using neutral beam injection modulation in the Joint European Torus: Experimental results, analysis methodology, and first principles modeling", Physics of Plasmas, 17, 092505 (201)

[60] T. Tala, A. Salmi, C. Angioni, F. J. Casson, G. Corrigan, J. Ferreira, C. Giroud, P. Mantica, V. Naulin, A. G. Peeters, W. M. Solomon, D. Strintzi, M. Tsalas, T. W. Versloot, P. C. de Vries, K.-D. Zastrow and JET-EFDA contributors, "Parametric dependences of momentum pinch and Prandtl number in JET",

Nuclear Fusion, 51, 123002 (2011)

[61] W. M. Solomon, K. H. Burrell, J. S. deGrassie, J. A. Boedo, A. M. Garofalo, R. A. Moyer, S. H. Muller, C. C. Petty and H. Reimerdes, "Characterization of intrinsic rotation drive on DIII-D", Nuclear Fusion, 51, 073010 (2011)

[62] H. Weisen, Y. Camenen, A. Salmi, T. W. Versloot, P. C. de Vries, M. Maslov, T. Tala, M. Beurskens, C. Giroud and JET-EFDA contributors, "Identification of the ubiquitous Coriolis momentum pinch in JET tokamak plasmas", Nuclear Fusion, 52, 042001 (2012)

[63] G. V. Pereverzev, Report IPP 5/42, Garching, Max-Planck-Institut für Plasmaphysik (1991)]

[64] A. Pankin, D. McDune, R. Andre, G. Bateman, A. Kritz, " The tokamak Monte Carlo fast ion module NUBEAM in the National Transport Code Collaboration library", Computer Physics Communications, 159, 157 (2004)

[65] Y. B. Kim, P. H. Diamond, and R. J. Groebner, "Neoclassical poloidal rotation and toroidal rotation in tokamaks", Physics of Fluids B, 3, 2050 (1991)

[66] H. A. Claassen, H. Gerhauser, A. Rogister, C. Yarim, "Neoclassical theory of rotation and electric field in high collisionality plasmas with steep gradients", Physics of Plasmas,

7, 3699 (2000)

[67] C. L. Rettig, T. L. Rhodes, J. N. Leboeuf, W. A. Peebles, E. J. Doyle, G. M. Staebler, K. H. Burrell, R. A. Moyer, "Search for the ion temperature gradient mode in a tokamak plasma and comparison with theoretical predictions", Physics of Plasmas, 8, 2232 (2001)

[68] G.D. Conway, C. Angioni, R. Dux, F. Ryter, A.G. Peeters, J. Schirmer, C. Troester, CFN Reflectometry Group and the ASDEX Upgrade team, "Observations on core turbulence transitions in ASDEX Upgrade using Doppler reflectometry", Nuclear Fusion, 46, S799 (2006)

[69] W. Lee, J. Leem, J. A. Lee, Y. B. Nam, M. Kim, G. S. Yun, H. K. Park, Y. G. Kim, H. Park, K. W. Kim, C. W. Domier, Luhmann N. C. Jr, K.D. Lee, Y. U. Nam, W. H. Ko, J. H. Jeong, Y. S. Bae and the KSTAR Team, "Microwave imaging reflectometry for density fluctuation measurement on KSTAR", Nuclear Fusion, 54, 023012 (2014)

[70] H. Arnichand, R. Sabot, S. Hacquin, A. Krämer-Flecken, X. Garbet, J. Citrin, C. Bourdelle, G. Hornung, J. Bernardo, C. Bottereau, F. Clairet, G. Falchetto and J. C. Giacalone, "Quasi-coherent modes and electron-driven turbulence", Nuclear Fusion, 54, 123017 (2014)

[71] H. Arnichand, R. Sabot, S. Hacquin, A. Krämer-Flecken, C. Bourdelle, J. Citrin, X. Garbet, J. C. Giacalone, R. Guirlet, J. C. Hillesheim, L. Meneses, "Discriminating the trapped electron modes contribution in density fluctuation spectra", Nuclear Fusion, 55, 093021 (2015)

[72] H. Arnichand, J. Citrin, S. Hacquin, R. Sabot, A. Krämer-Flecken, X. Garbet, C. Bourdelle, C. Bottereau, F. Clairet, J. C. Giacalone, Z. O. Guimarães-Filho, R. Guirlet, G. Hornung, A. Lebschy, P. Lotte, P. Maget, A. Medvedeva, D. Molina, V. Nikolaeva, D. Prisiazhniuk, the Tore Supra and the ASDEX Upgrade teams, "Identification of trapped electron modes in frequency fluctuation spectra", Plasma Physics and Controlled Fusion, 58, 014037 (2016)

[73] J. Citrin, H. Arnichand, J. Bernardo, C. Bourdelle, X. Garbet, F. Jenko, S. Hacquin, M. J. Pueschel and R. Sabot, "Comparison between measured and predicted turbulence frequency spectra in ITG and TEM regimes", Plasma Physics and Controlled Fusion, 59, 064010 (2017)

[74] A. G. Peeters, Y. Camenen, F. J. Casson, W. A. Hornsby, A. P. Snodin, D. Strintzi, G. Szepesi, "The nonlinear gyro-kinetic flux tube code GKW", Computer Physics Communications, 180, 2650 (2009)

[75] E. A. Belli and J. Candy, “Kinetic calculation of neoclassical transport including self-consistent electron and impurity dynamics”, Plasma Physics and Controlled Fusion, 50, 095010 (2008)

[76] W. A. Hornsby, C. Angioni, E. Fable, P. Manas, R. McDermott, A. G. Peeters, M. Barnes, F. Parra and The ASDEX Upgrade Team, “On the effect of neoclassical flows on intrinsic momentum in ASDEX Upgrade Ohmic L-mode plasmas”, Nuclear Fusion, 57, 046008 (2017)

[77] G. S. Yun, W. Lee, M. J. Choi, J. B. Kim, H. K. Park, C. W. Domier, B. Tobias, T. Liang, X. Kong, N. C. Luhmann Jr, and A. J. H. Donne, “Development of KSTAR ECE imaging system for measurement of temperature fluctuations and edge density fluctuations”, Review of Scientific Instruments, 81, 10D930 (2010)

[78] T. S. Hahm, P. H. Diamond, O. D. Gurcan, G. Rewoldt, “Nonlinear gyrokinetic theory of toroidal momentum pinch”, Physics of Plasmas, 14, 072302 (2007)

[79] A. G. Peeters, C. Angioni, and D. Strintzi, “Toroidal Momentum Pinch Velocity due to the Coriolis Drift Effect on Small Scale Instabilities in a Toroidal Plasma”, Physical Review Letters, 98, 265003 (2007)

Abstract in Korean

플라즈마 유동은 토카막 플라즈마 성능 및 안정성에 영향을 주는 것으로 알려져 있다. 한편, ITER와 같은 대형 장치에서는 현존하는 토카막 장치와 달리 중성입자입사 시스템에 의한 플라즈마 유동이 매우 작을 것으로 예측되기 때문에, 고유 유동 연구는 토카막 플라즈마의 중요한 이슈 중 하나이다. 오믹 플라즈마는 토카막 고유 유동의 물리적 기작을 연구하기에 가장 적합한 플라즈마로써, 다양한 장치에서 실험이 수행되고 있었다. 국내 토카막 장치인 KSTAR의 경우도 고유 유동에 대한 실험적 연구가 오믹 플라즈마에서 수행되고 있었으며, 본 연구가 수행되기 이전까지는 XICS 진단을 기반으로 한 플라즈마 중심에서의 유동 연구만 수행되고 있었다 ($V_\phi(0)$ 을 기반으로 한 고유 유동 특성 분석). 본 연구에서는 전체 고유 유동 분포를 진단할 수 있게 실험을 설계하고, 이를 기반으로 하여 KSTAR 오믹 플라즈마의 고유 유동에 대한 실험적 특성을 분석하였다. 이를 바탕으로 다양한 고유 유동 기작 이론과의 비교 분석을 수행하였고, 통합 모델링을 통한 전체 고유 유동 분포의 계산 및 비교의 과정을 통해 KSTAR 오믹 플라즈마의 고유 유동 기작에 대해 논의하였다.

KSTAR에서 전체 고유 유동 분포 진단을 위해서는 필연적으로 중성입자입사가 요구된다. 이 때, 중성입자입사는 플라즈마 성질에 섭동을 줄 뿐만 아니라, 외부 토크로 인한 플라즈마 유동의 변형을 초래하므로, 이런 외부 섭동을 최소화하고 가능한 실제 오믹 플라즈마의

고유 유동을 측정하는 것이 가장 우선시 된다. 이를 위해 KSTAR 오믹 플라즈마에서 고유 유동을 측정하기 위한 중성입자입사 장치의 최적 운전 조건을 실험적으로 도출하였다. 플라즈마 상태 및 목적에 따라 최적 운전 조건은 달라질 수 있지만, 400−600 kA의 플라즈마 전류의 KSTAR 오믹 플라즈마에서 일반적으로는 20 ms x 2 Hz 이하의 입사는 최소한으로 만족되어야 하는 것을 확인할 수 있었다.

다양한 운전 및 플라즈마 조건에서 측정한 고유 유동 분포를 살펴본 결과, 기존의 $V_\phi(0)$ 기반의 분석이 한계가 있음을 실제적으로 확인하였다. $V_\phi(0)$ 기반의 분석이 고유 유동 특성을 충분히 포함하려면, 크게 두 가지 조건이 요구된다. 하나는 플라즈마 경계 부근의 고유 유동이 무시할만해야 하며, 또 다른 하나는 고유 유동의 분포가 단순한 곡선 형태를 띄어야 한다는 것이다. KSTAR 오믹 플라즈마의 다양한 운전 및 플라즈마 조건에서 플라즈마 경계 부근의 고유 유동이 달라질 수 있으며, 심지어 동일한 운전 조건이더라도 언제 실험이 수행되었느냐에 따라 달리지는 것이 확인되었다. 이는 플라즈마 경계 부근의 고유 유동이 운전 조건뿐만 아니라 불순물 정도 등에 민감하다는 것을 의미하며, KSTAR 오믹 플라즈마에서의 경계 부근의 고유 유동 변화는 최대 20 km/s까지 이르는 것이 확인되었다. 이는 $V_\phi(0)$의 변화 정도와 비교해 볼 때 결코 무시할 수 없는 수준이다. 또 다른 하나는 고유 유동의 분포가 단순한 곡선 형태를 띠지 않고 기울기가 내부에서 급격하게 변하는 영역이 존재할 수 있다는 것이다. 이는 곧 실제 고유 유동 특성을 파악하기 위해서는 전체 고유 유동의 분포를 고려하여야

한다는 것을 방증한다. 이런 특성을 고려하여, 2016년 KSTAR 캠페인까지 확보된 약 300여개의 데이터베이스를 활용하여 KSTAR 오믹 플라즈마의 고유 유동 특성을 분석함에 있어 고유 유동 분포에 기반한 분석을 수행하였다.

먼저, 전형적인 고유 유동 분포에 대해 살펴보았으며, KSTAR 오믹 플라즈마의 고유 유동은 크게 네 개의 영역으로 구분되는 구조를 가지는 것을 확인하였다. 플라즈마 중심부와 가까운 가장 안쪽 영역은 다소 평평하거나 약간 볼록한 형상을 가지는 구조가 보이며, 이는 주로 톱날 불안정성의 영역과 일치하는 것이 확인된다. 다음은 기울기 영역으로 가파른 기울기를 갖는 분포가 쉽게 관측되며, 일반적으로 KSTAR 오믹 플라즈마에서는 양의 기울기, 즉 결과적으로 오목한 형상의 고유 유동 분포를 나타내게 하는 주요 요소로 작용하는 영역이 관측된다. 이 영역은 플라즈마 밀도 증가 시 기울기가 크게 변화하며, 결과적으로 $V_\phi(0)$ 의 변화를 초래하는 것과 가장 큰 연관이 있다. 그 다음은 앵커 포인트 영역이다. 여기서는 고유 유동의 분포가 다시 평평해지며, 안쪽의 기울기 영역의 경계영역으로 작용하는 것처럼 보인다. 이 영역은 실제 플라즈마 경계에서 멀리 떨어진 곳으로, 실제 플라즈마 경계 영역과 구분된다. 마지막은 앵커 포인트 영역과 실제 플라즈마 경계 사이의 영역으로, 이 구간은 플라즈마 운전 조건에 따라 형상 및 고유 유동 값이 다양하게 존재한다.

여러 가지 운전 조건에 대해 분포를 분석해 본 결과, KSTAR 오믹 플라즈마에서 고유 유동 분포는 밀도가 증가함에 따라 평평한 형상에서

오목한 형상으로 바뀌는 것을 확인할 수 있으며, 이런 고유 유동의 변화 영역은 q_{95} 와 밀접하게 관련이 있는 것을 확인할 수 있었다. 이 때, 고유 유동 분포 형상 변화는 플라즈마 밀도 증가에 따라 정규화된 고유 유동의 기울기 (u')가 크게 변화함에 따라 나타나는데, 그 변화는 기울기 영역으로만 제한되며 앵커 포인트 영역에서는 거의 변화가 관측되지 않는다. 이 때, 기울기 영역은 q 값이 낮고 자기 전단이 작은 영역에 해당하고, 앵커 포인트 영역은 q 값이 기울기 영역보다 크며, 자기 전단이 큰 영역에 해당하는 것으로 확인된다.

기울기 영역에서 u' 은 근사적으로 잔류 응력(고유 유동 유발 기작)과 운동량 확산 계수의 비로써 나타낼 수 있다. 이 때, 잔류 응력과 운동량 확산 계수는 ITG/TEM과 같은 난류 특성과 관련이 있을 것으로 예상되므로, 난류 특성에 영향을 미치는 주요 플라즈마 인자인 $R/L_{T_i}, R/L_{T_e}, T_e/T_i, \nu_{eff}$ 등과의 상관 관계를 분석하였다. 그 결과 가장 높은 상관성을 보이는 인자는 ν_{eff} 와 T_e/T_i 인 것으로 도출되었다. 흥미롭게도 기울기 영역에서의 u' 변화는 시변 수송 전산모사 분석을 통해 운동량 확산 계수의 큰 변화와 관련이 있을 것으로 확인되었다. 이는 EC 인가를 통해 훨씬 낮은 ν_{eff} 에 대한 u' 을 분석하였을 때에도 양의 값을 갖지 않는 실험적 관측 및 선형/비선형 자이로키네틱 전산모사 결과와 합의를 이룬다.

KSTAR 오믹 플라즈마 데이터베이스를 활용하여 이론적 모델이 앞서 관측한 고유 유동 특성을 잘 예측할 수 있는지 비교 분석해 보았다. 신고전 수송 모델 및 다양한 난류 수송 모델을 비교 분석해 본 결과

“유한 벌룬 틸팅” 모델의 경우가 실험에서 관측한 고유 유동 특성과 가장 잘 일치하는 것으로 확인되었다. 비록 임의의 (그러나 가능한 수준의 범위 내의) 틸팅 각도가 사용되었지만, 실험에서 관측한 수준의 u' 의 값을 나타낼 수 있었고, 특히 고정된 틸팅 각도 하에서도 기울기 영역의 u' 변화 특성과 앵커 포인트 영역의 서로 상반된 특성도 잘 예측하는 것으로 평가되었다. 영역에 따른 모델 예측의 차이는 자기 전단과 큰 관련성이 확인되었는데, 자기 전단이 1보다 작고 q가 작을수록 전산모사 결과가 기울기 영역의 u' 변화와 경향성을 보이고, 자기 전단이 1보다 크고 q가 클수록 u'의 예측값이 작아지며 경향성이 달라지는 것을 확인할 수 있었다. 이는 기울기 영역과 앵커 포인트 영역이 q 값과 자기 전단 값과 관련이 있는 실험적 관측 결과와 일치한다.

마지막으로, “유한 벌룬 틸팅” 모델을 적용하여 KSTAR 오믹 플라즈마의 전체 고유 유동 분포를 계산하기 위해, GKW 코드와 수송 코드인 ASTRA를 결합하여 전산모사를 수행하였다. 실제 실험에서 진단된 고유 유동보다는 작게 예측하는 결과를 보였지만, 밀도 증가에 따른 u' 의 변화 경향성 및 앵커 포인트와 기울기 영역을 갖는 분포 경향성을 잘 예측하는 것으로 확인되었다. 이는 “유한 벌룬 틸팅” 모델이 KSTAR 오믹 플라즈마의 고유 유동 기작으로써의 높은 가능성을 가지는 것을 보여주며, 특정 고유 유동 기작을 포함한 통합 수송 모델링 및 플라즈마 유동 예측 방법론은 향후 다양한 응용 가능성을 포함하고 있다.